

Chair of Metal Forming  
Department Product Engineering  
University of Leoben, Austria



**DISSERTATION**

# **INVESTIGATION OF BALL SPINNING**

A thesis submitted to the University of Leoben  
in partial fulfilment of the requirements of the degree of  
Doktor der Montanistischen Wissenschaften

Mario Josef Kuss  
Leoben, April 2016



„Der Friede beginnt im eigenen Haus“

*Karl Jaspers*



## **Affidavit**

I declare in lieu of oath, that I wrote this thesis and performed the associated research myself, using only literature cited in this volume.

Leoben, April 2016

Mario Josef Kuss



## Acknowledgements

First of all, I would like to thank my supervisor, Prof. Bruno Buchmayr for his support and his confidence in me and my work.

Further, I would like to thank all the people on the Chair of Metal Forming and the community of the colloquium on metal forming for letting me be a part of its community. In countless entertaining conversations and discussions, I was able to get new insights and found new friends.

I wish to express my gratitude to my wife Manuela Kuss for her love and patience during periods of hard work. She is my rock and my fortress.

I also owe special thanks to my family Renate, Josef und Manuela Kuss for their confidence and support during all my life.

My thanks are especially applied to Robert Kaiser, Otto Harrer and Thomas Hatzenbichler. Their technical advice in numerical simulation and scientific understanding of metal forming was an invaluable help during this work. Furthermore, I want to thank Ralph Ambrosch, Christian Stöckl and Martin Dirscher for their technical assistance.

What is a life without friends? Colleagues became friends during this time. Special thanks to Andreas Weber for the hot chocolate trips and Gernot Eggbauer, Roland Kasberger and Christian Leodolter for the discussions during lunch. I want to thank Stefan Wallner and Barbara Böck for introducing me into the Chair of Metal Forming and for our annual family jaunt.

Finally I want to thank my friends Caroline Leodolter, Florian Glitzner, Johannes Kloepfer and Peter Brandl for the distraction in times of turbulence and demotivation.

## **Abstract**

To manufacture lightweight tubes, fabricators increasingly use incremental forming processes like ball spinning. The use of such processes requires a profound knowledge of material properties and process understanding.

This dissertation provides an overview about ball spinning and its modifications. Also a method to calculate the forming forces analytically is presented and compared to experiments and finite element simulations. A closer look to the process points out the dependence of process parameters to the damage behaviour. A 2D finite element model is presented to predict the damage during ball spinning. The results are showing the trend to modify the process parameters for a damage minimised process design.

The internal stress state of products after the forming process has also become an increasing focus. This is especially important for the prediction of lifetime under fatigue conditions of the product. The effects on kinematic and isotropic hardening of high strains has a significant influence on forming processes with reversing strain hardening like ball spinning. This investigation gives a detailed view into the deformation mechanism of a ball spinning expansion process with the finite element method. A closer look taken on to the differences between kinematic and isotropic hardening to the internal stress state after the forming process. This investigation provides a method to calibrate the combination of the strain hardening parameters on the final geometry, demonstrated by an experiment. Therefore, the final internal stress state and the lifetime prediction can be computed more precisely.

## **Kurzfassung**

Für die Produktion von gewichtsreduzierten Bauteilen kommen verstärkt inkrementelle Umformprozesse wie beispielsweise Kugeldrücken zur Anwendung. Der Einsatz solcher Technologien erfordert ein hohes Maß an Material- und Prozessverständnis.

Diese Doktorarbeit gibt einen Überblick über das Kugeldrücken sowie dessen Modifikationen. Es wird eine Berechnungsmöglichkeit gezeigt, welche es ermöglicht die Umformkräfte beim Kugeldrücken vorherzusagen. Diese Methode wurde mit Experimenten und numerischen Simulation verglichen und überprüft. Eine genauere Betrachtung des Prozesses zeigt die Abhängigkeit von Prozessparametern auf das Schädigungsverhalten während der Umformung. Es wird ein 2D Finite Element Model vorgestellt um das Schädigungsverhalten von Kugeldrücken vorherzusagen. Die Ergebnisse zeigen den Trend von Parameterveränderungen für eine schädigungsminimierte Prozessauslegung.

Der Eigenspannungszustand nach der Umformung hat einen entscheidenden Einfluss auf die Vorhersage von Lebens- und Betriebsdauer eines Bauteiles. Die Modelle der kinematischen und isotropen Verfestigung divergieren vor allem bei Prozessen mit wechselnder Verformungsrichtung wie beispielsweise dem Kugeldrücken. Mithilfe der Finiten Elemente Simulation können die Unterschiede zwischen den Verfestigungsmodellen beim aufweitenden Kugeldrücken gezeigt werden. Es wird eine Methode präsentiert um diese Modelle zu kombinieren und mit Experimenten zu kalibrieren. Dies ermöglicht eine exaktere Vorhersage des Eigenspannungszustandes sowie die davon abhängige Lebensdauer eines Bauteiles.

## Contents

<b>Affidavit</b> .....	<b>5</b>
<b>Acknowledgements</b> .....	<b>7</b>
<b>Abstract</b> .....	<b>8</b>
<b>Kurzfassung</b> .....	<b>I</b>
<b>Contents</b> .....	<b>I</b>
<b>List of Symbols</b> .....	<b>3</b>
<b>1. Introduction</b> .....	<b>6</b>
<b>2. State of the Art</b> .....	<b>7</b>
2.1 Description of Metal Spinning .....	7
2.2 Description of Ball Spinning .....	12
<b>3. The Market Need</b> .....	<b>18</b>
<b>4. Systematic Process Consideration</b> .....	<b>19</b>
<b>5. Finite Element Simulation of Flow Forming and Ball Spinning</b> .....	<b>29</b>
<b>6. Radial Forging versus Flow Forming</b> .....	<b>34</b>
6.1 Model Set Up.....	34
6.2 Results of the Comparison of Radial Forging and Flow Forming .....	36
<b>7. Forming Forces of Ball Spinning</b> .....	<b>38</b>
7.1 Analytical Calculations.....	38
7.2 Experimental Investigation of the Forming Forces .....	45
7.3 FEM Simulation for the Forming Forces .....	47
7.4 Comparison of the Axial Forming Force.....	48
7.5 Metallography after the Ball Spinning Expansion Process .....	50
7.1 Stress State of a Ball Spinning Expansion Process .....	53
7.2 Sensitivity Study on the Effects of Process Parameters on the Forming Forces.....	55

<b>8. Damage Minimised Ball Spinning Process Design .....</b>	<b>57</b>
8.1 2D FEM Simulation of Damage Behavior .....	57
8.2 Statistical Design of Experiments.....	61
8.3 Experimental Details for a Ball Spinning Reduction Process .....	71
<b>9. Internal Stress State after Ball Spinning.....</b>	<b>74</b>
9.1 Hardening Models .....	74
9.1 Calibrating the Combination of the Strain Hardening Parameters .....	78
9.2 Result of the Hardening Models during Ball Spinning .....	82
<b>10. Discussion .....</b>	<b>89</b>
<b>11. Conclusion and Outlook .....</b>	<b>93</b>
<b>Bibliography.....</b>	<b>95</b>
<b>List of Figures .....</b>	<b>100</b>
<b>List of Tables.....</b>	<b>103</b>
<b>Author's Publications.....</b>	<b>105</b>

## List of Symbols

symbol	unit	comment
$r$	mm	ball radius
$D_{i1}$	mm	workpiece inner diameter before forming
$D_{i2}$	mm	workpiece inner diameter after forming
$x_r$	mm	radial reaming before forming
$D_1$	mm	initial workpiece diameter
$D_2$	mm	final workpiece diameter
$h$	mm	height of a ball segment
$a$	mm	radius of a ball segment
$A$	mm <sup>2</sup>	contact surface
$A_k$	mm <sup>2</sup>	surface of a ball segment
$A_{dr}$	mm <sup>2</sup>	contact surface of a ball
$v$	mm/rev	axial feed rate
$z_d$	mm/rev	axial feed rate of one ball
$F_{ges}$	N	resulting forming force
$M_A$	Nm	drive torque
$M_F$	Nm	frictional moment
$F_F$	N	frictional force
$F_{GT}$	N	tangential component of $F_{ges}$
$F_{GR}$	N	radial component of $F_{ges}$
$F_{GRL}$	N	leading ring force
$F_r$	N	radial force
$F_t$	N	tangential force
$F_z$	N	axial force

---

<b>symbol</b>	<b>unit</b>	<b>comment</b>
$R_p$	$N/mm^2$	flow stress
$k_f$	$N/mm^2$	flow stress
$\sigma_m$	$N/mm^2$	medial stress
$\sigma_v$	$N/mm^2$	equivalent stress
$\sigma$	$N/mm^2$	stress
$E$	$N/mm^4$	Young's modulus
$t_{ges}$	sec	process time
$U$	rev/min	rotational speed
$R_a$	$\mu m$	arithmetical mean roughness
$R_q$	$\mu m$	root mean squared
$R_z$	$\mu m$	maximum height
$PE$	-	plastic strain
$n$	-	number of balls
$n_c$	-	number of contacts
$N_{Ges}$	-	number of experiments
$N_w$	-	number of cube experiments
$N_{St}$	-	number of star experiments
$N_0$	-	number of centre experiment
$\lambda$	-	range of the experimental star
$\eta$	-	efficiency of plastic deformation
$\mu$	-	friction coefficient
$PEEQ$	-	effective plastic strain

---

---

---

## 1. Introduction

Engineers are forced to come up with smart, flexible and cheap manufacturing solutions to master the challenges of the global market. Incremental forming processes like radial forming or flow forming get into focus for the production of lightweight products. For some products, special forming processes are needed to maintain complex geometry conditions. One example for such a product is the flexspline of a harmonic-drive gearing described by Groche and Fritsche (2006). This flow forming process with a multiple-roll-principle is called “ball spinning”.

In this context, the numerical simulation of ball spinning plays a significant role as it allows insights into this complex forming process. Commonly, the numerical simulation of incremental forming processes aims to determine the material flow and stress- and temperature distribution inside the workpiece.

This dissertation gives a general overview of the ball spinning process, presents missing analytical calculations and provides a closer look to the deformation mechanism using the finite element method. Further the limitations of the surface behaviour are examined and the influence on hardening models to the internal stress state is emphasized.

## 2. State of the Art

Metal spinning is an old incremental metal forming technique. Over the years, other forming processes such as deep drawing and ironing displaced this process. The market demand of material efficiency, flexibility in geometry, low to middle lot sizes and near net shape manufacturing leads in combination with numerical control to a new uptrend of metal spinning (Wong et.al., 2003). These kind of forming processes are characterised on the one hand by low tool costs and flexible material, temperature and geometry applications. On the other hand, a high knowledge of material behaviour, influencing parameters and process understanding is required to control the process efficiently.

### 2.1 Description of Metal Spinning

Generally, the workpiece is turned by friction grip by a tailstock and a mandrel. The tool is a roller with a simple geometry, which is controlled axially and radially. The rotation of the roller is induced by friction at the contact area to the workpiece and the deformation zone is below the contact area. These processes are generally used to produce axisymmetric profiles as seen in Fig. 1.

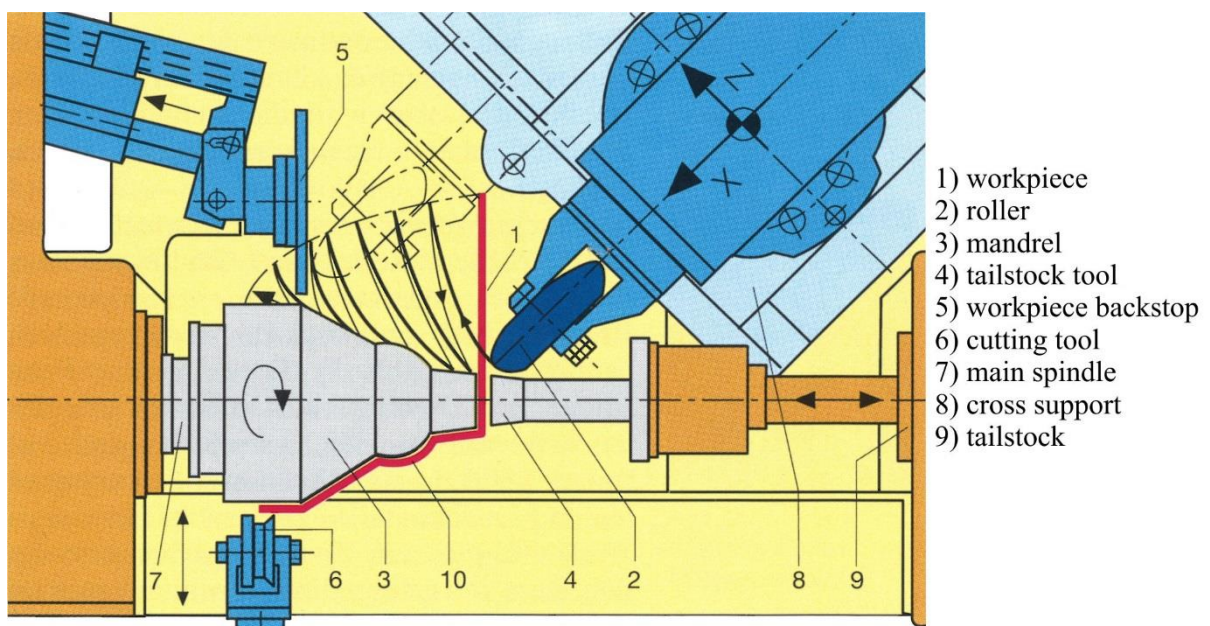


Fig. 1: Set up for a metal spinning process (Runge, 1993).

There are three different types of metal spinning:

- Spinning
- Shear Forming
- Flow Forming

DIN (German Institute for Standardisation) Standard 8582 classifies metal spinning by the different stress states during deformation. The spinning process deforms blanks by a combination of compression and tension stresses. Shear forming and flow forming are characterized by compression stresses as shown in Fig. 2 (Runge, 1993).

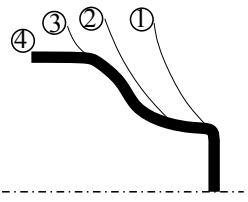
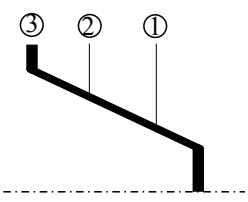
standard	compression and tension stress DIN 8582/ DIN 8584	compression stress DIN 8582/ DIN 8583	
process	<b>Spinning</b>	<b>Shear Forming</b>	<b>Flow Forming</b>
preform			
final contour			

Fig. 2: Classification of metal spinning processes.

**Spinning** is known as a process for an axisymmetric deformation of sheet metal blanks on a mandrel with one roller. Thereby the thickness is constant over the final contour. The numbers at the final contour of the spinning process marks the geometry of the incremental process steps over the production time.

**Shear spinning** is a process whereby a disc is projected on a mandrel. Thereby the thickness of the final contour depends on the mandrel geometry. The numbers mark the geometry of the incremental process steps during deformation. Fig. 3 shows a spinning process with a round blank and shear spinning and spinning products.



Fig. 3: Spinning and shear spinning products (Runge, 1993).

During **flow forming** tubes or cups are deformed axially and radially as seen in Fig. 2 and it is used to produce cylindrical components. Most modern flow forming machines employ one to three rollers and their design is more complex compared to that of spinning or shear forming rollers (Wong et.al., 2003). Generally, there are two different methods of flow forming, as depicted in Fig. 4.

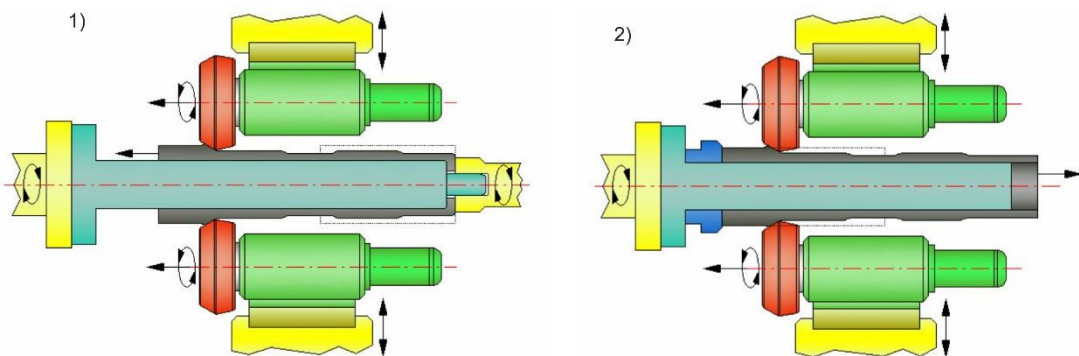


Fig. 4: Principle of flow forming 1) forward flow forming, 2) backward flow forming (Gün and Güveli, 2007)

In the forward flow forming method (1), the material flows in the same direction with the axial movement of the rollers. The workpiece is fixed on the mandrel with a tailstock and, hence, has the geometry of a cup to absorb the axial deformation forces. The maximum axial stresses during deformation limit this method. The second method is the backward flow forming process (2). The preform is a tube and the rollers pressures the workpiece against a toothed ring. The axially elongation of the tube is in the opposite direction of the rollers. During this method only

axial compression stresses occurs (Gün and Güveli, 2007). Fig. 5 shows a flow forming process of a tube and flow forming products.

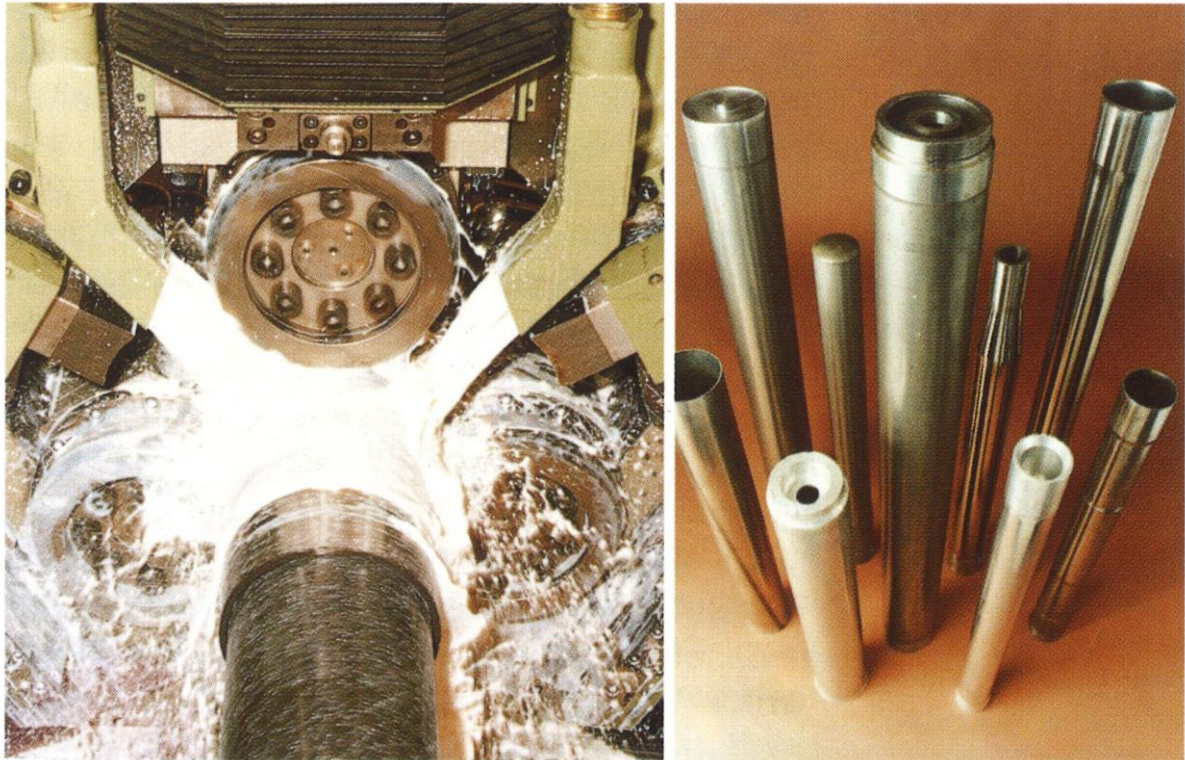


Fig. 5: Flow forming process (left) and products of such a process (right) (Runge, 1993).

There are many different process modifications of flow forming as Sivanandini et al. (2012) explain. The combination of expansion process and flow forming is explained in Fig. 6. Thereby the mandrel (4) expands the tube (1) and simultaneously the roller (3) reduces the thickness. The preform (2) is fixed in the lathe chuck (6). The diameter tolerance is about IT7-IT8 (Herold and Abdel-Kader, 1998).

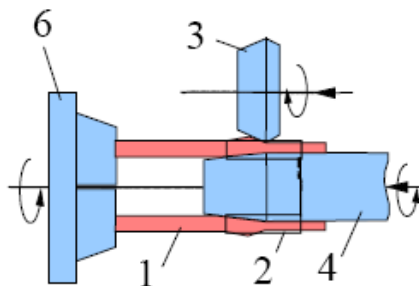


Fig. 6: Combination of expansion process and flow forming (Herold and Abdel-Kader, 1998).

The combination of extrusion and flow forming is shown in Fig. 7. A rod (1) is fixed and turned by a lath chuck (6) and a rotating mandrel (4) penetrates the workpiece while a roller (3) reduces the rod over the mandrel to a tube. Due to the rotation different geometries, as well as gears, multi wedges, or polygons are used as mandrels (Herold and Abdel-Kader, 1998).

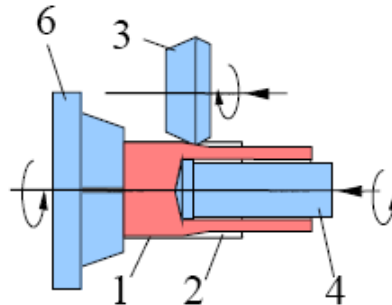


Fig. 7: Combination of extrusion and flow forming (Herold and Abdel-Kader, 1998).

One special innovation of flow forming is friction spinning as Homberger (2009) describes (Fig. 8). This method was developed to save the recrystallization annealing between the deformation steps. During friction spinning the workpiece is turned by a tailstock (a) and is pressed to a friction plate (b). Due to the friction the workpiece is heated locally. When the workpiece has the correct forming temperature, then the material flows radially outwards and is controlled by a roller.

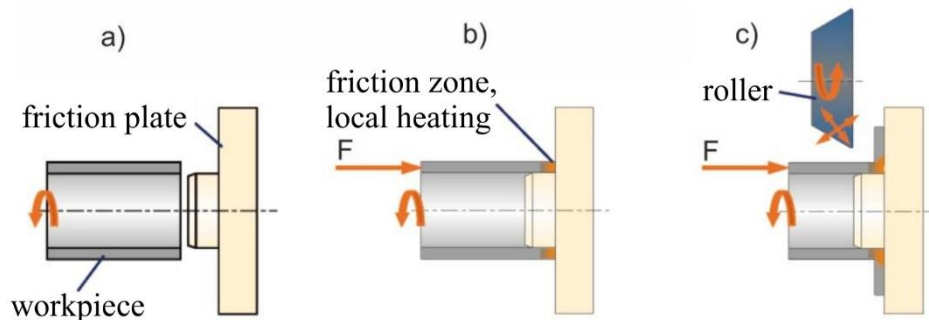


Fig. 8: Principle of friction spinning by Homberger (2009).

## 2.2 Description of Ball Spinning

Conventionally, one, two or three rolls are used for flow forming. During the production of inner ripped tubes with the use of mandrels, the forming force swivels around the mandrel tooth (Fig. 9 a, Pos1 to Pos 2). This is the reason for cracks at the throat and a reduction of the tool life. This lead to the idea of introducing several rolls as Ahmed (2011) described. Thereby the tangential component of the forming force are mutually eliminated and the lifetime of the mandrel is improved (Fig. 9 b).

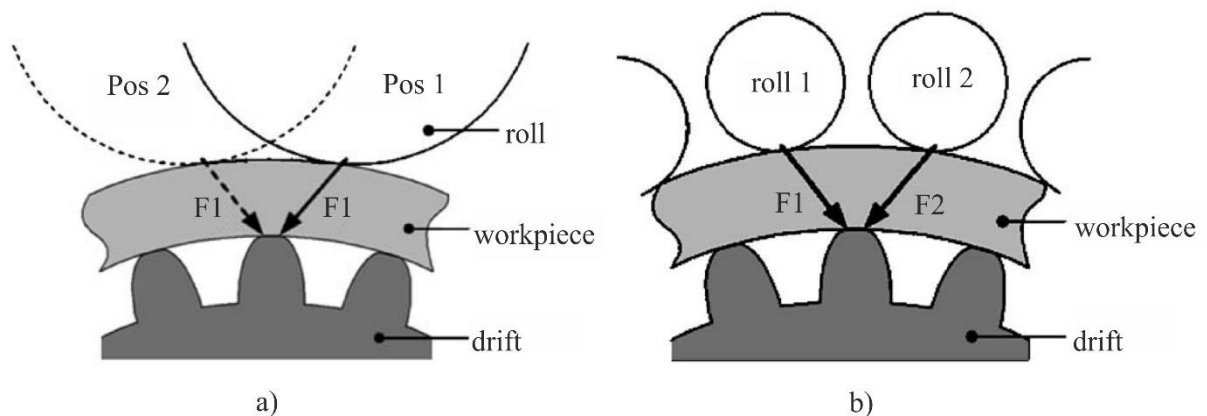


Fig. 9: Process description: (a) three roll principle, (b) multiple roll principle (Groche & Fritsch, 2006).

One process application is the multiple roll principle with spherical tools called ball spinning. Similar to a ball bearing, the balls are controlled by a cage (Fig. 10). As mentioned by Birk (1985), the diameter reduction of the tube is adjusted by the diameter of the balls and the diameter of the outer leading ring.

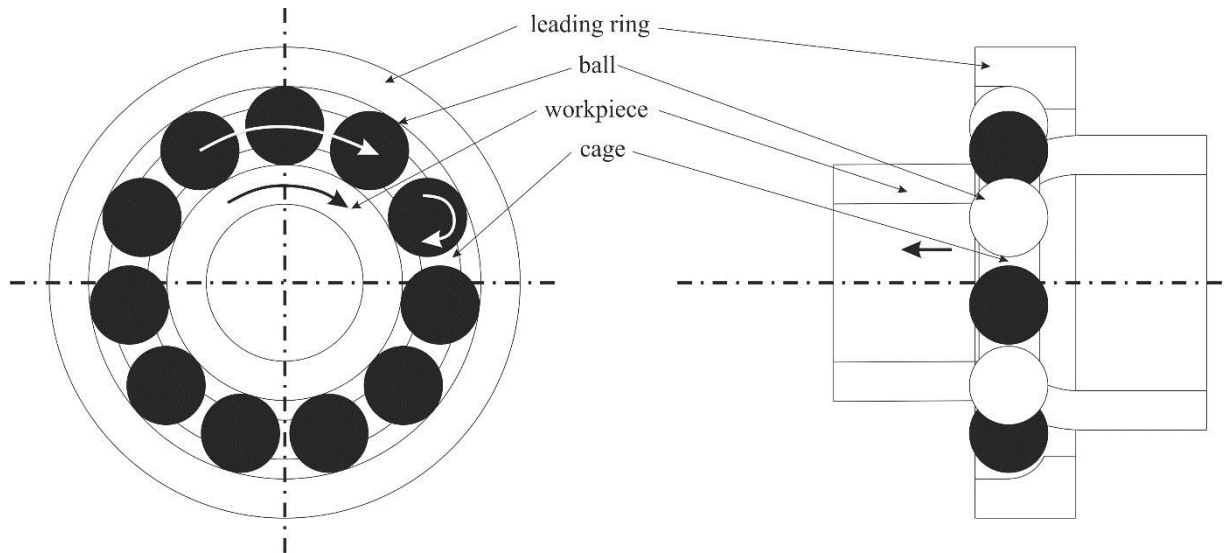


Fig. 10: Set up of a ball spinning reduction process (Kuss & Buchmayr, 2015).

During flow forming, every ball is rolling spirally over the tube, therefore, the number of balls determines the feed rate of the tool. As pointed out by Birk (1985), the biggest advantage of this technology is the increased feed rate due to the large number of forming zones. Hofen & Wenke (1986) and Friedmann (1984) stated, that the ball spinning process is about ten times faster than a conventional flow forming process. Thus, the ball spinning process must be cooled in a more extensive way compared to other incremental forming processes.

Conversely, the main disadvantage of this process is the missing flexibility. Ball spinning requires a new tool for every tube diameter. This problem can be solved by using a conical leading ring, as shown in Fig. 11. An additional screw tube is used to position the balls axially, thereby adjusting the diameter in the range of the conical leading ring.

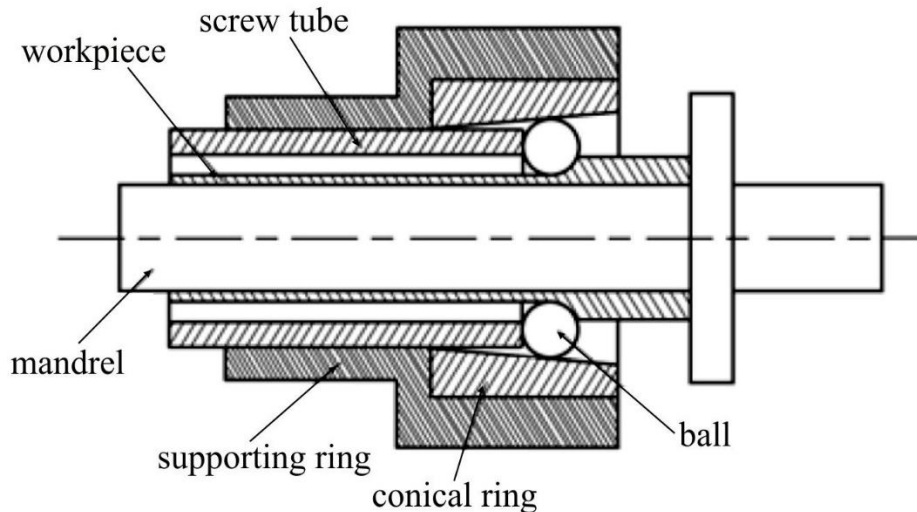


Fig. 11: Ball spinning with variable diameter (Jiang et. al. 2009).

The main difference to flow forming is the self-regulation of the rotation axis of the forming tools due to the geometrical boundary conditions. A dome-shaped leading ring causes a variable rotation axis and a low surface pressure. The rotation axis by a conical leading ring is unchangeable and the surface pressure is higher. The most important forming parameters for the ball spinning process are listed by Heidel & Kühmel (1979) and Birk (1985). The key parameters are the number of balls, the leading ring geometry, the feed rate, the rotational speed and the cooling and lubrication conditions. Nowadays ball spinning is used e.g. for the production of tubes with longitudinal inner ribs as Jiang et. al. (2009) show.

The serial combination of following ball spinning processes, as shown in Fig. 12, is another way to modify the process. Through this combination, a higher diameter reduction can be realized in one operation of the tool. In the first forming zone, higher ball diameters are used to reduce the build-up of the material in front of the ball. The last forming zone calibrates the final diameter and is responsible for the dimensional stability (Heidel & Kühmel, 1979)

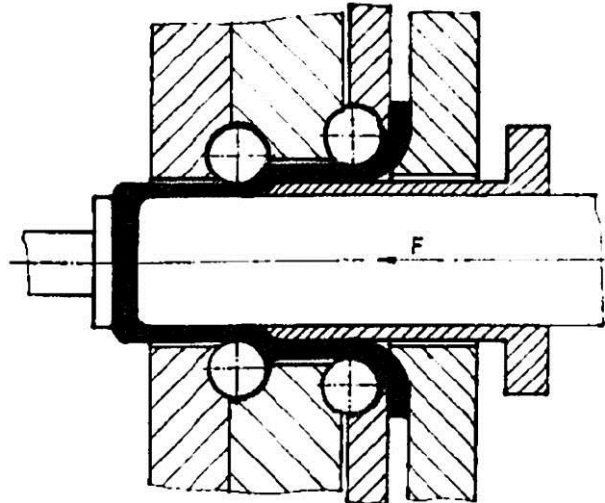


Fig. 12: Step tool for reduction of a round blank with ball spinning (Hofen & Wenke, 1986).

Another variant of the ball spinning reduction process is the ball spinning expansion process as described by Hofen & Wenke (1986). Similarly to Fig. 10, the inner leading ring adjusts the diameter and the tube is expanded by the rotating balls (Fig. 13). This process is applied in the production of harmonic-drive gearings, collar-spinning process for the cookware industry, and is used for surface hardening.

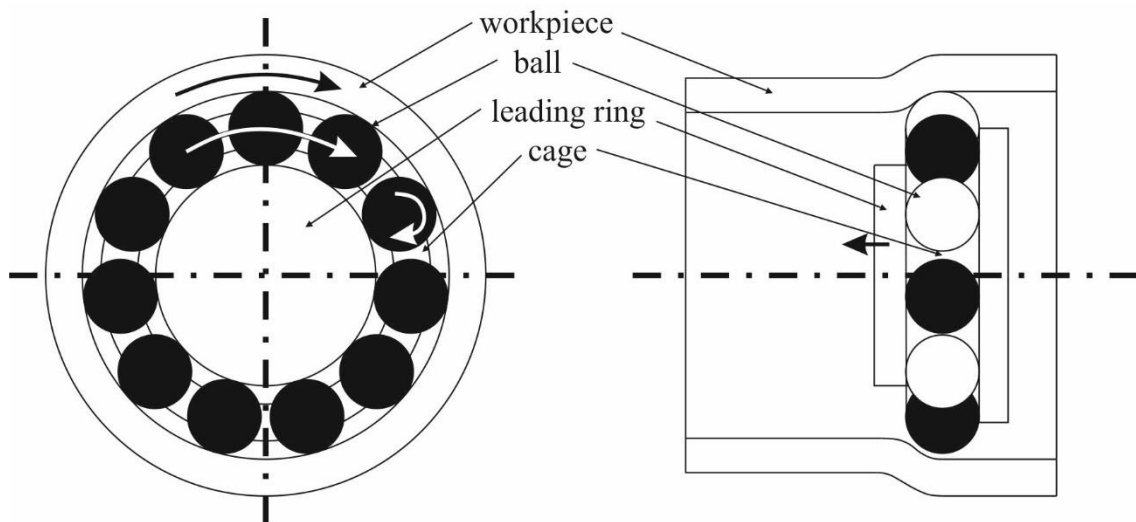


Fig. 13: Set up of a ball spinning expansion process (Kuss & Buchmayr, 2015).

### 2.2.1 Advantages and Disadvantages of Ball Spinning

The biggest advantages of ball spinning are the multiple forming zones of the process combined with a short processing time. This made ball spinning attractive for mass-production. Nowadays, the process excels at deformation mechanism of the hydrostatic stress state and minimization of grain size at the deformed surface. Hence, longitude ripped tubes or products with internal teeth can be produced. Besides the deformation mechanism as primary action, the high quality of the deformed surface is also a great benefit. Nevertheless, the main disadvantage of ball spinning is the missing flexibility to control the final geometry. Additionally, the process potentiates existing material defects like cracks or chatter marks at the surface.

### 2.2.2 Influencing Parameters of the Ball Spinning Process

The most important influencing parameters of ball spinning are listed by Heidel & Kühmel (1979) and Birk (1985). These parameters are the number of balls, as well as the ball diameter, leading ring geometry, and the feed rate.

#### Number of Balls

The maximal number of balls is geometrically limited. Between 70-100% of the maximal number of balls, no significant influence appears. Under 70%, the build-up after the deformation zone of the reduction process intensifies. Due to an expansion process, the roundness declines.

#### Diameter of Balls

The rotation angle of the balls is defined by the diameter of the balls, combined with the reduction value. With a reduction of the diameter, the axial and radial build-up grows. In contrast to that, the form deviation and roundness become declining with higher ball diameters.

#### Feed Rate

All forming force components raise with an increase of the feed rate. In addition, the turning speed has to be increased for a constant quality.

### Leading Ring Geometry

A linear leading ring geometry (b) forces the balls into a fixed angle of the rotation axis. Therefore, a high contact pressure at the leading ring occur. The angle of rotation at a circular leading ring (a) is flexible and depends on the contact point to the workpiece. This set-up reduces the contact pressure, compared to a linear leading ring system. Fig. 14 (c) exhibits a two-part leading ring for a material reduction in both directions.

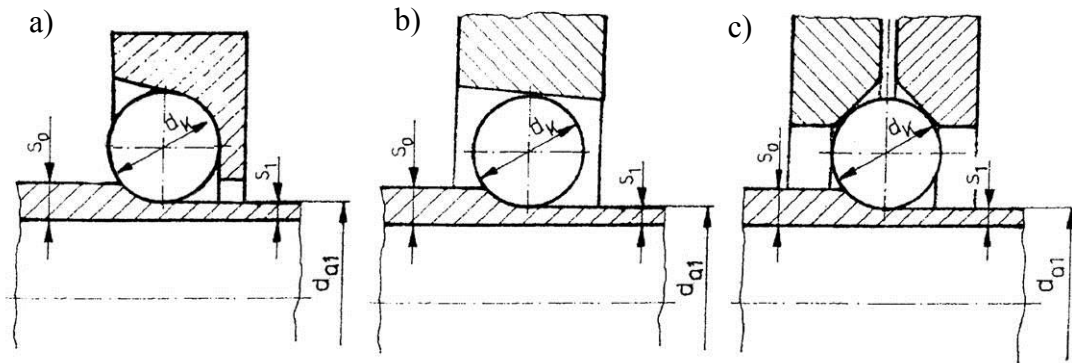


Fig. 14: Leading ring geometries a) circular leading ring, b) linear leading ring, c) two part leading ring (Hofen & Wenke, 1986; Friedmann, 1984).

### 3. The Market Need

The metal forming market demands smart, flexible and cheap manufacturing solutions to master the challenges of low to middle lot sizes with a high product variety. Incremental forming processes like radial forming or flow forming emerge into focus for the production of lightweight products. Some special forming products maintain complex stress conditions, for example ball spinning obtains a triaxial state of compressive stress. Axial symmetric products that require a triaxial compressive stress state are the flexspline of harmonic-drive gearings, as Groche and Fritsche (2006) describe, as well as the inner spiral copper pipe for air conditioners or electronic devices (Wang, 2015). The high radial pressure ensures a controlled material flow to fill deep cavities. Simple tool geometries and a self-regulating rotation axis guarantee an ideal material flow to the direction of least flow resistance. A secondary effect of ball spinning is the excellent surface finish. This characteristic, together with internal compressive stresses, is responsible for a high fatigue limit. With a wide range of process parameters, these effects can be specifically optimised for the product requirements.

Interviewing the management of companies about flow forming or ball spinning technologies has shown that adaption to the processes is done intuitively by their workers. The workers, practically employed with these technologies, are able to vary process parameters flexibly, due to their experience with the process, and achieve good results. This approach is often faster and cheaper as to allocate resources into research and development. Nevertheless, understanding specific parts and alterations to the processes in detail is fundamental to maintain competitive within this industry, which lead to a strong cooperation between universities and the industry.

Despite the fact, that ball spinning with all its features is not flexible in the geometric variety, it obtains several advantages, as mentioned before. If the process would be understood in more detail it might as well spread in application. To this end, more knowledge about the process and the parameter variations needs to be generated and further process features have to be developed to make the process more attractive and user friendly.

## 4. Systematic Process Consideration

The systematic process consideration begins with the historical evolution of the process, called lifecycle curve (Fig. 15). This idealized “S” curve illustrates the performance of products or processes over time and is split into four sections. The first section describes the genesis of the product. At the beginning of the lifecycle, this performance is gently. The second section characterizes the growth and the third section the mellowing of the product, whereas the last one is the displacement section. Thereby another product displaces the product or the product is included into a super system as Eversheim (2003) generally describes.

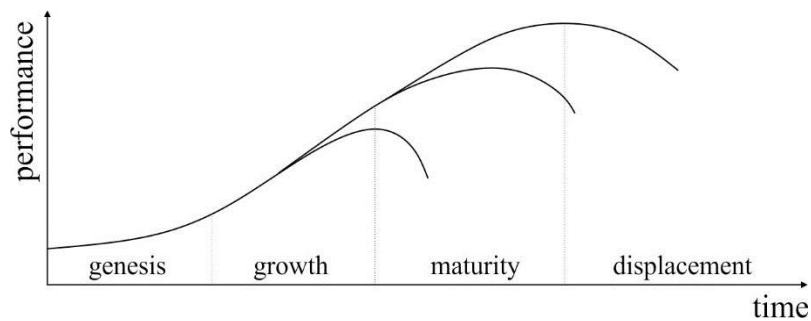


Fig. 15: Lifecycle curve (Eversheim 2003).

Several indicators, like count of innovations, success or patents, describe the position of the product within the “S” curve. In addition, the count of publications about a specific topic can be such an indicator as Fig. 16 shows.

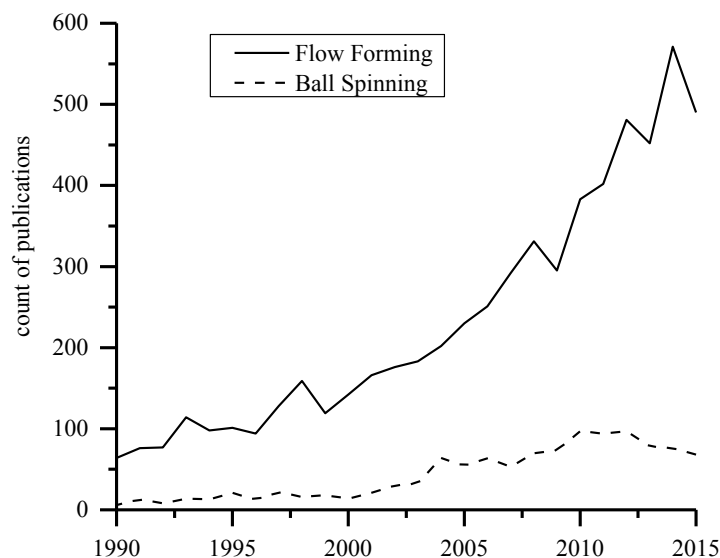


Fig. 16: Count of publications of Flow Forming and Ball Spinning.

From Fig. 16 it can be assumed, that flow forming is in the “growth” section, whereby no significant characteristics can be determined for the ball spinning. Ball spinning could be either in the “genesis” or in the “maturity” section.

One method for a systematic process consideration is the influence matrix. This matrix points out the schematic connections and dependences of different process parameters in a network. This process consideration is based on the subjective view of the observer (Lindemann, 2006). Generally, only the values of the dependent parameters are included into an influence matrix. With the enhancement of positive and negative values of the dependence, it is possible to illustrate the trend of influence on each parameter. The influence matrix in Fig. 17 is created with a range from - 6 (maximal negative influence) to + 6 (maximal positive influence). The parameters themselves need to have a nomenclature with a tendency, such as “higher axial feed rate” or “better surface quality”. The nomenclature is a tendency, which describe the easiest and cheapest way of a production. A separate evaluation of the positive and negative influences creates a cluster of points in an active and passive sum. Every parameter is mapped with two points, one with the positive influence and one with the negative influence (Kuss et. al., 2013).



The positive and negative influence parameters are mapped into an active/passive sum diagram (Fig. 18). Within the map, every parameter is split into two points, one for the positive and one for the negative influence. Points within the upper right corner are implying a critical positive influence whereas point within the lower left corner imply a critical negative influence. For example has the parameter “higher infeed” a critical negative influence to the ball spinning process.

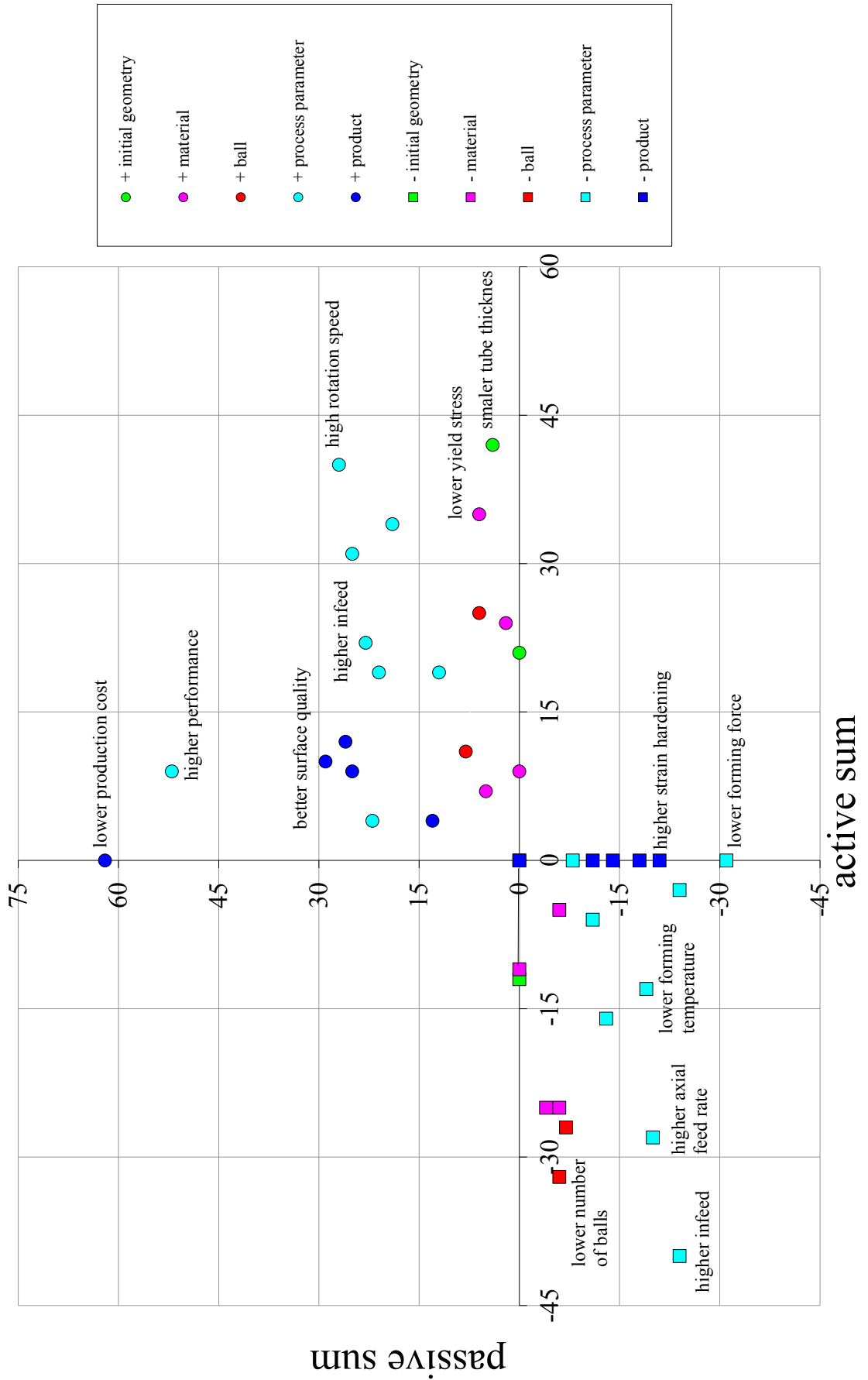


Fig. 18: Active and passive sum of the influence matrix for a ball spinning process.

By connecting the positive and negative influence points of each parameter, the influence range can be pictured (Fig. 19). This influence range is now correlating with the active and passive sum of each parameter, as depicted through the length of each range.

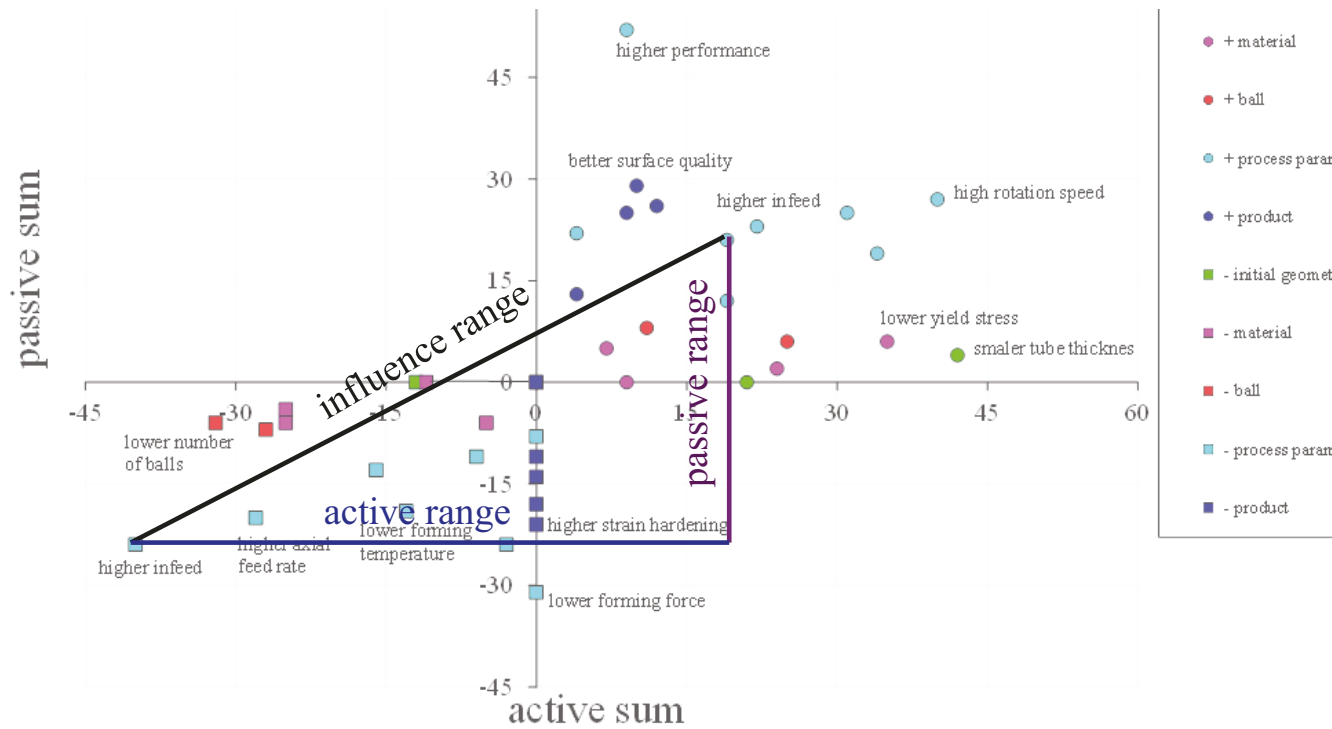


Fig. 19: Active/passive sum and influence range of one parameter.

The result of the influence matrix is displayed in Fig. 20. Every parameter is mapped with its active and passive influence range and its positive (+) or negative (-) influence. This analysis screens for example, that a high rotation speed has almost positive influence to other parameters and is itself positively influenced by other parameters. A higher axial feed rate influences other parameter in an equally positive and negative way, since the light purple bar is balanced between positive and negative side.

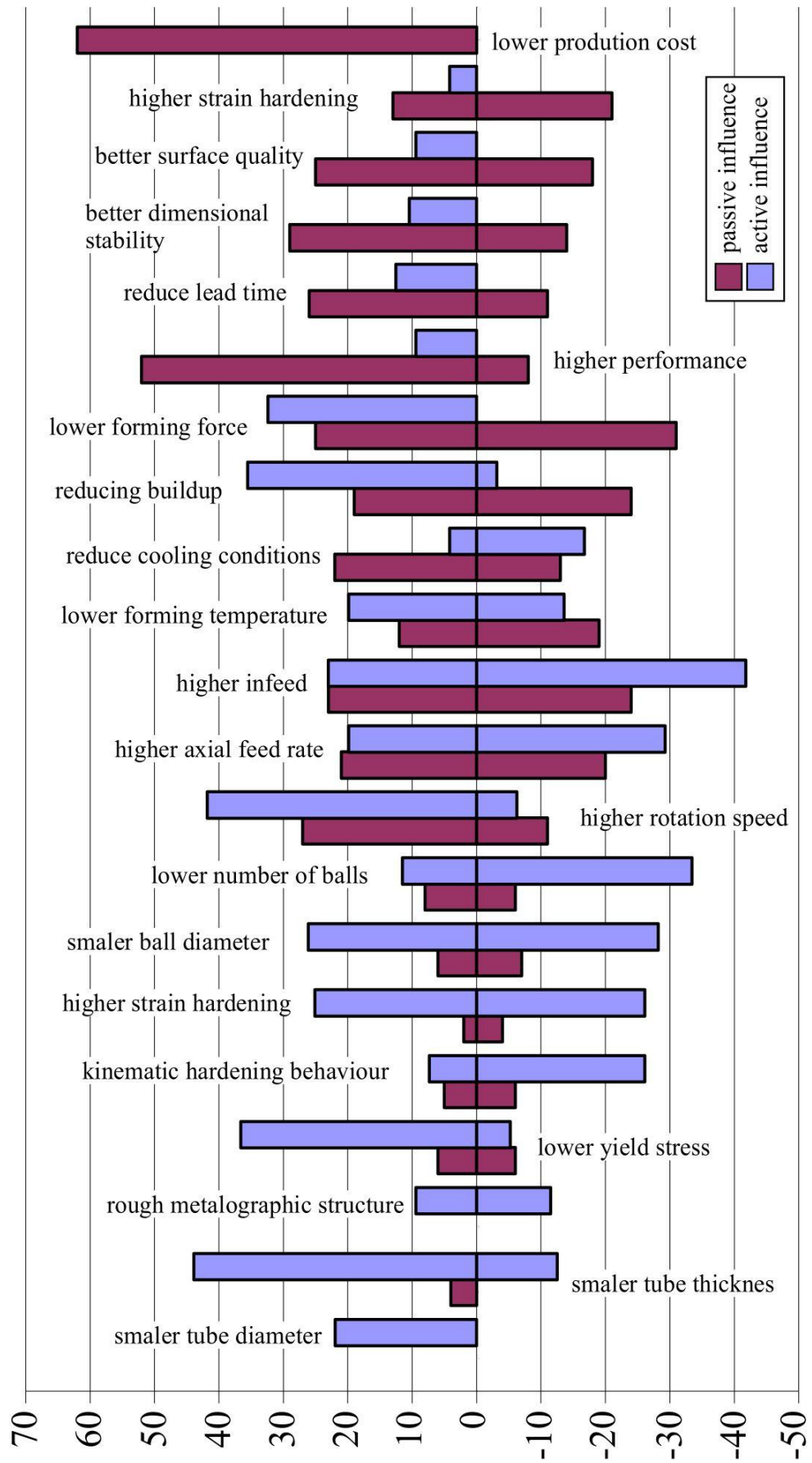


Fig. 20: Parameter influence on ball spinning.

In Fig. 21 and Fig. 22 the positive and negative influence on each parameter group of Fig. 17 is displayed in a vector diagram. The thickness of the arrows indicates the range of influence and the arrowhead points to the influenced parameter group. Arrows to the same parameter group signifies that some parameters influence each other in this group. The arrows with two arrowheads indicate an interaction between the parameters. Both graphics must be read in combination with Fig. 17. For example influence the process and product parameters the material in form of strain hardening and the microstructure. It is to note, that there is a strong positive influence of single parameters within the process parameter group.

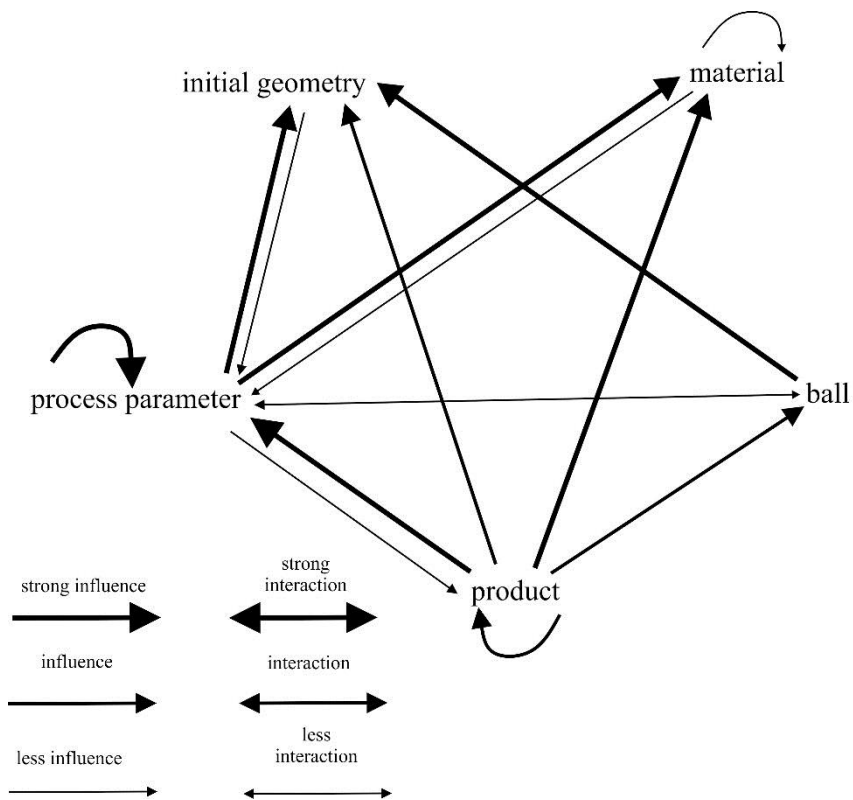


Fig. 21: Vector diagram of the positive influence on ball spinning.

The negative vector diagram shows for example, that the ball parameter has no negative influence on other parameters and that there is a mutual influence of parameters in the process parameter group.

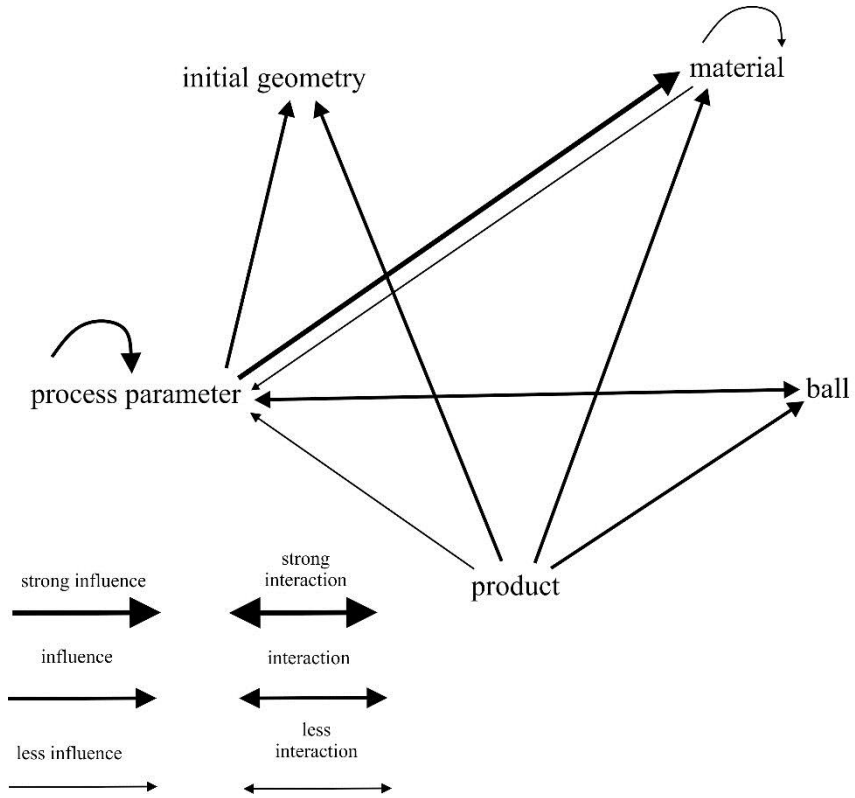


Fig. 22: Vector diagram of the negative influence on ball spinning.

Another method for process parameter influence evaluation is the TRIZ method (teoria reschenija isobretatjelskich sadatsch). This method enables the extraction and solution of technical contradictions. This method is separated and based on three foundations: systematics, knowledge and analogies. The category “knowledge” includes the contradiction-matrix. Altschuller (1984) inspected 200.000 patents for their method of resolution. He conceived a matrix with 39 parameters and 40 innovations. Such a process inspection supports the user to focus on special problems. Beginning by the parameters in Fig. 20, contradictions are listed and solutions are formulated (Eversheim 2003).

- **force - velocity:**

- make dynamic => seesawing system for the tool or cylinders

*The production of gas bottles with a flow forming process uses a seesawing kinematic. A similar kinematic could also reduce the forming forces for the ball spinning process.*

- **force - form:**

- previous actions => displaced tool position for bigger balls

*The ball diameter influences the roller angle and therefore the deformation forces. Bigger balls could be used for a previous deformation; the deformation forces would be lower.*

- **force - temperature:**

- separation of the location => inductive heating in front of the deformation zone

*Similar to a friction spinning process (Hombberger, 2009), an inductive heating in front of the deformation zone could reduce the deformation force.*

- change aggregate state => deformation at temperatures of recrystallization

*The deformation force could be reduced at hot (~1200°C) or warm (~600°C) temperatures.*

- **force – manufacturing precision:**

- periodic effects => change of the feed rate (grooves at the surface)

*Grooves can occur for thin tubes and high axial feed rates at the outer side during an expansion process. A reduced axial feed rate for the finishing could reduce the deformation force and improve the manufacturing precision.*

- **manufacturing precision – length of moveable parts:**

asymmetry => count of tools, form of tools (cylinder/needle)

*A combination of different tool geometries in a step tool could increase the manufacturing precision.*

## 5. Finite Element Simulation of Flow Forming and Ball Spinning

There are many different methods to simulate flow forming or ball spinning processes. FEM is used from 2D simulations for a first overview of the process behaviour as Hong et. al. (1998) describes, to a detailed elastic-plastic 3D simulation shown by Hua et. al. (2005). Houillon et.al. (2011) compared a Lagrangian formulation with an ALE method for a flow forming process. Compared with the conventional simulation of forming processes, the simulation of incremental forming processes are strongly coupled with a high number of new contact condition. This fact causes a long computing time (Ufer and Awiszus 2005).

The 2D simulation of flow forming or ball spinning processes is characterised by a rigid tool with no friction condition or with a radial oscillating tool with friction condition. For the second method, the frequent of the oscillation is calculated by the axial feed rate and the rotational speed of the workpiece. The ovality during the deformation forces ( $F$ ) has to be respected by radial displacement of the tool ( $C$ ) as a function of axial distance ( $z$ ), diameter ( $dw$ ) and rotational speed ( $n$ ) as shown in Fig. 23.

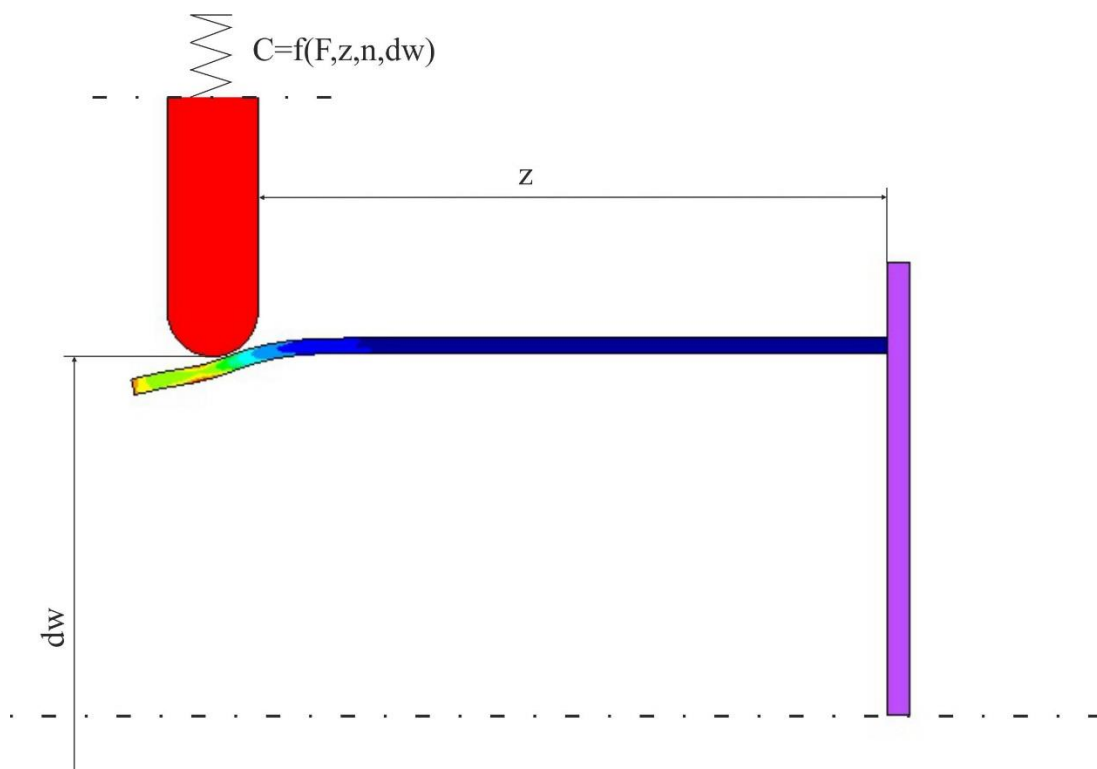


Fig. 23: 2D FEM simulation of flow forming.

One way to optimize a 3D FEM simulation is to use symmetry areas. Wang and Zhao (2015) use symmetry areas to reduce the count of elements for the simulation of a ball spinning process for inner groove copper tubes as depicted in Fig. 24.

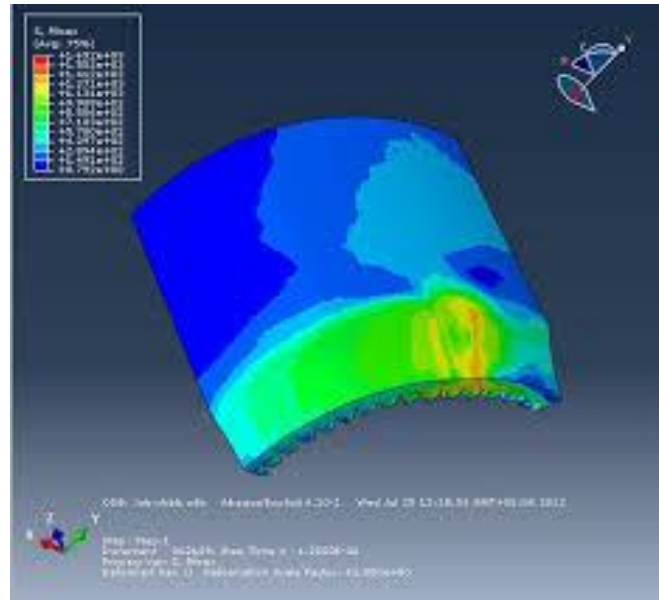


Fig. 24: 3D Simulation of ball spinning with symmetry areas (Wang and Zhao 2015).

Full 3D simulations can be optimized by using the right kinematic structure of the model. It depends on the possibilities of the FEM software and on the complexity of the process. There are three different structures for the ball spinning expansion process. Fig. 25 1) pictures a fixed workpiece for which the mesh does not have to be manipulated in the simulation. In 2) the positions of the balls fixed and in 3) the workpiece and the balls rotates around the inner leading ring.

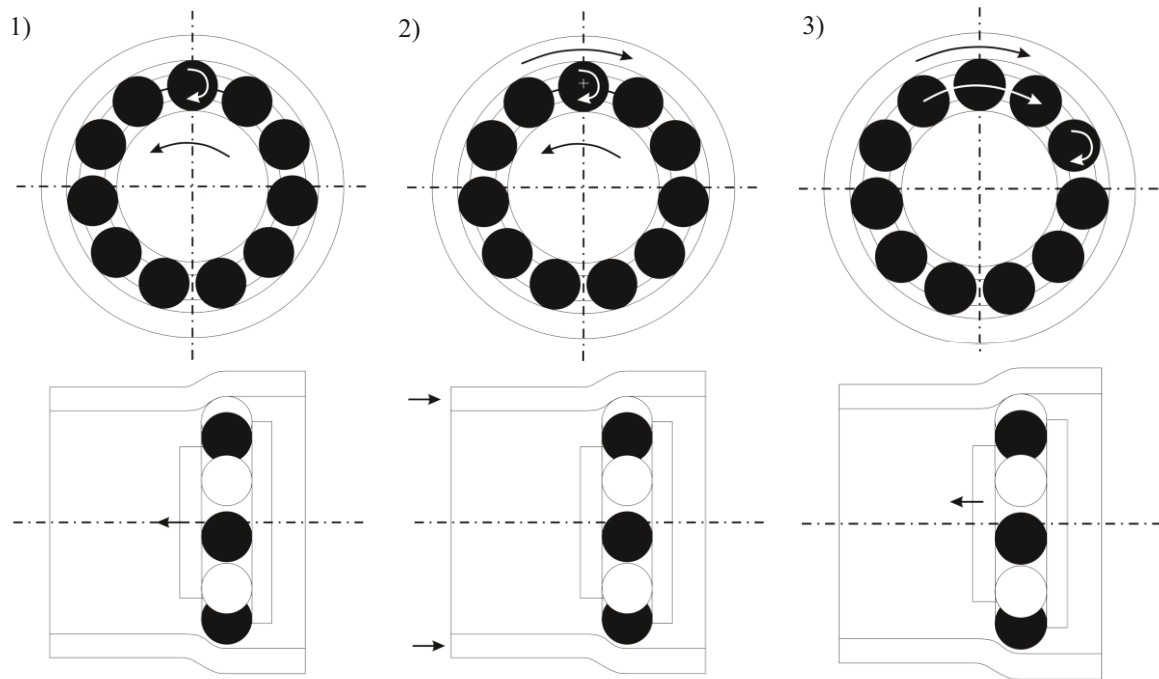


Fig. 25: Kinematic structure of a ball spinning expansion process.

The required accuracy of the simulation is corresponding with the size of one element within the mesh. Flow forming and ball spinning is characterized by their deformation near the surface, hence, the mesh has to be optimized and fined at the regions of interest. Fig. 26 illustrates thus an optimization of the mesh, to calculate the deformation gradient of this process in a correct way.

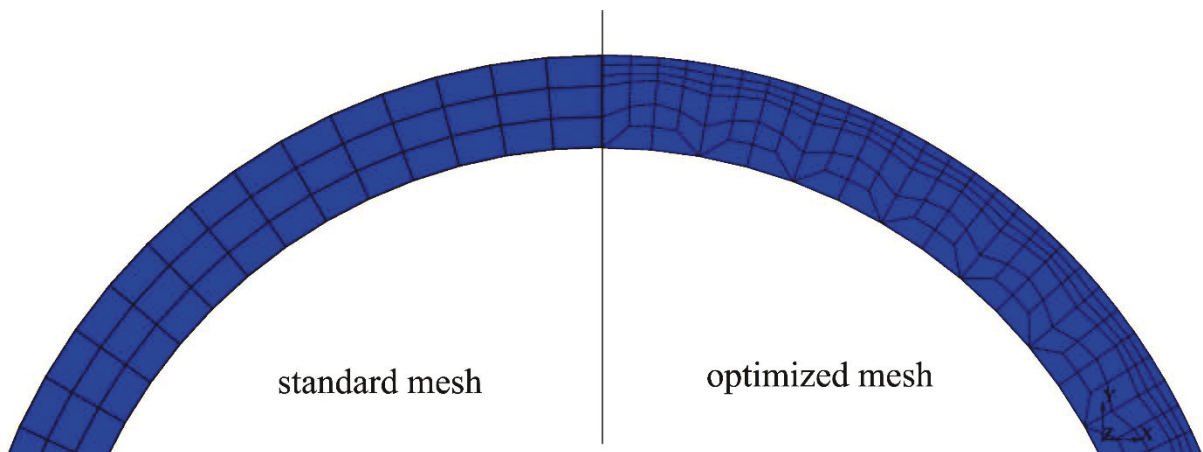


Fig. 26: Standard mesh and optimized mesh for a ball spinning or flow forming process.

Another important effect for the stability of the simulation is the ball – workpiece contact. Abaqus/Standard offers to the “Hard Contact”, “Softened Contact”. Thereby, it is possible to define the stiffness of the pressure – overclosure curve. This effect depends on the process and material behaviour and can be imitated by the theory of Hertz (1881). Hence, the contact area can be expanded during a constant element length (Fig. 27).

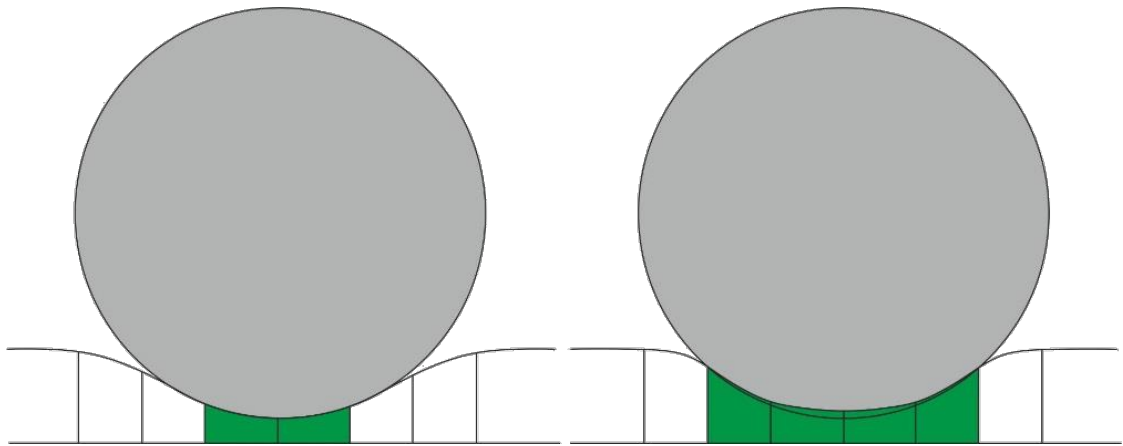


Fig. 27: Contact area for hard (left) and softened (right) contact.

For all incremental forming processes a high count of increments is required to simulate the changing contact situation. Some FEM software offer a strict increment definition. It is possible to combine the contact situation with finer increments and for the manipulation to the next contact area between tool and nodes of the mesh a mounting number of increments. Fig. 28 displays the increments and therefore the position of the nodes passing through the contact area.

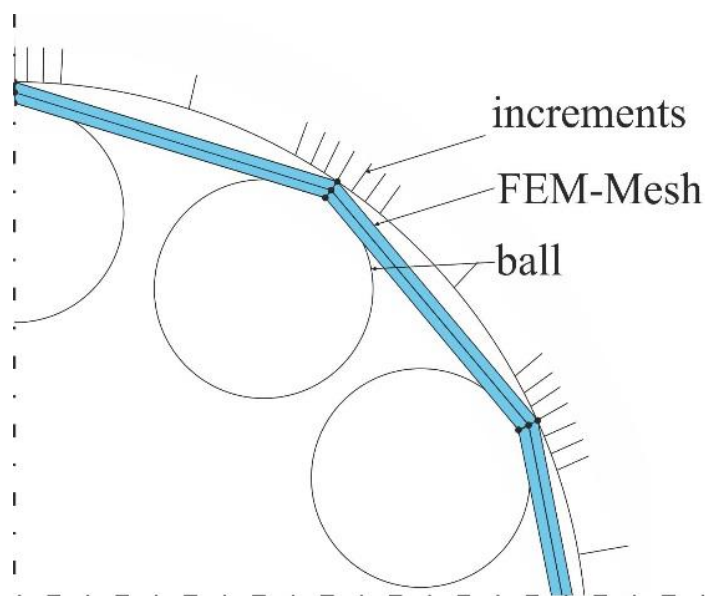


Fig. 28: Increments at the contact area and between the tools.

Generally is the FEM simulation a compromise between effort, quality and speed as pictured in Fig. 29 (Ufer, 2006). The focus of the simulation depends on required precision, kind of evaluation and available resource.

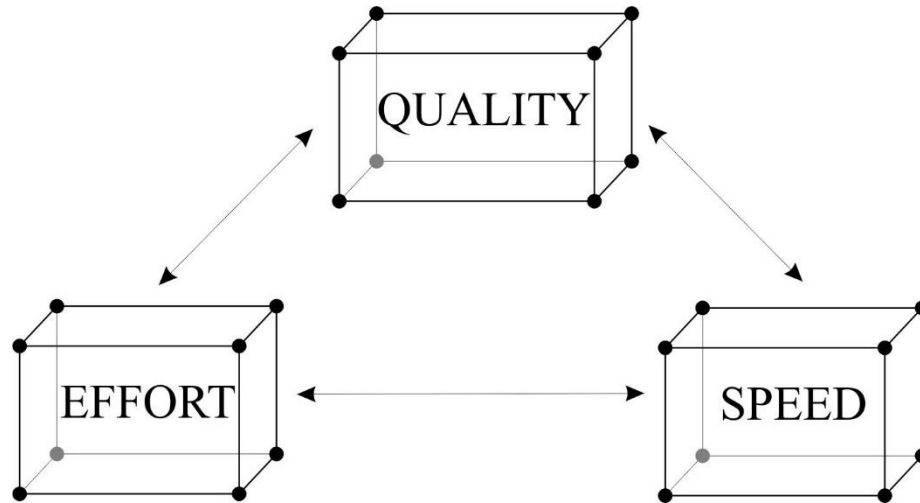


Fig. 29: Compromise of effort, quality and speed.

## 6. Radial Forging versus Flow Forming

### 6.1 Model Set Up

The next related process of flow forming is radial forging. Both processes are generally used to produce axisymmetric forms. The workpiece is similar to flow forming turned by a tailstock and a mandrel. The tool is composed of four hammers which encloses the workpiece as displayed in Fig. 30. The hammers oscillate radially and the tailstock turns the workpiece during an axial feed.

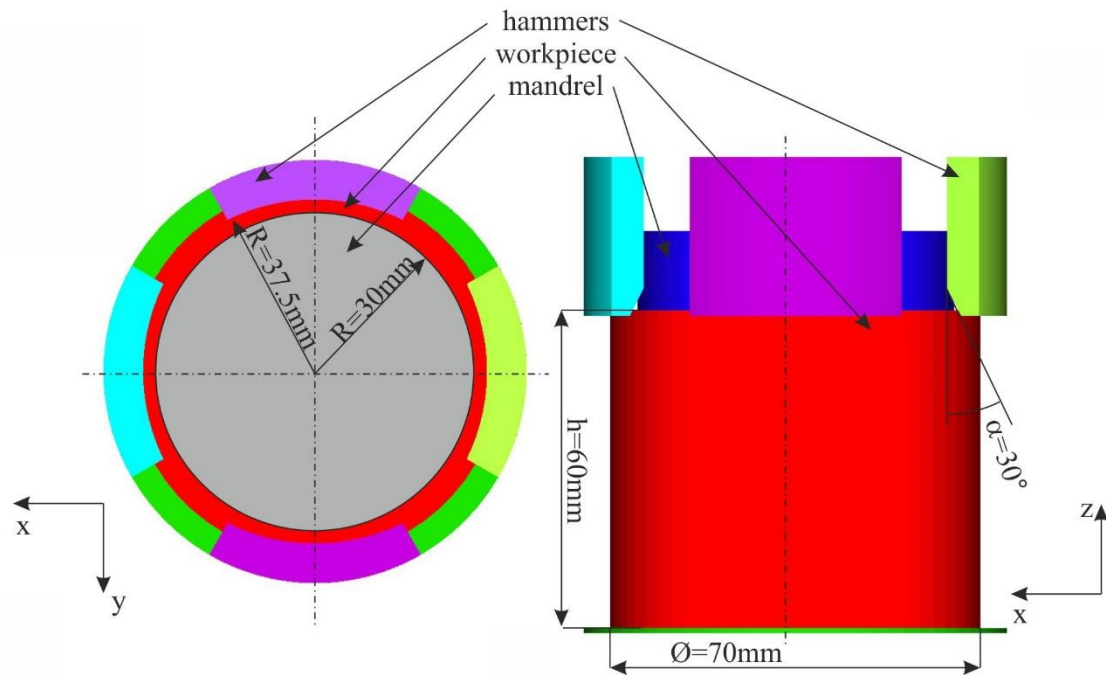


Fig. 30: Model set up of a radial forging process.

To compare radial forging with flow forming, two FEM models are created with the same geometrical attributes. The model set up for the flow forming process is depicted in Fig. 31. The simulations are computed with the software Simufact.

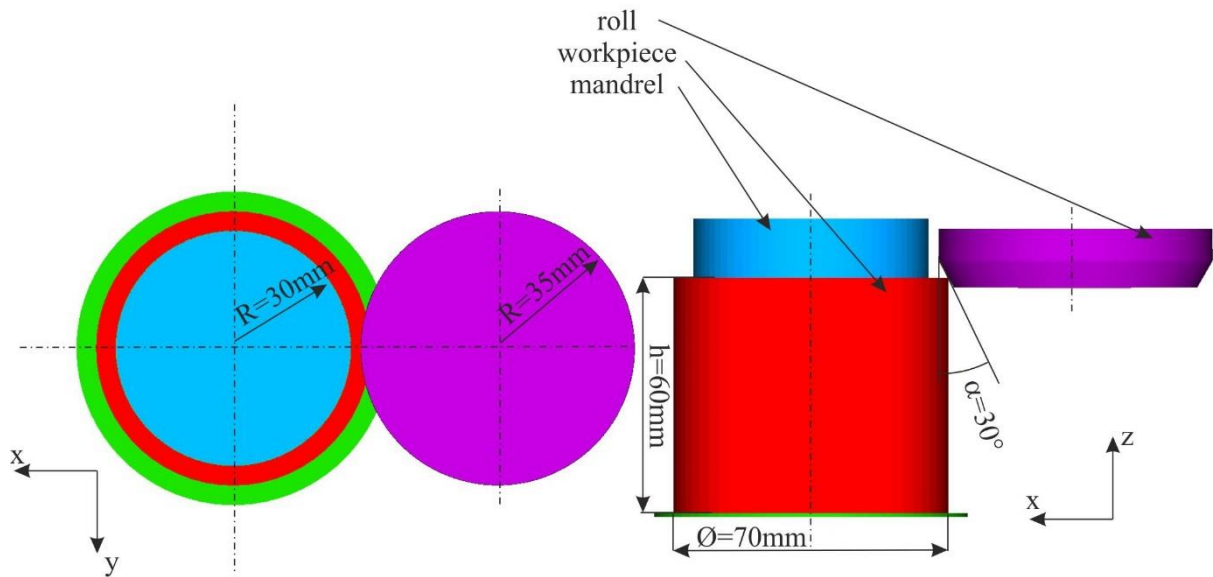


Fig. 31: Model set up of a flow forming process.

The used material data for the workpiece was 1.4301 from the material database from Simufact and the tools are made of H13. The friction boundary was a shear stress model with 0.3 and the process parameters are listed in Table 1. To estimate the different deformation behaviour, two tubes with 5mm and 16mm thickness are simulated.

Table 1: Process parameter for radial forging and flow forming.

process	radial forging	flow forming	
strokes	667	31.5	-
lift	3		mm
rotation step	17		°
axial feed rate	0.5	0.5	mm/sec
time	40	40	sec
infeed	2.5	2.5	mm
deformed volume	10.6	10.6	cm <sup>3</sup>

## 6.2 Results of the Comparison of Radial Forging and Flow Forming

The deformation zone between radial forging and flow forming are generally identically as seen in Fig. 32. Both processes have a radial build-up in front of the deformation zone at the inner diameter. Additionally, the flow forming process obtains a radial bulge at the outer diameter in front of the deformation zone. These two effects can be modified by the tool geometry, the axial feed rate, and the infeed of the process.

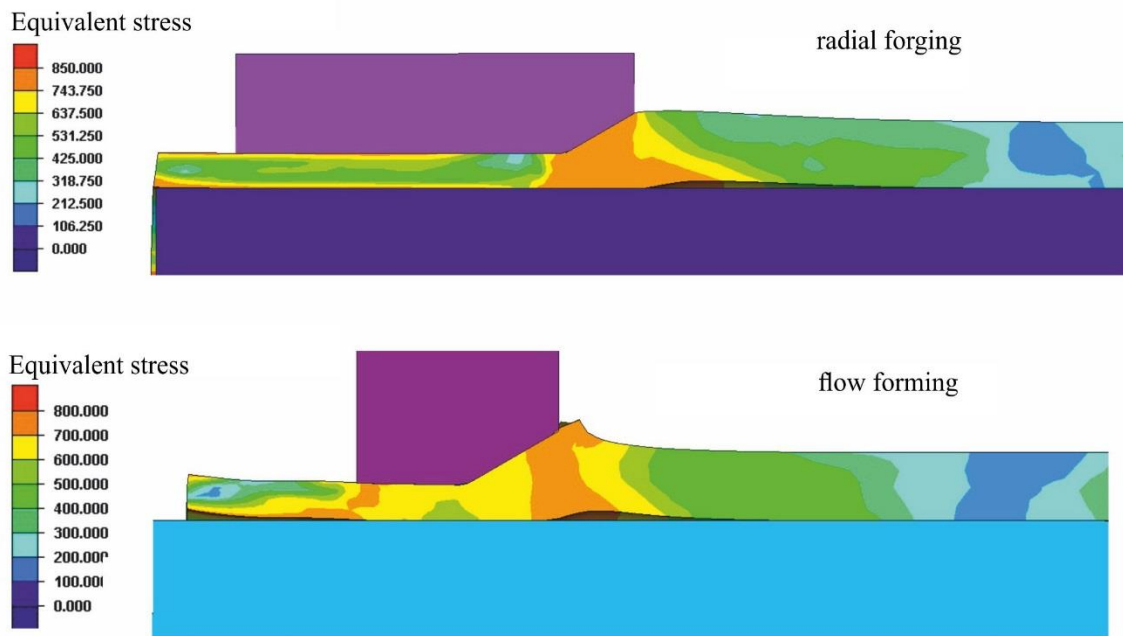


Fig. 32: Comparison of the equivalent stress between radial forging and flow forming

(Kuss et. al. 2014).

Fig. 33 and Fig. 34 picture the influence of the deformation gradient of the tube thickness during radial forging and flow forming. It can be seen, that flow forming deforms the surface of the workpiece in a more intensive way as radial forging. The deformation gradient of radial forging is lower than during flow forming. Therefore, radial forging is more practicable to deform the whole workpiece and flow forming can be applied to deform near to the surface with an injection of compressive stresses.

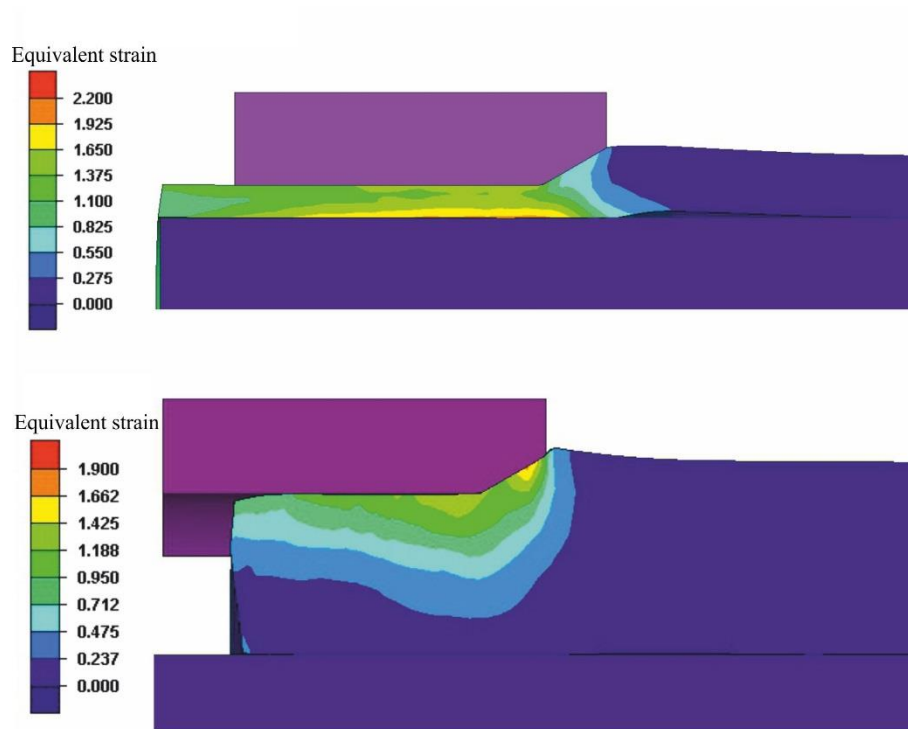


Fig. 33: Influence on the deformation gradient of the tube thickness during radial forging (Kuss et. al. 2014).

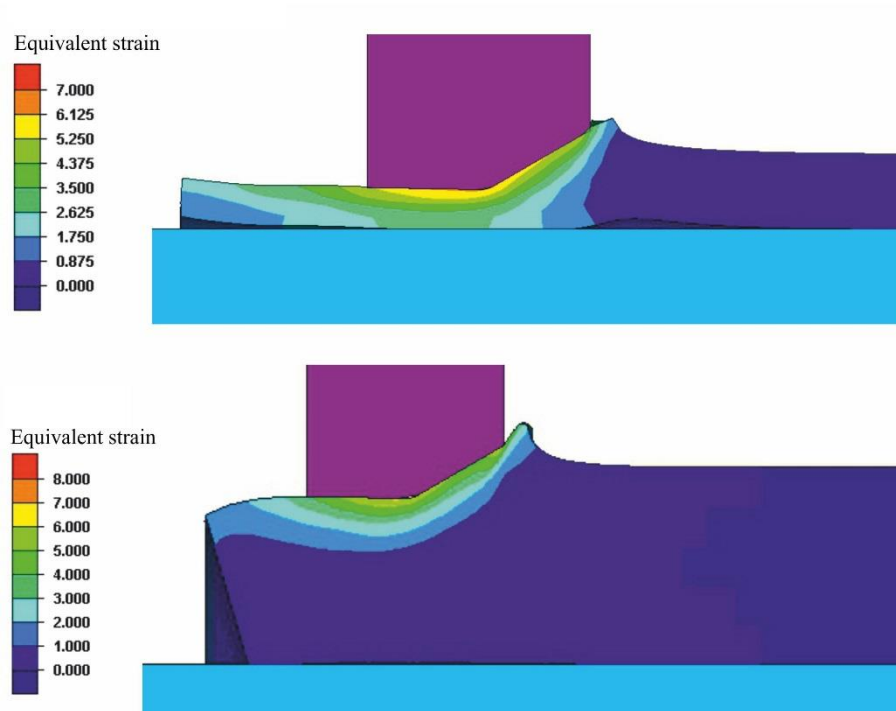


Fig. 34: Influence on the deformation gradient of the tube thickness during flow forming (Kuss et. al. 2014).

## 7. Forming Forces of Ball Spinning

### 7.1 Analytical Calculations

The forming forces of incremental forming processes are relatively low due to the small contact area. The ball spinning process is characterized by several incremental forming zones acting simultaneously. According to the fact, that numerical simulations of incremental forming processes require a long computing time, an analytical calculation of the forming forces is useful for a quick estimation. In addition, the analytical calculation gives an idea of the forming forces by a variation of process parameters.

To the authors' knowledge, no analytical study of a ball spinning expansion process has been performed yet. However, there are some articles which engage the analytical calculation of the ball spinning reduction process. Wenke (1973) used the approach from Thamasett (1961) and applied it to a ball spinning processes. Heidel and Kühmel (1979) analysed the ball spinning process by using the penetration of a ball into a plane analytically. Rotarescu (1994) created an algorithmic form of the analysis, which is suitable for computer applications. Li et. al. (2002) explored the influence on process parameters on the ball spinning process with theoretical and experimental analyses.

In the following section, a new analytical expression for a ball spinning expansion process is developed and the parameters for the calculations are listed in Table 2. Parts of these chapter are published by Kuss et. al. (2015).

Table 2: Nomenclature and parameters for the analytical calculation of the ball spinning.

parameter	value	unit
r ball radius	3.325	mm
D <sub>i1</sub> workpiece inner diameter before forming	33.500	mm
D <sub>i2</sub> workpiece inner diameter after forming	35.000	mm
x <sub>r</sub> radial reaming before forming	0.350	mm
v axial feed rate	0.600	mm/rev
n number of balls	11	-
k <sub>f</sub> flow stress	480	N/mm <sup>2</sup>
η efficiency of plastic deformation	0.8	-

The analytical calculation of the forming forces is based on the flow law, as shown by Siebel (1932).

$$F = k_f \cdot A \quad (1)$$

The forming force ( $F$ ) is the multiplication of the flow stress ( $k_f$ ) and the contact surface ( $A$ ), therefore, the calculation is based on an ideal plastic material behaviour.

At first, a ball segment ( $A_k$ ) with a height of  $h$  is calculated (Fig. 35).

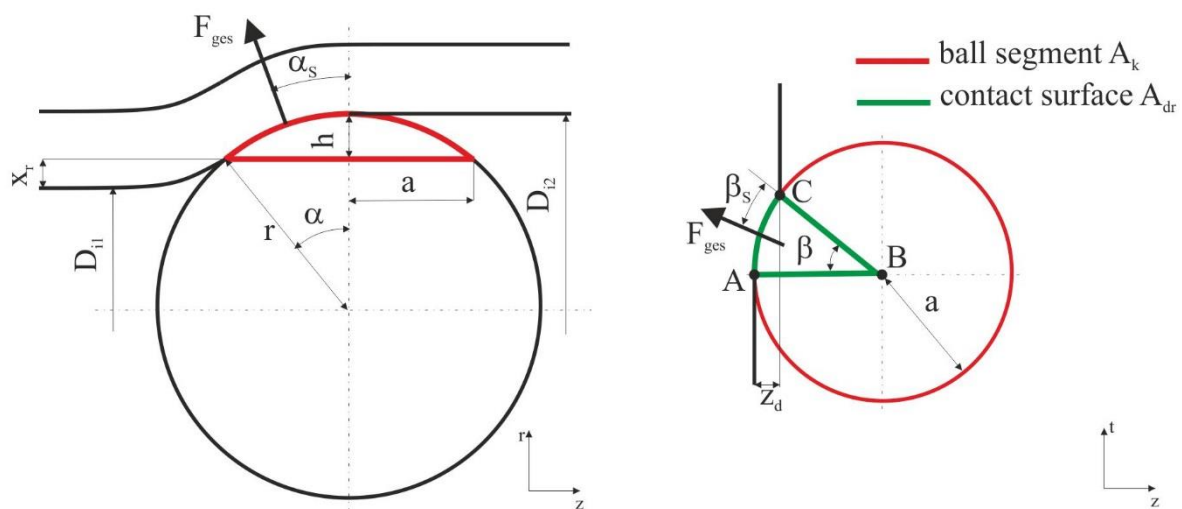


Fig. 35: Visualization of the parameters for the analytical calculation.

$$A_k = \pi \cdot (2 \cdot r \cdot h + a^2) \quad (2)$$

$$h = \frac{D_{i2} - D_{i1}}{2} - x_r \quad (3)$$

$$a = \sqrt{r^2 - (r - h)^2} \quad (4)$$

The radial bend up of the tube in front of the contact zone  $x_r$  (Fig. 35), depends on the geometry and the material behaviour of the tube. For this investigation, a finite element method (FEM) simulation predicts  $x_r$ . The parameter can also be determined experimentally.

$$0 < x_r \leq \frac{D_{i2} - D_{i1}}{2} \quad (5)$$

$$x_r = f(E, k_f, D_a, D_{i1}, D_{i2}) \quad (6)$$

Secondly, the contact surface  $A_{dr}$ , which is a sector of the ball segment ( $A_k$ ), is calculated by the process parameter  $z_d$  (Fig. 36).

$$z_d = \frac{v}{n} \quad (7)$$

$$\beta = \arccos\left(\frac{r - z_d}{r}\right) \quad (8)$$

$$A_{dr} = \frac{A_k}{2 \cdot \pi} \cdot \beta \quad (9)$$

Hence, the contact surface  $A_{dr}$  is a spherical triangle on each ball of the tool (Fig. 36).

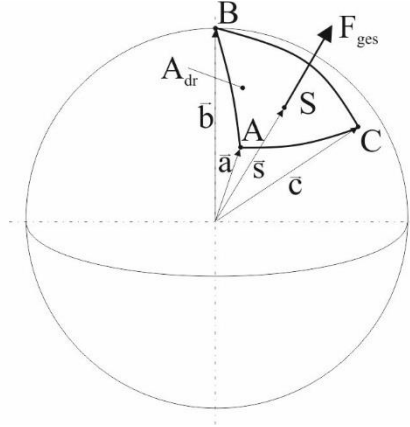


Fig. 36: Visualization of the contact surface and the gravity centre S.

The resulting forming force ( $F_{ges}$ ) is the flow stress ( $k_f$ ) times the contact surface ( $A_{dr}$ ) divided by the efficiency of deformation ( $\eta$ ). For real processes  $\eta$  is reported to be between 0.7 and 1 as explained by Doege and Behrens (2010).

$$F_{ges} = \frac{k_f \cdot A_{dr}}{\eta} \quad (10)$$

$A$ ,  $B$  and  $C$  are the corners of the contact surface and  $\vec{a}$ ,  $\vec{b}$  and  $\vec{c}$  are the vectors of those points from the ball centre (Fig. 35, Fig. 36). It is assumed that there is a constant contact pressure over the contact surface. Therefore, the resulting forming force  $F$  acts in the gravity centre  $S$ . Using Eq.10 to Eq.12 the vector  $\vec{s}$ , which is pointing from the ball centre to  $S$ , can be calculated.

$$\vec{a} = \begin{pmatrix} r-h \\ 0 \\ a \end{pmatrix} \quad \vec{b} = \begin{pmatrix} r \\ 0 \\ 0 \end{pmatrix} \quad \vec{c} = \begin{pmatrix} r-h \\ \sqrt{r^2 - (r-z_d)^2} \\ z_d \end{pmatrix} \quad (11)$$

$$\vec{s} = \frac{r \cdot (\vec{a} + \vec{b} + \vec{c})}{|\vec{a} + \vec{b} + \vec{c}|} \quad (12)$$

The angles of the resulting forming force (Fig. 36) are calculated by the components of the vector  $\vec{s}$ .

$$\alpha_s = \arctan\left(\frac{s3}{s1}\right) \quad (13)$$

$$\beta_s = \arctan\left(\frac{s2}{s3}\right) \quad (14)$$

Finally, the resulting forming force is separated into the axial, radial and tangential components.

$$F_Z = F_{ges} \cdot \sin(\alpha_s) \cdot \cos(\beta_s) \cdot n \quad (15)$$

$$F_R = F_{ges} \cdot \cos(\alpha_s) \cdot \cos(\beta_s) \cdot n \quad (16)$$

$$F_T = F_{ges} \cdot \sin(\beta_s) \cdot n \quad (17)$$

With the analytical calculation, it is possible to predict the forming forces in each direction. The calculation is based on an ideal plastic material behaviour and does neither include temperature nor hardening effects. Based on the flow law it is possible to calculate the influence on the process and geometric parameters on the forming forces.

The drive torque  $M_A$  is also important for the estimation of the expansion process. The calculation of  $M_A$  is based on the resulting forming force  $F_{ges}$  and frictional force  $F_F$  (Fig. 37).

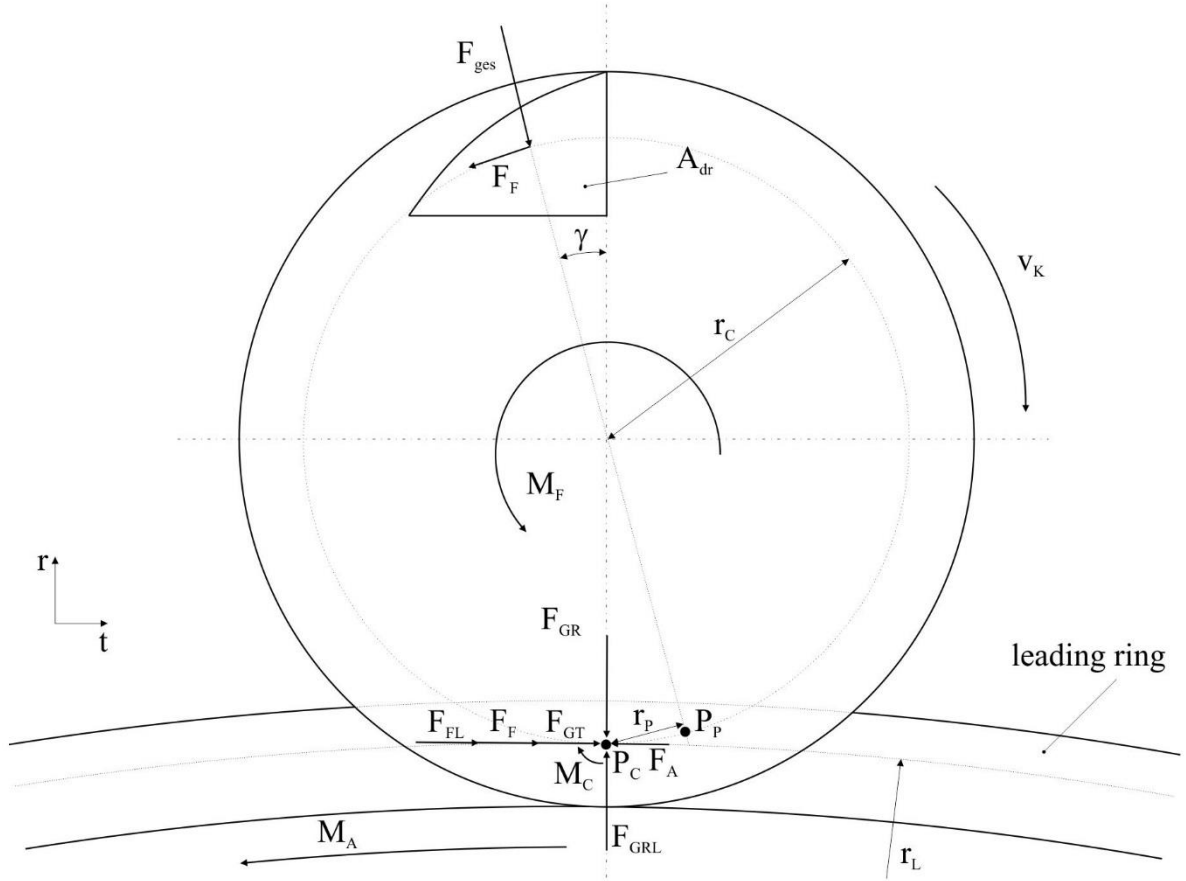


Fig. 37: Visualization of the forces on the ball and the leading ring.

Klocke and König (2006) describe, that during the high contact pressure and the plastic deformation of the tube, the shear frictional stress law is useful (Eq.18).

$$\tau_R = m \cdot k = m \cdot \frac{k_f}{\sqrt{3}} \quad (18)$$

$$F_F = \tau_R \cdot A_{dr} \quad (19)$$

It is assumed that the frictional force  $F_F$  acts in the opposite direction of the turning speed of the ball  $v_K$ . Therefore the friction moment  $M_F$  is calculated with the radial distance  $r_C$  to the ball center.

$$r_C = r \cdot \cos(\alpha_s) \quad (20)$$

$$M_F = F_F \cdot r_C \quad (21)$$

The resulting forming force is displaced from the projection point  $P_P$  to the contact point  $P_C$ , whereby the moment  $M_C$  results.

$$r_P = r_C \cdot \sin(\gamma) \quad (22)$$

$$M_C = F_{ges} \cdot r_P \quad (23)$$

To split the forming force, the angle  $\gamma$  is calculated.

$$\alpha = \arcsin\left(\frac{a}{r}\right) \quad (24)$$

$$\gamma = \arcsin(\sin(\beta) \cdot \tan(\alpha)) \quad (25)$$

The reaction force is split into a radial component  $F_{GR}$  and a tangential component  $F_{GT}$ .

$$F_{GT} = F_{ges} \cdot \sin(\gamma) \quad (26)$$

$$F_{GR} = F_{ges} \cdot \cos(\gamma) \quad (27)$$

The radial component  $F_{GR}$  is compensated by the radial leading ring force  $F_{GRL}$ .

$$F_{GR} = -F_{GRL} \quad (28)$$

Due to the fact that no plastic deformation between the ball and the leading ring occurs, the frictional force at the leading ring  $F_{FL}$  is calculated by the coulomb friction. The drive torque  $M_A$  needs to be higher than the moment of the frictional force  $F_F$ , the frictional force at the leading ring  $F_{FL}$  and the tangential component of the displaced resulting forming force  $F_{GT}$  (Eq.31).

$$r_L = \frac{D_{i2}}{2} - r - r_C \quad (29)$$

$$F_{FL} = F_{GR} \cdot \mu \quad (30)$$

$$M_A \geq n \cdot r_L \cdot (F_{FL} + F_F + F_{GT}) \quad (31)$$

## 7.2 Experimental Investigation of the Forming Forces

In the experiments a welded tube ( $\varnothing$  35 mm x 1.5 mm and a length of 70 mm) composed of the austenitic stainless steel 1.4301 was used as workpiece. The tool was made of a ball bearing type SKF 7203-B-TVP with 11 balls. The thickness of the tube was reduced to 0.75 mm to lower the axial force (Fig. 38).

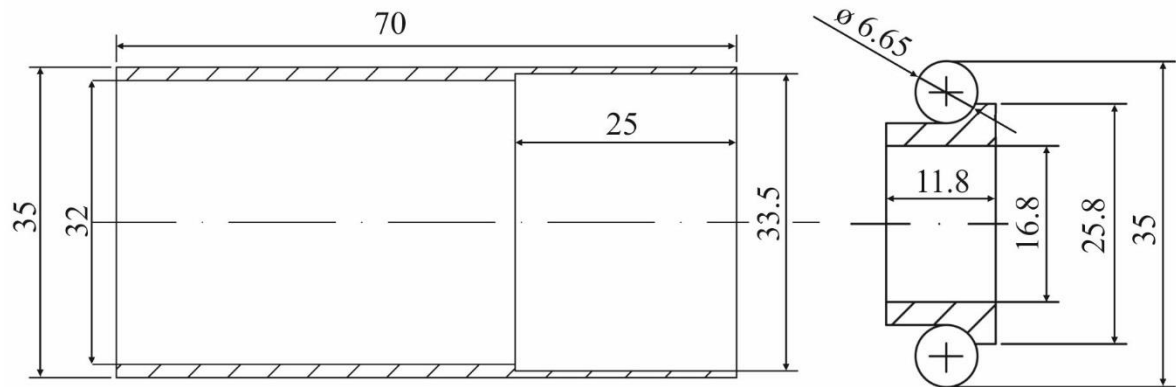


Fig. 38: Tubular workpiece and tool geometry.

The experiments are carried out on a friction-welding machine at the Chair for Metal Forming at the Montanuniversitaet Leoben (Fig. 39). During the experiments, the axial force was measured by a load cell between tool support and hydraulic cylinder support.



Fig. 39: Experimental setup of the friction welding machine.

The design of experiments includes seven experiments with different rotations speeds and axial feeds, which are listed in Table 3.

Table 3: Design of experiments for measure the forming force.

ID	turning speed [rev/min]	axial feed [mm/s]	axial feed rate [mm/rev]
1	100	1.0	0.600
2	194	1.3	0.402
3	194	1.8	0.557
4	194	2.0	0.619
5	194	3.3	1.021
6	500	1.0	0.120
7	500	1.3	0.156

---

### 7.3 FEM Simulation for the Forming Forces

In addition to the experiments, a FEM simulation is performed to obtain the axial force and the final geometry of the tube after the ball spinning process. Fig. 40 shows the assembly of the FEM simulation. The manipulator powers the tube, which is brought about by a fixed contact condition between manipulator and tube. The high friction value of  $\mu = 0.5$  between tube and balls is required to stabilize and turn the balls in the simulation. The balls can turn freely and the leading ring supports the axial force. The leading ring can turn freely in axial direction. The material data are taken from the database of the simulation software SIMUFACT, which cannot be published in this investigation. Flow curves of steel grade 1.4301 and the tool steel H13 are used for the tube and for the tools respectively. Generally, the process is performed as an isotropic thermo-elasto-plastic simulation starting with an ambient temperature of 20°C. For the workpiece hexagonal elements with an axial length of 1 mm and four elements over the thickness without a remeshing criteria are used. The parameter variations in the simulation are identical to the experiments as shown in Table 2.

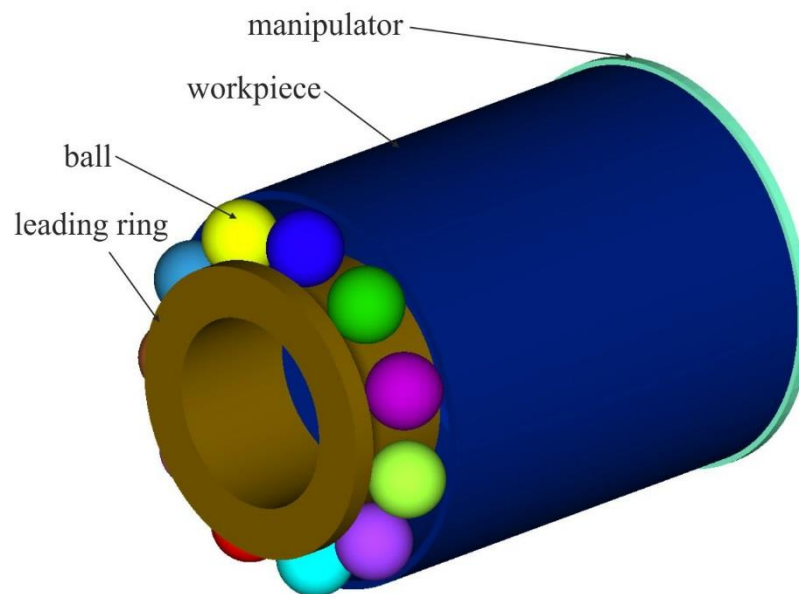


Fig. 40: Set up of the ball spinning FEM model.

Due to the relaxation of the internal stresses during the cutting of the real tube, also the axial cut is simulated. This is done by deleting half of the elements in axial direction. Hence, it is possible to compare the axial contour of the simulation with those of the experiment.

## 7.4 Comparison of the Axial Forming Force

After the forming process, the workpiece was axially sliced and a metallographic section has been prepared (Fig. 41).

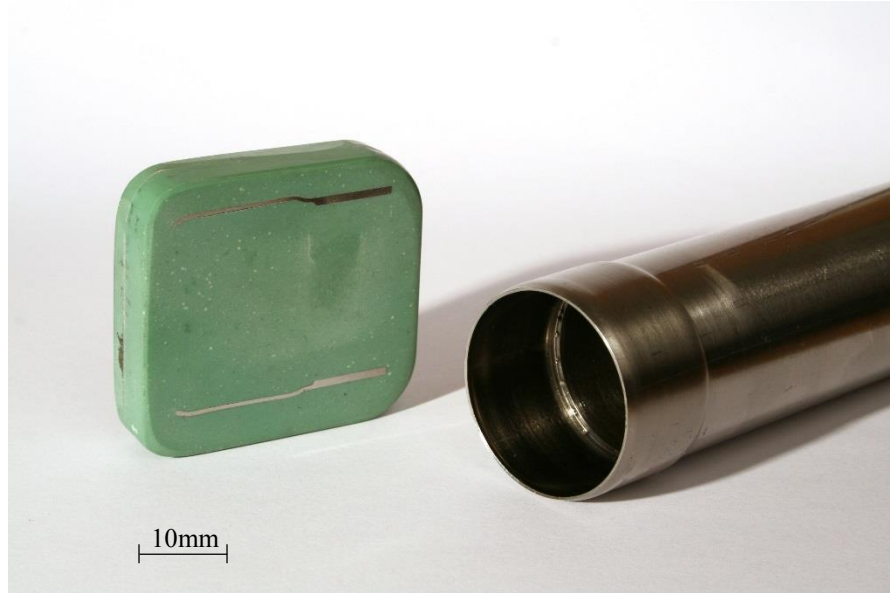


Fig. 41: Formed workpiece and metallographic section.

The final geometry of the metallographic section (ID4) was measured by a stereo microscope and compared with the results of the FEM simulation in Fig. 42.

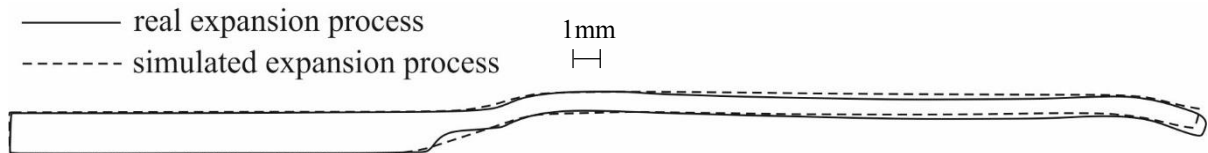


Fig. 42: Comparison of the experimental result ID 4 with the FEM simulation in an axial section.

Fig. 43 shows the different stages of the axial force  $F_z$  during the forming process. The first stage (I) is the first contact and radial bending of the tube edge. In the second stage (II), the workpiece is bended over the balls and the axial force increases about 45%. In the third stage (III), the tube edge is bended radially inward. This mechanism is caused by the tube stiffness. The last stage is the steady state zone (IV).

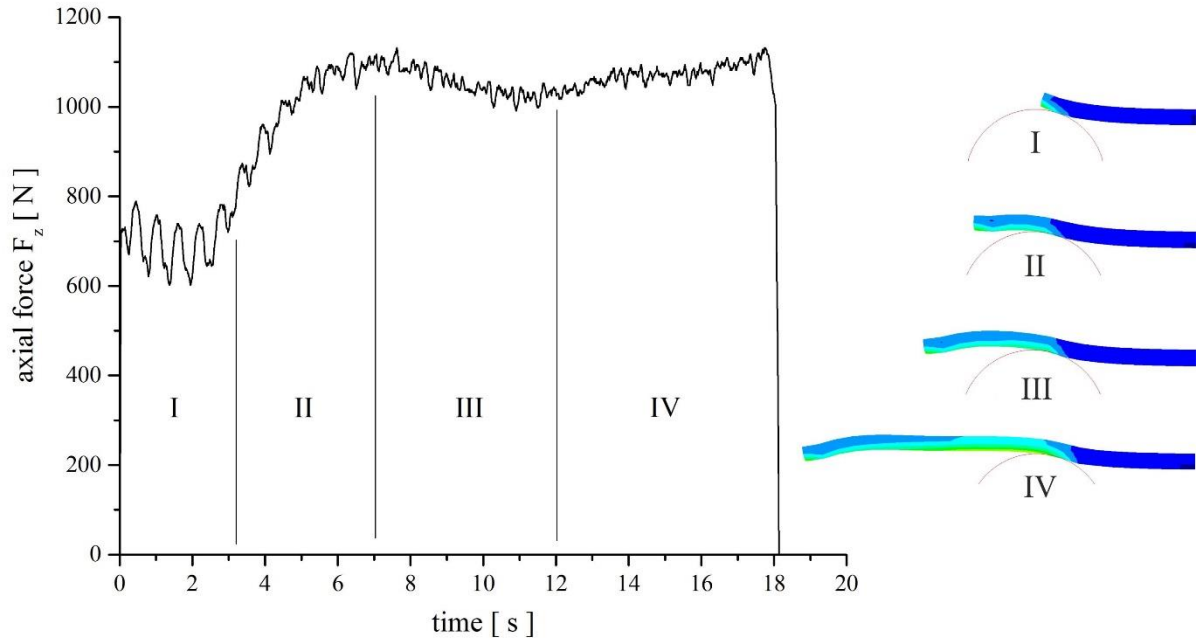


Fig. 43: Stages of the axial forming force  $F_z$  (experiment ID4).

The axial force can be calculated by inserting the values listed in Table 2 and Table 3 into the Eq.2 to Eq.17. Fig. 44 compares the steady state zone of the experimental axial force to the simulated and calculated axial force. The medial deviation between experiment and calculation is 135N, between calculated and simulated results 114N and between simulation and experiment 130N.

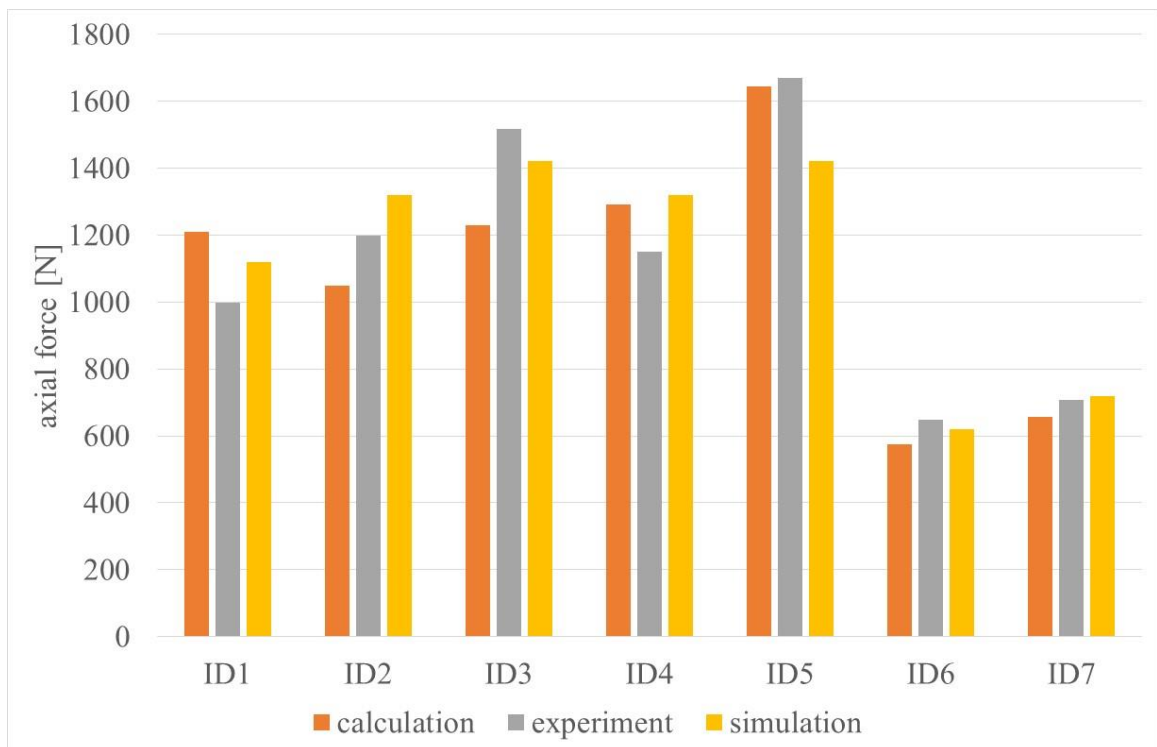


Fig. 44: Axial force comparison of analytical calculation, experiment and simulation.

## 7.5 Metallography after the Ball Spinning Expansion Process

Fig. 45 displays the micrograph of the basic structure and the welding seam before (left) and after deformation (right). Fig. 46 shows the microstructure of the basic structure at the outside (A1) and the inside of the tube (A3) and the texture of the welding seam at the outside (A2) and at the inside of the tube (A4) before the deformation. No differences can be observed between the outside and the inside microstructures, hence, it can be assumed that the inside and outside are of equal microstructure.

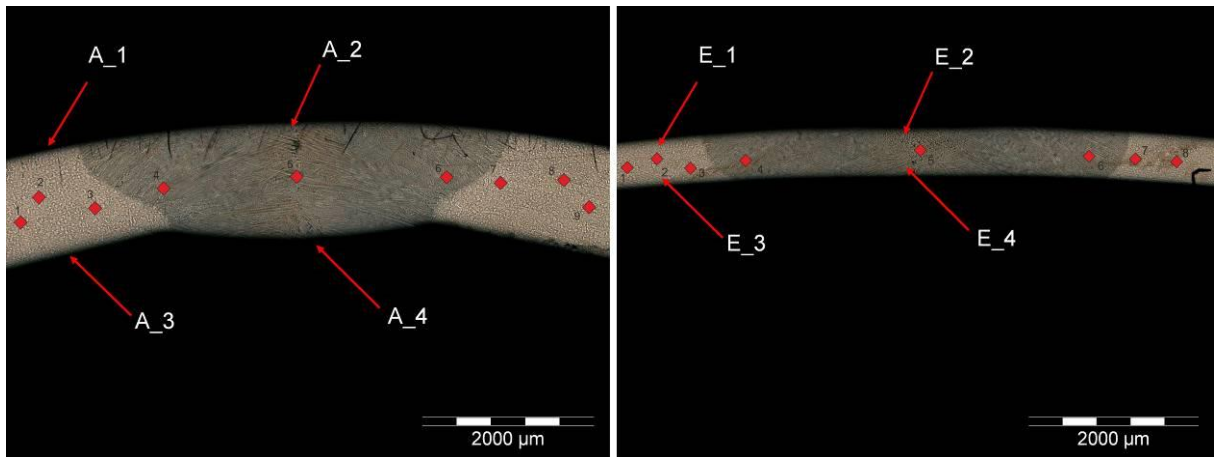


Fig. 45: Microsection of the basic structure and the welding seam before (left) and after (right) deformation.

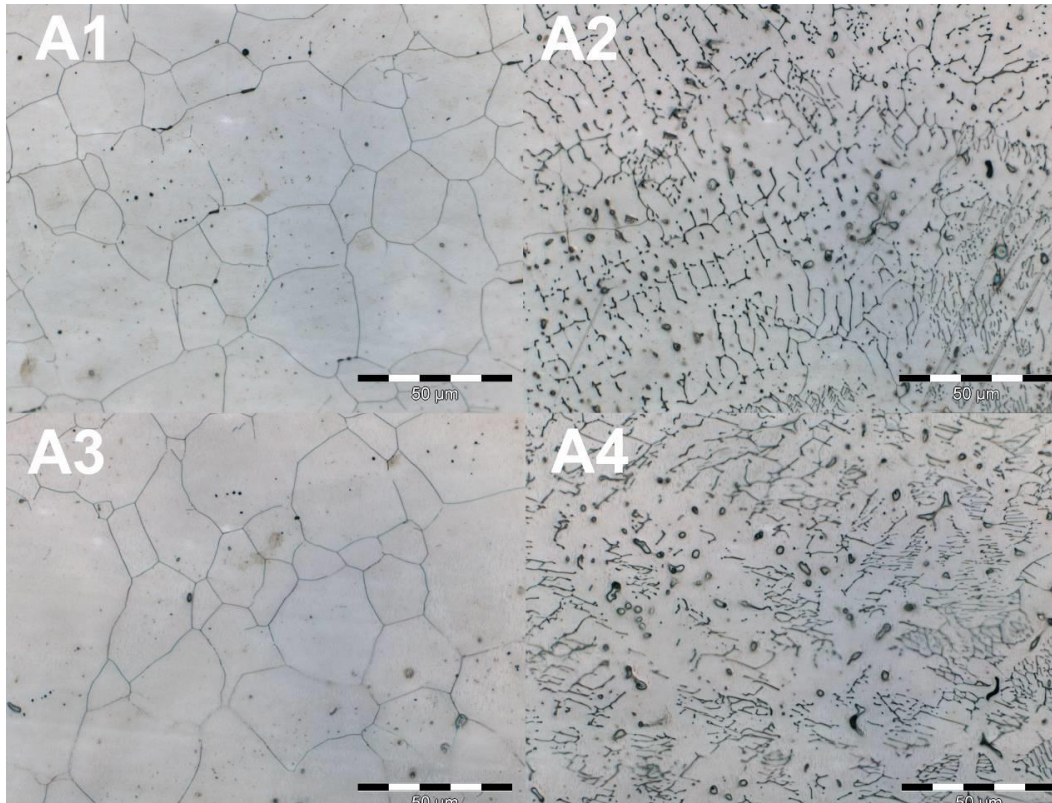


Fig. 46: Micrograph of the basic structure and the welding seam before deformation.

Fig. 47 illustrates the microstructure of the basic structure at the outside (E1) and the inside of the tube (E3) and the structure of the welding seam at the outside (E2) and at the inside of the tube (E4) after the deformation. It is observed, that the grain size at the outer diameter is between 20-60 $\mu\text{m}$  and at the inner diameter between 5-30 $\mu\text{m}$  after the deformation.

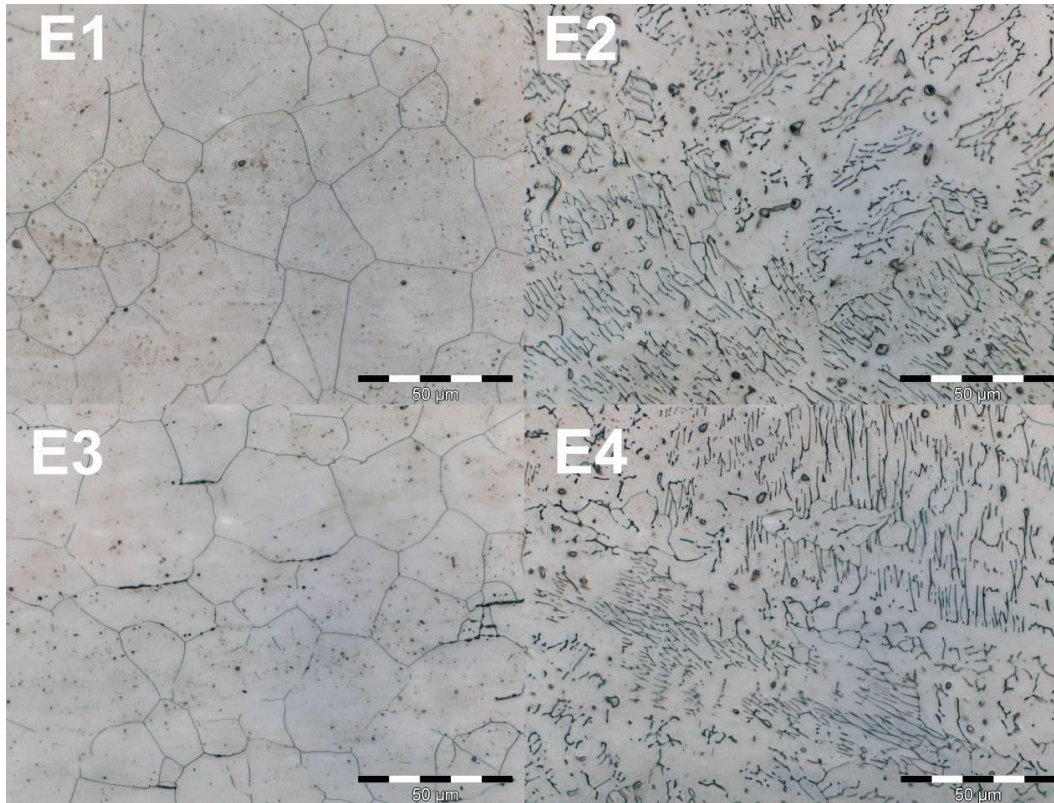


Fig. 47: Microsection of the basic structure and the welding seam after deformation.

The hardness profile of the passage near to the welding seam before the deformation shows no significant characteristic as Fig. 48 displayed. The hardness obtains an almost constant value of around  $210 \pm 10$  HV. The positions of the measuring points were pictured in Fig. 45.

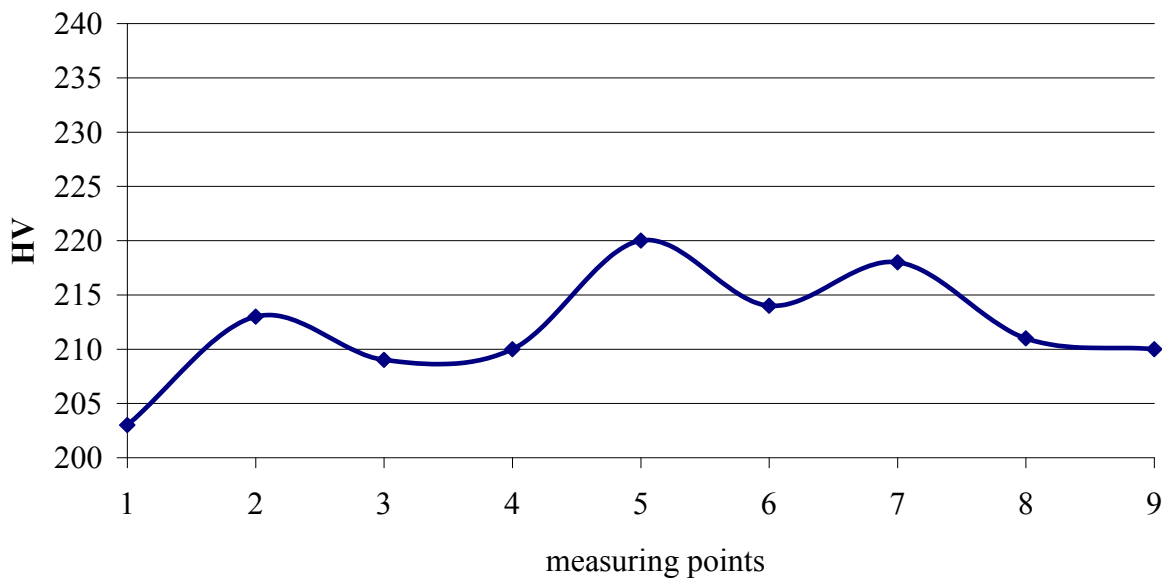


Fig. 48: Hardness profile of the basic structure.

The characteristics of the hardness after the deformation is shown in Fig. 49. In general, the hardness increased through the forming process, due to strain hardening. Nevertheless, the heat affected zone next to the welding seam (Points 3,4, and 6) has a significant lower level of hardness as the basic structure and the welding seam.

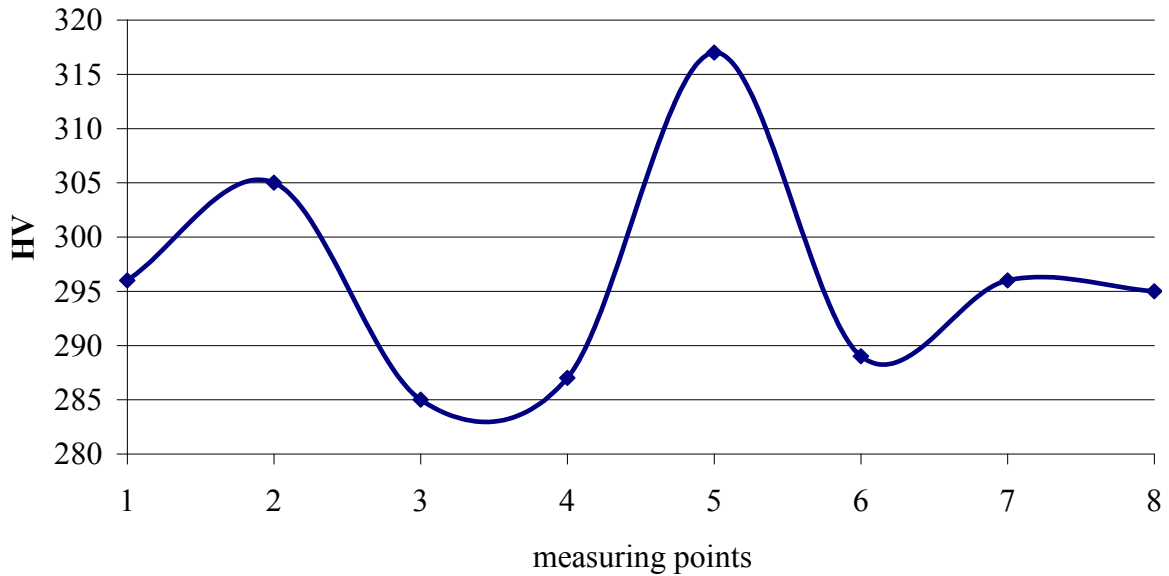


Fig. 49: Hardness profile after deformation.

## 7.1 Stress State of a Ball Spinning Expansion Process

The distribution of the effective plastic strain in Fig. 50 points out, that the highest deformations are at the inner side of the tube, as also the micrograph in Fig. 47 shows.

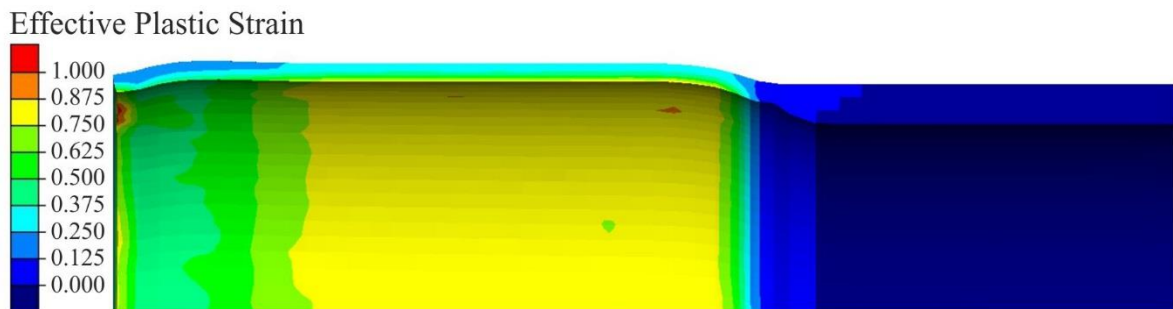


Fig. 50: Effective plastic strain of the FEM simulation in an axial section.

Fig. 51 shows the normal stress state during the forming process. The stress state and the deformation mechanism depend on the workpiece geometry. The upper bound of the

deformation process is the maximal tangential and axial strain of the workpiece. These stresses are accrued at the inner diameter of the expansion process.

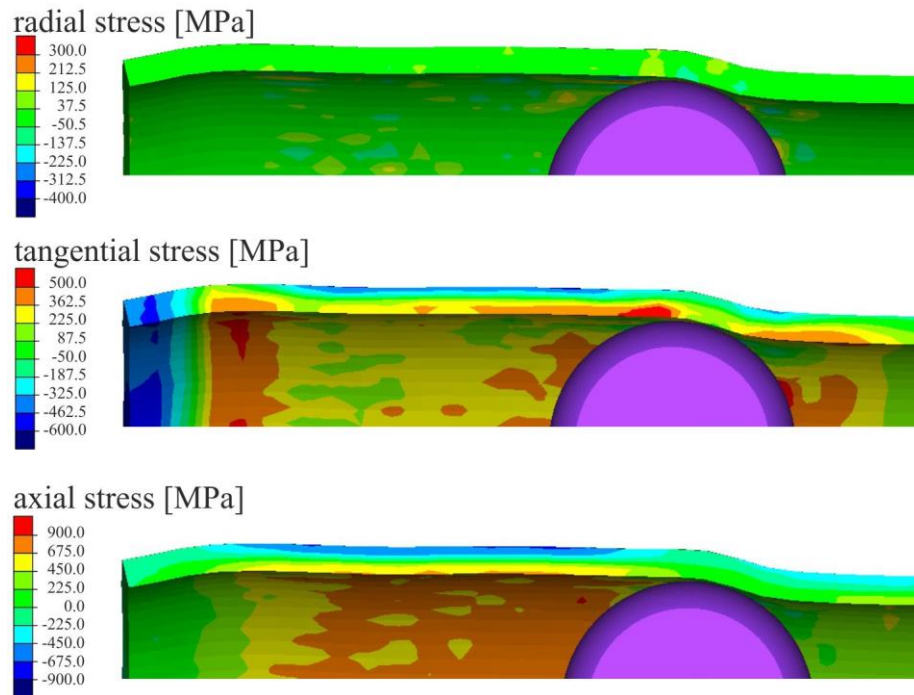


Fig. 51: Axial tube section showing the radial, tangential and axial stresses.

The essential shear stresses for the forming process are pictured in a tangential and an axial section in Fig. 52. The middle part of the tube thickness undergoes positive and negative shear stresses in axial direction during the expansion of the tube.

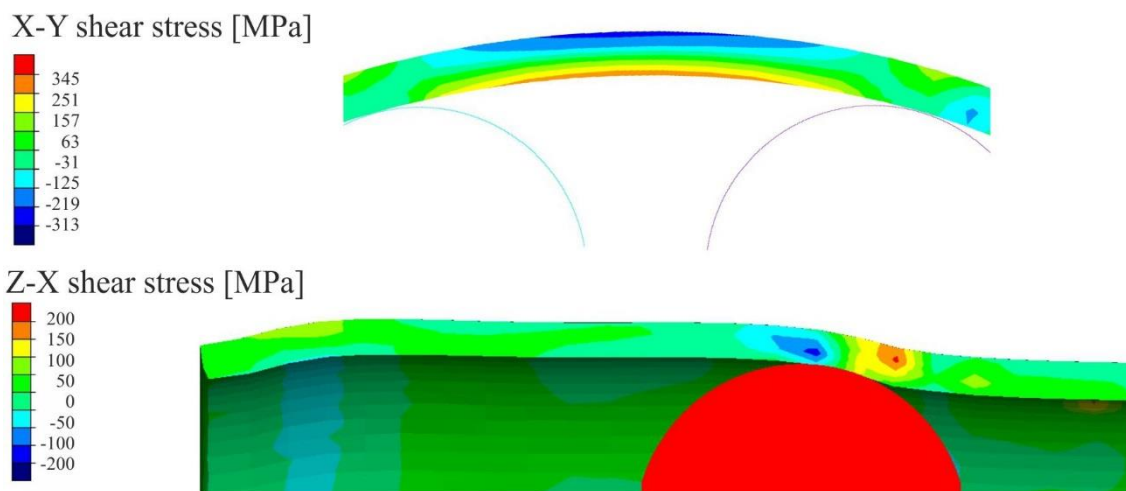


Fig. 52: Axial- and tangential tube section showing the shear stresses.

## 7.2 Sensitivity Study on the Effects of Process Parameters on the Forming Forces

As already mentioned, there are many different process parameters. Some of these parameters can be modified while still maintaining the final geometry. The analytical description in Eq.2 to Eq.17 allows assessing the change of the forming forces, when selected parameters are varied. Fig. 53 describes the variation of the diameter of the ball ( $D_k$ ), axial feed rate ( $v$ ), radial reaming ( $x_r$ ), efficiency of plastic deformation ( $\eta$ ) and flow stress ( $k_f$ ). During the sensitivity study, the other parameters were kept constant at the values printed in Table 1.

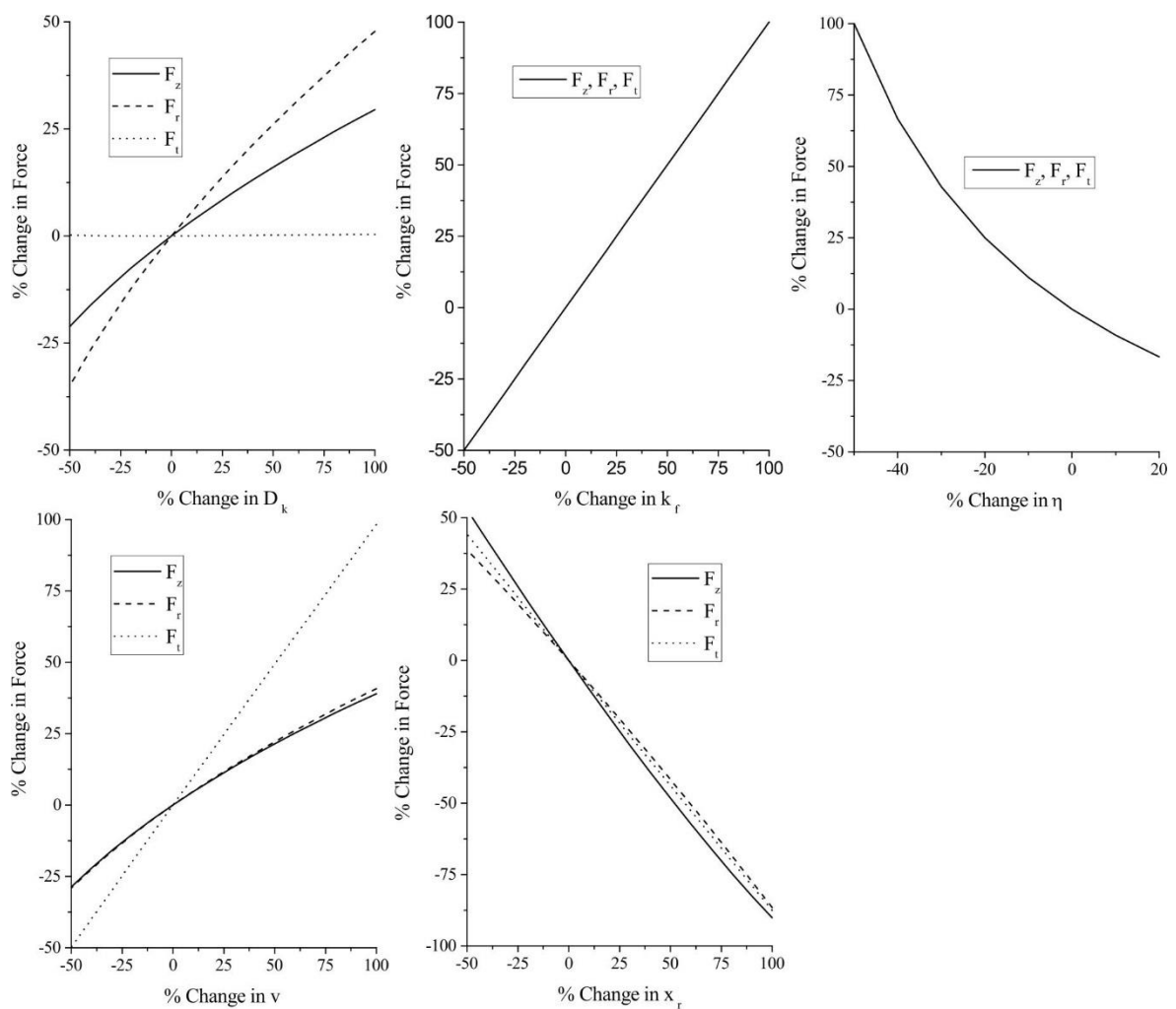


Fig. 53: Sensitivity study on the effects of process parameters on the forming forces.

The sensitivity of the drive torque regarding friction is shown in Fig. 54. The lines “coulomb” and “shear frictional stress” point out the analytically calculated influence on the drive torque. In order to calculate the influence of the coulomb friction in  $P_C$ , the coefficient of the shear frictional stress at the area  $A_{dr}$  is set to zero (Fig. 37). Vice versa, the coulomb friction is set to zero while the influence on the shear frictional stress is calculated. In reality, the drive torque is composed of both values with different friction coefficients. In the analytical calculation, the shear frictional stress model is used for the contact between the tube and ball. Moreover, the coulomb friction model is used for the contact between ball and leading ring. The simulation was carried out by using the coulomb friction for both contact points of the ball.

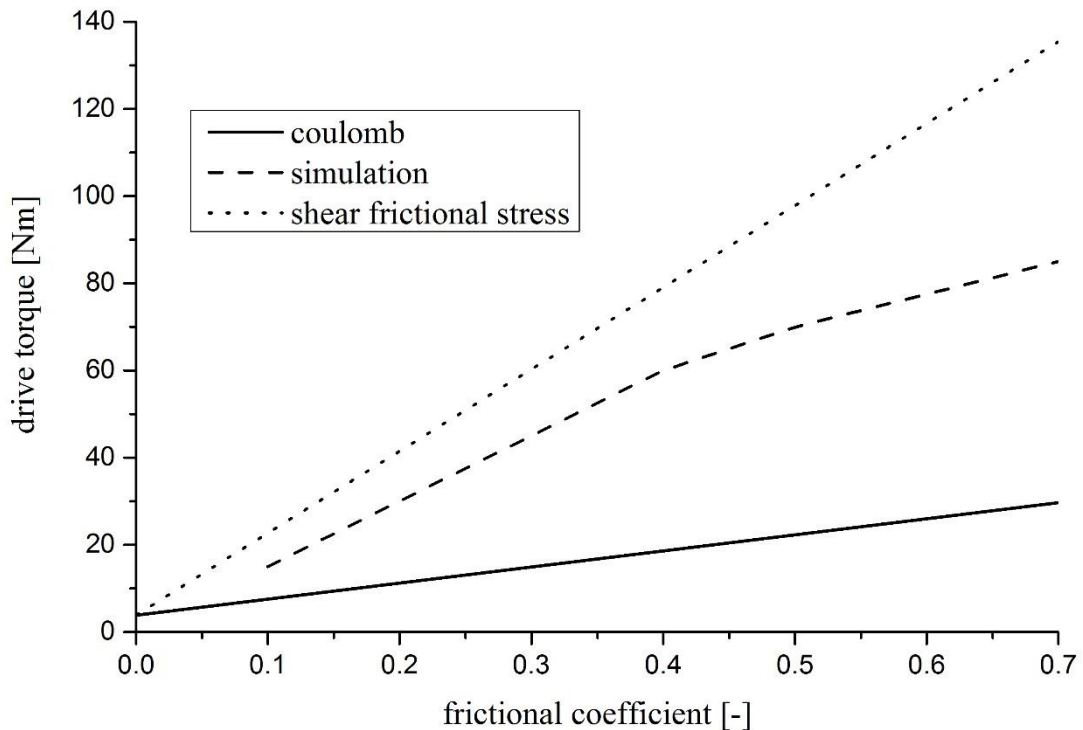


Fig. 54: Sensitivity of the frictional coefficient on the drive torque.

## 8. Damage Minimised Ball Spinning Process Design

The deformability by ball spinning is limited by surface cracking. A closer look pointed out the dependence of some process parameters. The most influencing parameters are the workpiece diameter ratio  $D_1/D_2$ , the tool diameter ratio  $D_1/d$  and the axial feed rate  $v$ . A vast number of experiments would be necessary to solve all the interactions between these parameters. A 3D FEM simulation also has its limitations in the computing time. This chapter proposes a 2D FEM model to predict the damage during a ball spinning reduction process and gives a detailed view of a statistical design of experiments. Parts of these chapter have been published by the author in Kuss et. al. 2016.

### 8.1 2D FEM Simulation of Damage Behavior

The FEM simulation is performed to depict the damage behaviour of the ball spinning reduction process. Fig. 55 shows the assembly of the FEM simulation in Abaqus 6.12.

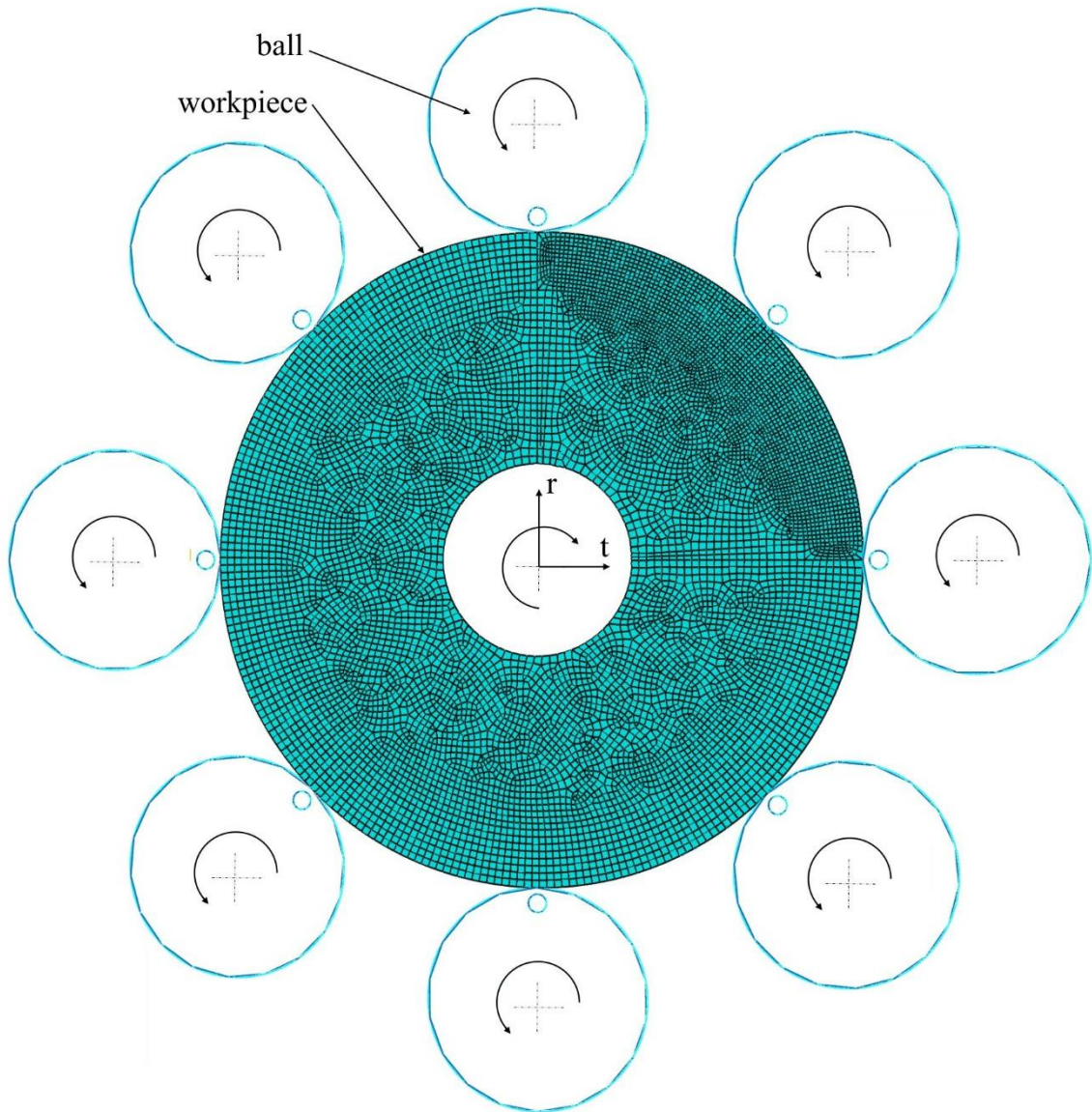


Fig. 55: Set up of the ball spinning damage FEM model to predict damage.

Generally, the process is performed as an isotropic elasto plastic simulation. The Young's Modulus of 210 GPa and a Poisson's Ratio of 0.3 are used and the values of the fictitious flow curve are listed in Table 4. It can be assumed, that the gradient of the strain hardening curve and the strain rate has only an influence on the bulge levels in front of the deformation zone and therefore only on the damage level, but not on the variation of the damage. A coulomb friction coefficient of 0.5 is used for the tangential behaviour and a "hard contact" respective to the classical Lagrange multiplier method of constraint enforcement is performed for the normal behaviour. Preliminary investigation showed, that the friction coefficient provides no significant influence on the FEM simulation. For the implementation of the kinematic behaviour, the rod is modelled as a thick-walled tube. The FEM model is created as a 2D simulation with generalized plane strain elements (Dassault Systemes). The mesh is separated

into a quart with fine elements with a length of 0.12 mm. The residual elements are modelled with an element lengths of 0.20 mm. The balls spin around their own centre point and simultaneously the workpiece turns around the centre of the rod.

Table 4: Fictitious values of the flow curve.

plastic strain [ - ]	yield stress [ MPa ]
0	650
0.13	900
5	900

The damage factor (Eq.32) of Ayada et. al. (1987) is employed with a “User-Routine” into the simulation to estimate the damage behaviour of the ball spinning process. Ayada et. al. include the medial stress  $\sigma_m$  divided by the equivalent stress  $\sigma_v$ , which takes into account the triaxiality of the stress state into account and is consequently suitable for the ball spinning process.

$$D = \int_0^\varphi \frac{\sigma_m}{\sigma_v} \cdot d\varphi \quad (32)$$

Every partition of the workpiece in this process undergoes a few contact situations with balls as displayed schematically in Fig. 56. The number of contacts and the geometrical conditions are influenced by the process parameters.

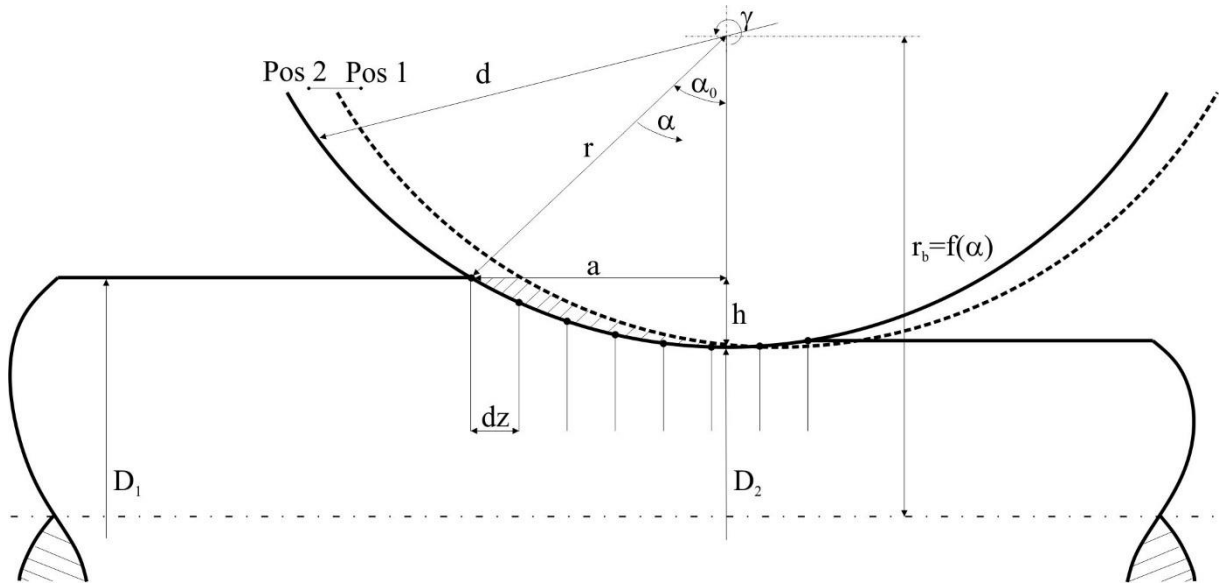


Fig. 56: Schematic illustration of the contacts during ball spinning.

The first step is the calculation of the simulated length and time. The parameters  $h$  and  $a$  are calculated by the initial workpiece diameter  $D_1$  [mm], the final workpiece diameter  $D_2$  [mm] and the ball radius  $r$  [mm].

$$h = \frac{D_1 - D_2}{2} \quad (33)$$

$$a = \sqrt{r^2 - (r - h)^2} \quad (34)$$

The incremental distance  $dz$  is the feed rate  $v$  [mm/rev] divided by the number of balls  $n$  [-].

$$dz = \frac{v}{n} \quad (35)$$

The parameter  $a$  is doubled to ensure that the elastic relaxation has enough time in the simulation. This is especially important for small diameter changes.

$$z = 2 \cdot a \quad (36)$$

The number of contacts  $n_c$  is the integral multiple of  $z$  divided by  $dz$ .

$$k = \frac{z}{dz} \quad (37)$$

$$n_c := \max \{k \in \mathbb{Z} | k \leq n_c\} \quad (38)$$

Therefore, the simulated distance is calculated by the number of contacts  $n_c$  and  $dz$ .

$$z_{ges} = n_c \cdot dz \quad (39)$$

The simulated time  $t_{ges}$  is the distance  $z_{ges}$  divided by the rotational speed  $U$  [rev/min] times the feed rate  $v$ .

$$t_{ges} = \frac{z_{ges}}{\frac{U}{60} \cdot v} \quad (40)$$

The angle of the first contact point  $\alpha_0$  is calculated by the parameters  $a$  and  $h$ .

$$\alpha_0 = \arccos\left(\frac{a}{r}\right) \quad (41)$$

With all these parameters the radial position of the balls  $r_b$  are calculated by  $\alpha_0$ ,  $D_2$  and  $r$ . The function of the rotation of the balls around their own centre  $\gamma$  are calculated by the parameters  $r_b$ ,  $r$  and  $\alpha$ .

$$r_b = \frac{D_2}{2} + r \cdot (2 - \cos(\alpha_0 - \alpha)) \quad (42)$$

$$\gamma = \frac{\alpha}{(r_b - r)} \cdot r \quad (43)$$

This calculation defines the kinematic of the ball spinning process in the simulation. The workpiece turns around its centre with the rotation speed  $U$ . During the time  $t_{ges}$ , the balls move radially inward following function  $r_b$  and rotate around their own centre defined by function  $\gamma$ .

## 8.2 Statistical Design of Experiments

To reduce the number of simulations, a statistical design of simulations is implemented. In this investigation a central composite experimental design is implemented. Thereby a specific modification of the process parameters ensures the same quality of the output by a low number of simulations. Fig. 57 shows a scheme of the central composite experimental design for  $k = 3$  factors. Thereby, the central composite experimental design uses 15 instead of 28 ( $3^k$ ) experiments (Kleppmann 2008).

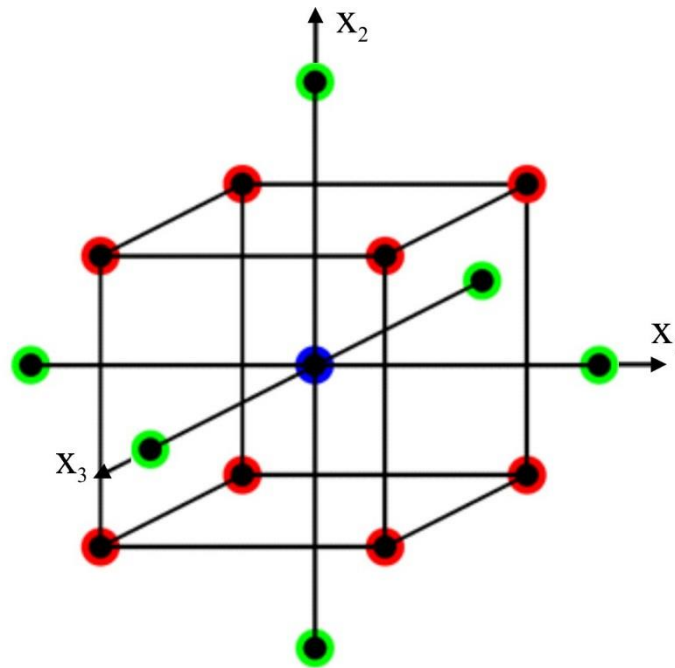


Fig. 57: Schematic illustration of the central composite experimental design.

Every point in the illustration represents one experiment (Scheffler 1997). The number of experiments  $N_{Ges}$  is the sum of cube experiments ( $N_w$ , red), the star experiments ( $N_{St}$ , green), the centre experiment ( $N_0$ , blue) and the factor levels  $k$ .

$$N_{Ges} = N_w + N_{St} + N_0 = 2^k + 2k + 1 = 2^3 + 2 \cdot 3 + 1 = 15 \quad (44)$$

The range of the star  $\lambda$  is calculated using Eq.45 and Eq.46.

$$\lambda^2 = \frac{1}{2} \cdot (\sqrt{N_{Ges} \cdot N_w} - N_w) \quad (45)$$

$$\lambda = \sqrt{\frac{1}{2} \cdot (\sqrt{15 \cdot 8} - 8)} = 1.215 \quad (46)$$

Table 5 lists the parameter combination for three factors.  $x_1$  represents the feed rate  $v$  [mm/rev],  $x_2$  the tool diameter ratio  $D_1/d$  and  $x_3$  the workpiece diameter ratio  $D_1/D_2$ . The parameter combinations are the standardized values  $\pm\lambda$ ,  $\pm 1$  and 0. The real value of each parameter is normalized to  $\lambda$  by the Eq.47 to Eq.49.

$$x_1 = \frac{2.5 \cdot (v - 1)}{1} \quad (47)$$

$$x_2 = \frac{4 \cdot \left( \left( \frac{D_1}{d} \right) + 2.340989171204 \right)}{2.340989171204} \quad (48)$$

$$x_3 = \frac{-273.375 \cdot \left( \left( \frac{D_1}{D_2} \right) - 1.007427307206 \right)}{1.007427307206} \quad (49)$$

Table 5: Parameter combination for the central composite experimental design.

real values			normalized values [ - ]		
v [mm/rev]	$D_1/d$ [-]	$D_1/D_2$ [-]	$x_1$	$x_2$	$x_3$
0.6	2.9262	1.0111	-1	-1	-1
1.4	2.9262	1.0111	1	-1	-1
0.6	1.7557	1.0111	-1	1	-1
1.4	1.7557	1.0111	1	1	-1
0.6	2.9262	1.0037	-1	-1	1
1.4	2.9262	1.0037	1	-1	1
0.6	1.7557	1.0037	-1	1	1
1.4	1.7557	1.0037	1	1	1
0.514	2.3410	1.0074	-1.215	0	0
1.486	2.3410	1.0074	1.215	0	0
1	3.0521	1.0074	0	-1.215	0
1	1.6299	1.0074	0	1.215	0
1	2.3410	1.0119	0	0	-1.215
1	2.3410	1.0029	0	0	1.215
1	2.3410	1.0074	0	0	0

Within this parameter field, two experiments are carried out and the parameter values are listed in Table 6.

Table 6: Parameter of real experiments.

$D_1$ [mm]	$D_2$ [mm]	v [mm/rev]	d [mm]	$D_1/d$ [-]	$D_1/D_2$ [-]
17.0	16.8	1	7.89	2.1546	1.0119
16.9	16.8	1	7.89	2.1420	1.0059

After processing the simulation field, all results are taken from the fine meshed region with the highest damage and listed in Table 7.

Table 7: Results of the central composite experimental design.

normalized values [ - ]			Ayada [ - ]
$x_1$	$x_2$	$x_3$	$y$
-1	-1	-1	12.2757
1	-1	-1	5.6172
-1	1	-1	9.6436
1	1	-1	4.4188
-1	-1	1	0.4741
1	-1	1	0.3305
-1	1	1	0.3515
1	1	1	0.2513
-1.215	0	0	8.3019
1.215	0	0	3.0451
0	-1.215	0	5.3921
0	1.215	0	3.6488
0	0	-1.215	7.3922
0	0	1.215	0.1195
0	0	0	4.3913

With the results  $y$  of the simulations, a regression polynomial can be calculated (Scheffler 1997).

$$\hat{y} = b_0 + \sum_{i=1}^k b_i x_i + \sum_{i < j}^{k-1} \sum_{j=1}^k b_{ij} x_i x_j + \sum_{i=1}^k b_{ii} x_i^2 \quad (50)$$

The parameter  $b_i$  is the linear and  $b_{ii}$  the quadratic influence on the parameter  $x_i$  and  $x_j$ .  $b_{ij}$  describes the interaction of  $x_i$  to  $x_j$ .  $b_0$  represented the Y distance at point 0. Using Eq.51 to Eq.55 the coefficients of the regression polynomial (Eq.56) are calculated.

$$\bar{y} = \frac{1}{N_{Ges}} \cdot \sum_1^{N_{Ges}} y \quad (51)$$

$$b_i = \frac{1}{\sum_1^{N_{Ges}} x_i^2} \cdot \sum_1^{N_{Ges}} x_i y \quad (52)$$

$$b_{ij} = \frac{1}{\sum_1^{N_{Ges}} (x_i x_j)^2} \cdot \sum_1^{N_{Ges}} x_i x_j y \quad (53)$$

$$b_{ii} = \frac{1}{\left[ \sum_1^{N_{Ges}} \left[ x_i^2 - \frac{\sum_1^{N_{Ges}} x_i^2}{N_{Ges}} \right]^2 \right)} \cdot \sum_1^{N_{Ges}} \left[ x_i^2 - \frac{\sum_1^{N_{Ges}} x_i^2}{N_{Ges}} \right] \cdot y \quad (54)$$

$$b_0 = \bar{y} - \sum_1^k \frac{\sum_1^{N_{Ges}} x_i^2}{N_{Ges}} b_{ii} \quad (55)$$

$$\hat{y} = b_0 + b_1 x_1 + b_2 x_2 + b_3 x_3 + b_{12} x_1 x_2 + b_{13} x_1 x_3 + b_{23} x_2 x_3 + b_{11} x_1^2 + b_{22} x_2^2 + b_{33} x_3^2 \quad (56)$$

Table 8 shows the calculated coefficients after simulated experimental design. The workpiece diameter ratio  $D_1/D_2$  produces a significant linear influence and a strong relation on the tool diameter ratio  $D_1/d$ .

Table 8: Coefficients for the normalized values of the regression polynomial.

coefficients for normalized values	
b0	4.80
b1	-1.69
b2	-0.56
b3	-3.60
b12	0.18
b13	0.45
b23	1.45
b11	0.50
b22	-0.28
b33	-0.80

The coefficients for the regression polynomial are transformed back using Eq.47 to Eq.49 and the result for a constant feed rate is pictured in Fig. 58. The damage is increasing with higher initial workpiece diameter and smaller ball diameter. The two experiments from Table 6,  $D_1=17\text{mm}$  and  $D_1=16.9\text{mm}$  are displayed.

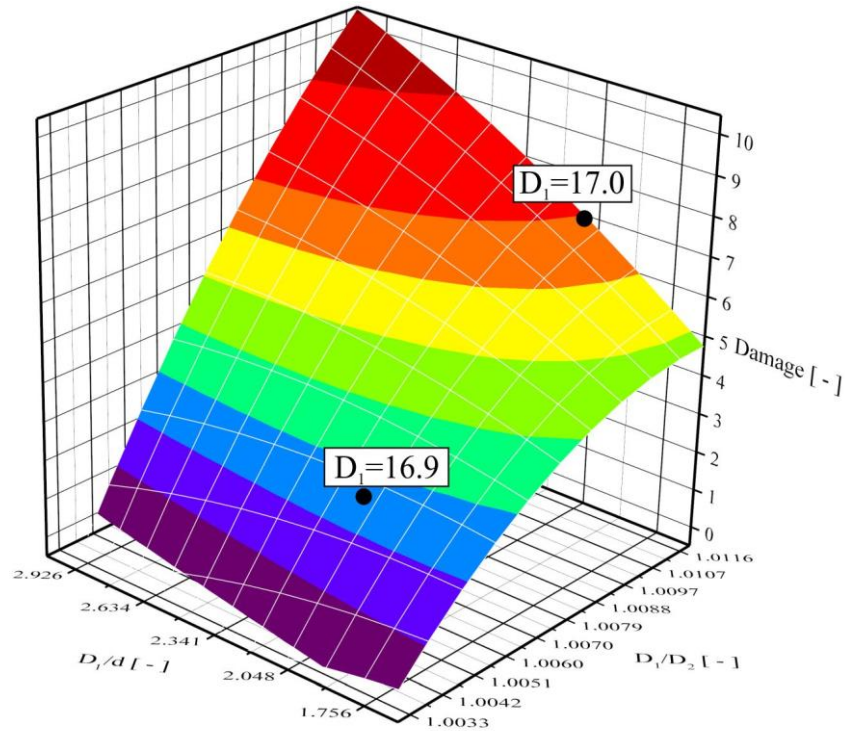


Fig. 58: Regression of the damage in dependence on the tool diameter ratio  $D_1/d$  and the workpiece diameter ratio  $D_1/D_2$ , by a constant feed rate  $v$  of 1 mm/rev.

Fig. 59 displays the influence on the damage by a constant tool diameter ratio  $D_1/d$  of 2.13. It is remarkable that an increase of the feed rate results in a reduction of the damage. Similar to the Fig.8, the damage is reduced by decreasing the workpiece diameter.

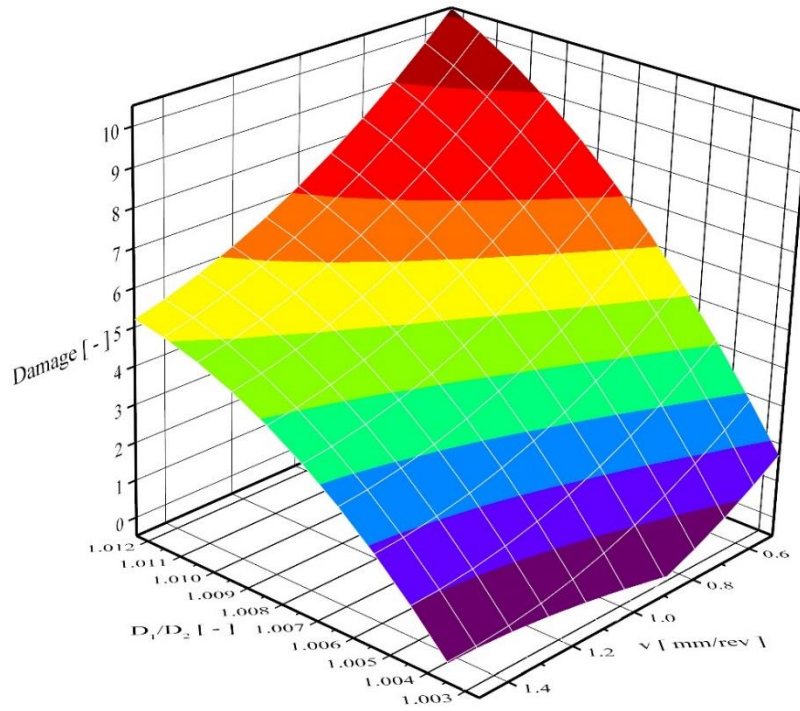


Fig. 59: Regression of the damage in dependence on the workpiece diameter ratio  $D_1/D_2$  and the feed rate  $v$ , by constant feed rate  $v$  of 1 mm/rev.

Fig. 60 depicts the influence on the damage of the feed rate and the tool diameter ratio by a constant workpiece diameter ratio  $D_1/D_2$  of 1.0119. The ball diameter and the axial feed rate have to be at maximum to minimise the Ayada damage.

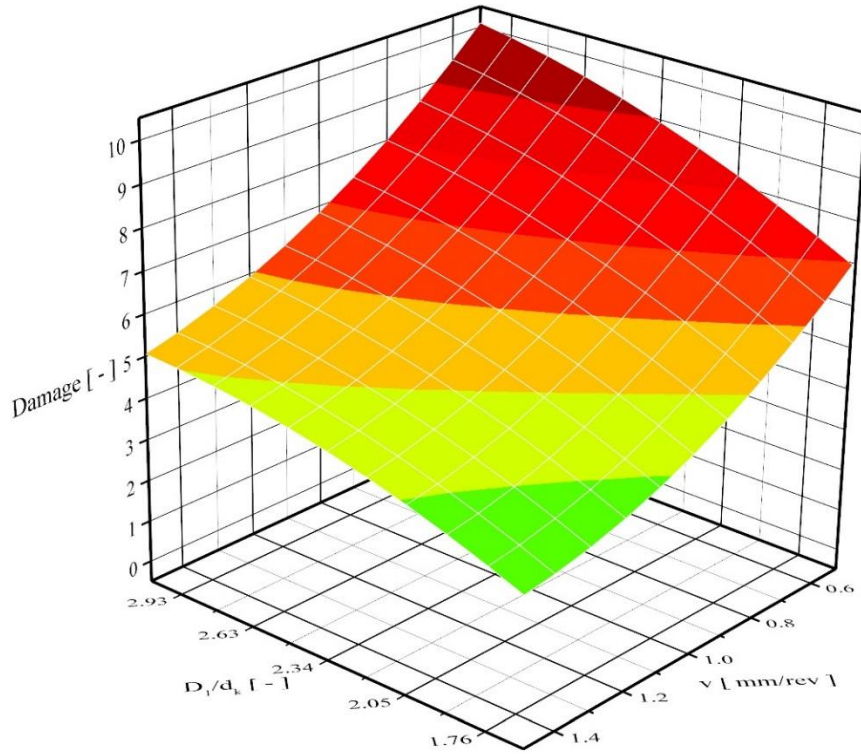


Fig. 60: Regression of the damage in dependence on the feed rate  $v$  and the tool diameter ratio  $D_1/d$ , by a constant workpiece diameter ratio  $D_1/D_2$  of 1.0119 [-].

The applicability of the Ayada model is shown in Fig. 61 and the results of two experiments are depicted. The two experiments are taken from the data field within, where Fig. 61 a) accords to  $x_1 = 1$ ,  $x_2 = 1$ ,  $x_3 = -1$  and Fig. 61 b) accords to  $x_1 = -1$ ,  $x_2 = -1$ ,  $x_3 = -1$ . The small ball diameter and the low feed rate of the experiment b) result in a high Ayada damage. The experiment a) has a lower roller angle  $\alpha$  and steamrolls the workpiece with a higher feed rate as the experiment b). Following, the Ayada damage in experiment a) is about three times smaller than for experiment b).

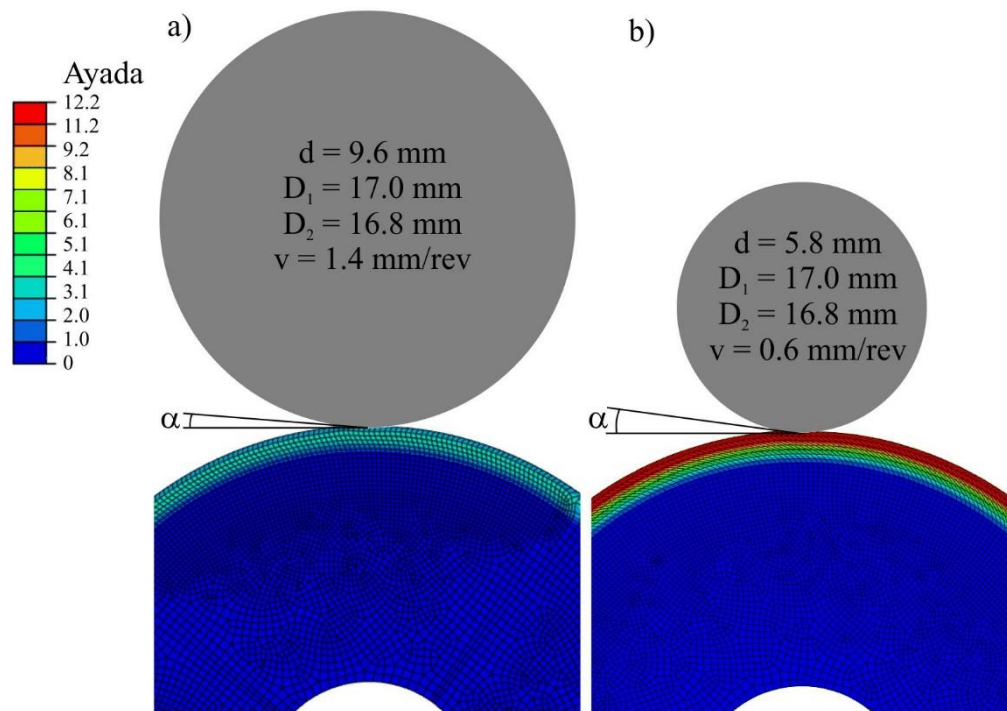


Fig. 61: Damage value of Ayada of two different experiments.

Fig. 62 pictures the highest damage values of the two experiments according to Ayada. It is shown, that the highest values are located below the top of the surface at the third row of nodes in the simulation.

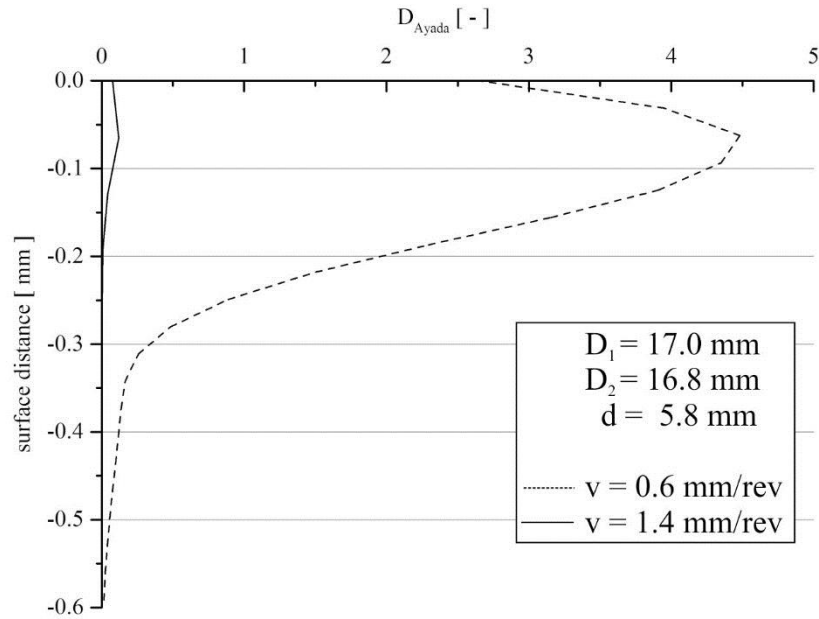


Fig. 62: Damage value according to Ayada plotted over the distance to the surface.

### 8.3 Experimental Details for a Ball Spinning Reduction Process

In the experiments, a rod ( $D_1$  and a length of 120 mm) made of 37MnSi5 was used as workpiece. The tool was made of a ball bearing SKF 7301B.JP with 8 balls (Fig. 63).

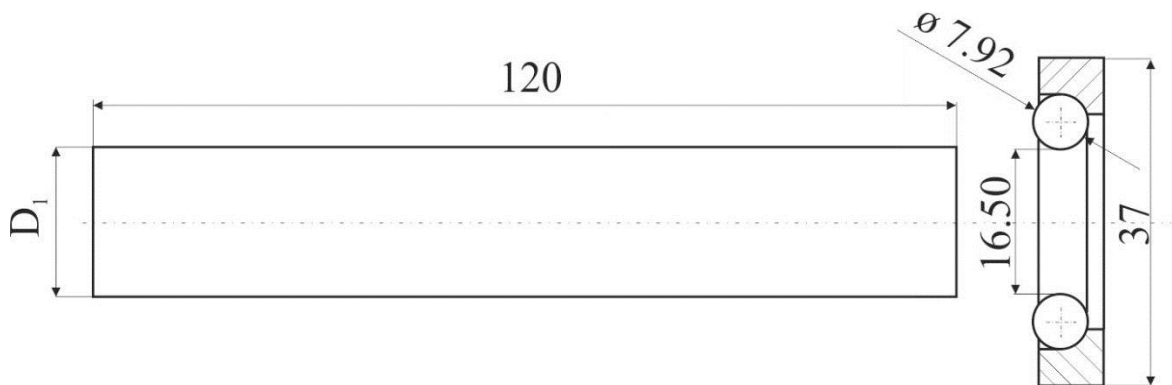


Fig. 63: Workpiece and tool geometry for a ball spinning reduction process.

During the experiments, the process parameters of Table 6 were used. The balls and the cage are turned by the tool support. The workpiece is tangentially fixed and axially moved by the workpiece support. A hydraulic cylinder does the axial movement and during the deformation,

the process is oiled to reduce the forming forces and to forestalled surface wear between tool and workpiece.

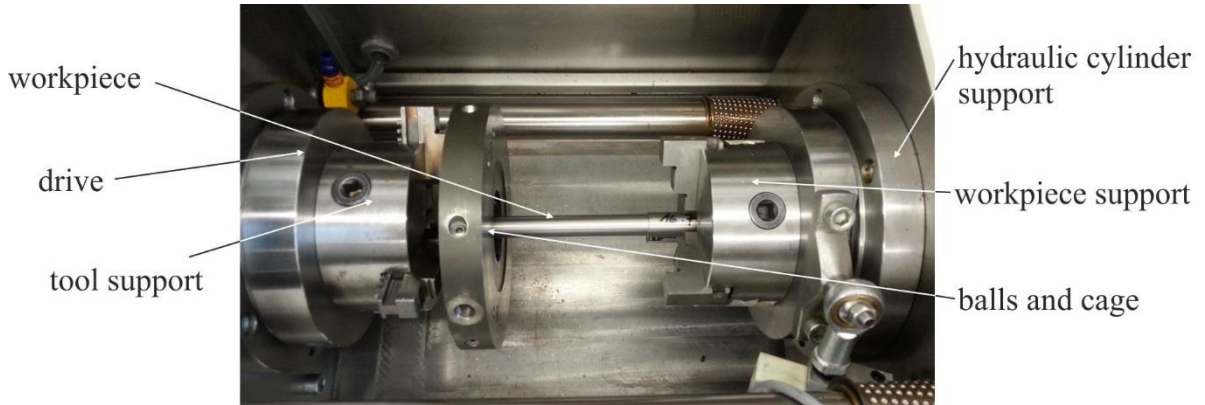


Fig. 64: Experimental reduction setup of the friction welding machine.

Fig. 65 depicts the damage occurring at the workpieces during the ball spinning experiment by changing the workpiece diameter ratio  $D_1/D_2$ . Differences in roughness are optically visible.



Fig. 65: Sample  $D_1 = 17.0$  mm &  $D_1 = 16.9$  mm after ball spinning.

The intensifying roughness in axial direction of the sample  $D_1 = 17.0$  mm can be referred to the growing axial bulge. Bulges appear axially and tangentially in front of the balls. The balls overrun the bulge when the bulge becomes too big and a metal ring occurs at the workpiece

(Fig. 65). This is also the reason, why this experiment was stopped earlier and the axial deformation is shorter.

Table 9: Roughness value of the two experiments after ball spinning.

	$D_1$ [mm]	$R_a$ [ $\mu\text{m}$ ]	$R_q$ [ $\mu\text{m}$ ]	$R_z$ [ $\mu\text{m}$ ]
R1	17.0	8.65	10.95	61.61
R2	16.9	4.34	5.49	28.32

As seen in Fig. 65 also the roughness value of the two samples (Table 8) are different. The roughness of R1 is a lot higher, than for R2. Since R1 was the sample, where bulges appeared, it can be concluded, that roughness can be an indication of damage.

## 9. Internal Stress State after Ball Spinning

The internal stress state of products after the forming process has become an increasing focus, since it is especially important for the prediction of lifetime under fatigue conditions. Therefore, a profound knowledge of the material properties and process understanding is required. The effects on kinematic and isotropic hardening of high strains has a significant influence on forming processes with reversing strain hardening like ball spinning. This chapter gives a detailed view on the deformation mechanism of a ball spinning expansion process using the finite element method. A closer look is taken on the differences between kinematic and isotropic hardening with regards to the internal stress state after the forming process. This investigation provides a method to calibrate the parameter combination of isotropic and kinematic strain hardening on the final geometry and demonstrates this experimentally.

### 9.1 Hardening Models

Lemaitre and Chaboche (2002) explain six different particular flow laws and define the terms isotropy, kinematic and anisotropy. These words are used for the flow criteria and for the hardening, which means for the evolution of the criterion. Isotropic and anisotropic describe both aspects, while the term kinematic is applied only to the idea of evolution. The six levels of theory are restricted to the use of the second invariant and are listed in Table 10.

Table 10: Different plasticity criteria and flow rules (Lemaitre and Chaboche 2002).

case	initial criterion	hardening variables	transformed criterion due to hardening	
1	$f(J(\sigma))$ isotropic	$p$	$f(J(\sigma)) - R(p)$	isotropic
2	$f(J(\sigma))$ isotropic	$X$	$f(J(\sigma - X))$	kinematic
3	$f(C:\sigma':\sigma')$ anisotropic	$p$	$f(C:\sigma':\sigma') - R(p)$	isotropic
4	$f(C:\sigma':\sigma')$ anisotropic	$X$	$f(C:(\sigma' - X):(\sigma' - X))$	kinematic
5	$f(J(\sigma))$ isotropic	$p, X, \varepsilon^p$	$f(J(\sigma - X)) - R(p)$	isotropic + kinematic + anisotropic
6	$f(C:\sigma':\sigma')$ anisotropic	$p, X, \varepsilon^p$	$f(C*:(\sigma' - X):(\sigma' - X)) - R(p)$	anisotropic + kinematic + anisotropic

- (1) Isotropic criterion – isotropic hardening: the invariant  $J(\sigma)$  and a scalar variable  $p$  are sufficient ( $J$  is, for example, the second invariant,  $J=J_2$ )
- (2) Isotropic criterion – kinematic hardening: the translation of the criterion by a tensor  $X$  is used.
- (3) Anisotropic criterion – isotropic hardening: the criterion is expressed in a more complex form, for example with  $(C:\sigma'):\sigma'$  where  $C$  depends on the material. However, this form of the criterion is retained during the hardening process by simple dilatation, and therefore, involves only a scalar variable  $p$ .
- (4) Anisotropic criterion – kinematic hardening: the form of the criterion is retained during hardening but the surface is subjected to a translation represented by the tensor  $X$ .
- (5) Isotropic criterion – anisotropic hardening (nonkinematic): the invariant  $J_2(\sigma)$  is transformed into a more complex expression, eventually leading to a kinematic effect in which  $C^*(\varepsilon^p)$  expresses an anisotropy depending on the present state of plastic strain.
- (6) Anisotropic criterion – anisotropic hardening. This is the generalization of case (5);  $C$  describes the initial anisotropy in a state of zero plastic strain.

(Lemaitre and Chaboche 2002)

Two material models are taken out of these description to exhibit the different influences on the deformation mechanism between isotropic (1) and kinematic (2) hardening. Both simulations are performed with a Young's Modul of 210000 MPa and a Poisson's Ratio of 0.3.

Von Mises (1931) characterized the isotropic hardening by the expansion of the Mises cylinder (Fig. 66). After reversing the strain hardening, the flow stress has the value of the strengthened Mises cylinder. A tabular flow curve as seen in Fig. 67 was used for the FEM simulation.

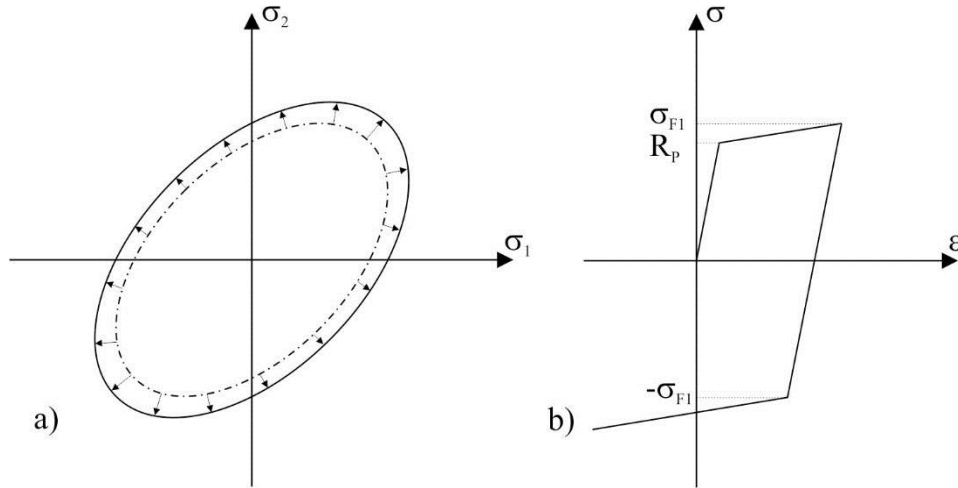


Fig. 66: Schematics of the isotropic hardening. a) Yield surface of the two dimensional stress state, b) the stress vs plastic strain response.

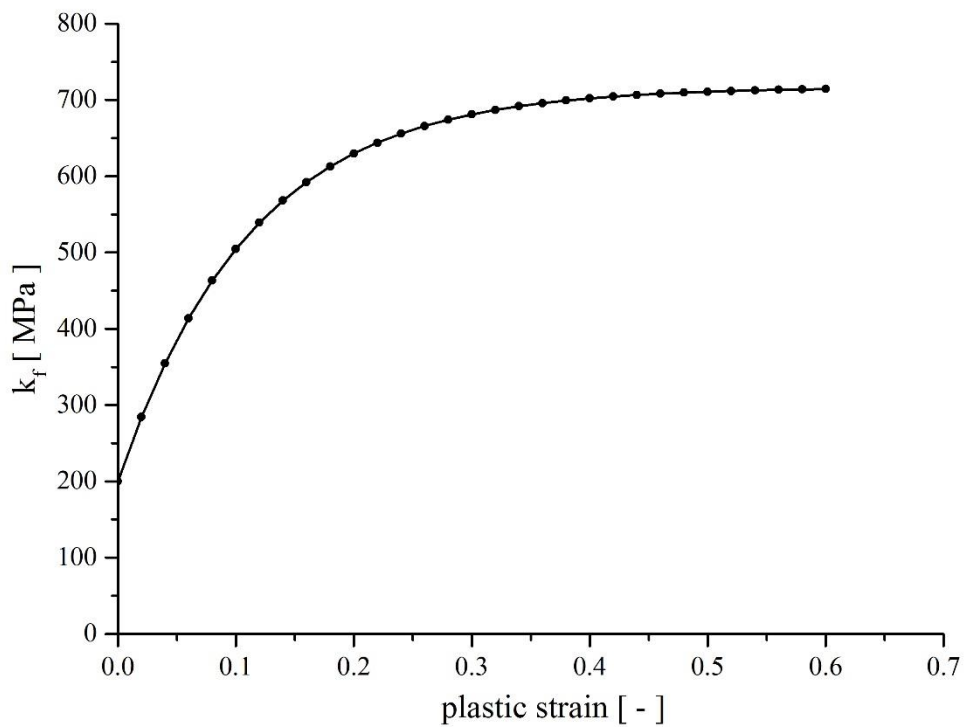


Fig. 67: Tabular flow curve of 1.4301 as used for the FEM simulation.

The kinematic hardening is characterized by the displacement of the Mises cylinder during strain hardening (Fig. 68). After reversing the strain hardening, the flow stress has the value of the displaced Mises cylinder. Therefore, the Chaboche-Modell (J.L. Chaboche 1989) was used for the FEM simulation. To maintain the same flow curve as for the isotropic model (Fig. 67), the minimum least squares method was used to calculate the kinematic Chaboche parameter (Eq.57) Yield Stress  $\sigma_0 = 200$  MPa, Kinematic Hardening Parameter  $C = 4600$  MPa and Gamma  $\gamma = 8.9$ .

$$\sigma = \sigma_0 + \frac{C}{\gamma} \cdot (1 - e^{(-\gamma \cdot \varepsilon_p)}) \quad (57)$$

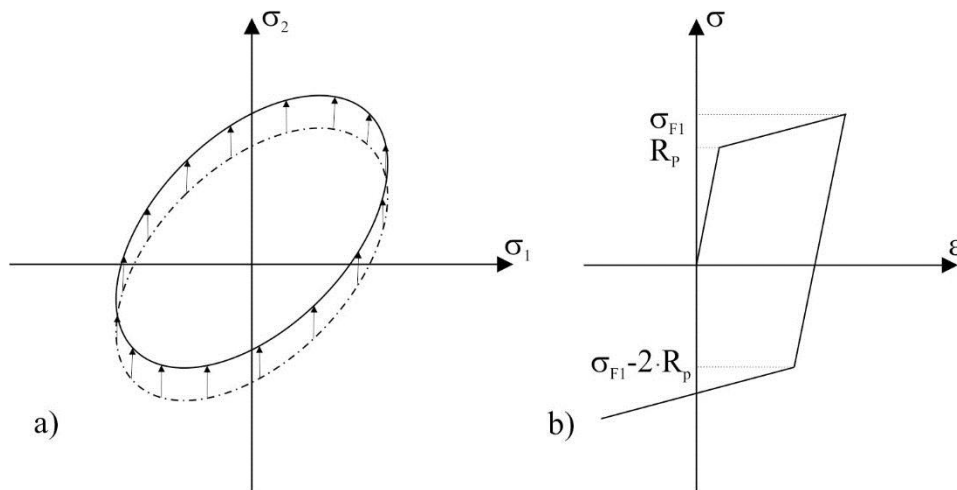


Fig. 68: Schematics of the linear kinematic hardening. a) yield surface of the two dimensional stress state, b) the stress vs plastic strain response.

## 9.1 Calibrating the Combination of the Strain Hardening Parameters

The simulation design is the same as in chapter 7.2 and the kinematic of the machine is the same as for the damage simulation with an axial speed of 1.5 mm/sec and a rotating speed of 150 rev/min. The model was processed for 10 sec. After simulating the deformation of the two extrema 100% kinematic- and 100% isotropic hardening with Abaqus 6.12, also a physical experiment was realized.

Due to the different hardening models also the internal stress state must be different between kinematic and isotropic hardening. The physical experiment needs to be a mixture of these two theories. To display the internal stress state, the models and the experiment are cut axially. Subsequently, half of the elements are deleted, the internal stresses relax and a reduction of the tube diameter arises. The same effect occurs at the physical workpiece. Fig. 69 (a) shows the tangential stress of the deformed tube, (b) shows the stress relaxation after the axial cut and (c) shows the physical tube segment.

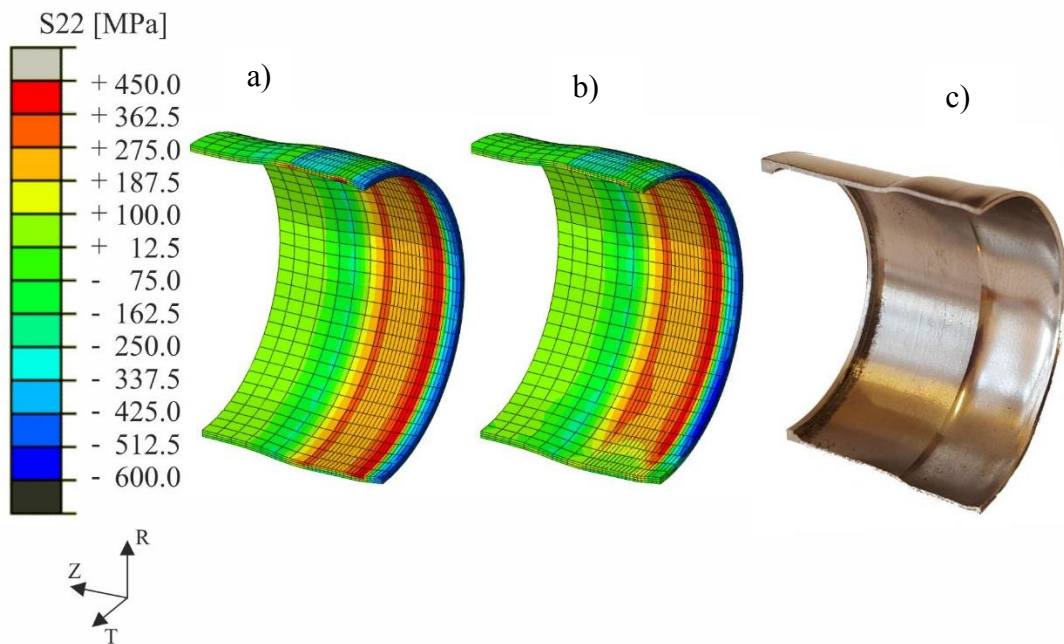


Fig. 69: Tangential stress of isotropic hardening at the in- and outside of the tube and the physical workpiece.

Due to the diverse internal stresses of the two strain hardening methods, the resulting diameters are also different. After processing the experiment, the tube was optically measured at the contour maximum of the profile with Alicona Infinite Focus G4 at the Chair for Metal Forming after deformation and after the axial cut. This experimental reduction of the diameter  $\Delta D_{ex}$  is between the simulated diameter reduction  $\Delta D_{iso}$  (isotropic) and  $\Delta D_{kin}$  (kinematic) as can be seen in Table 11. The grade of isotropic hardening is 91.63%, which is calculated by Eq.58.

Table 11: Diameter springsback after the axial cut.

	diameter [mm]		DD [mm]
	after deformation	after axial cut	
kin-hardening	36.8010	36.6169	0.1841
iso-hardening	36.9200	36.7622	0.1578
experiment	36.8300	36.6700	0.1600

$$h_{iso} = \frac{\Delta D_{kin} - \Delta D_{ex}}{\Delta D_{kin} - \Delta D_{iso}} \quad (58)$$

J.L. Chaboche (2008) describes the combination of the two hardening models in Eq.59 to Eq.63.

$$f = J(\underline{\underline{\sigma}} - \underline{\underline{X}}) - \sigma_F - R = 0 \quad (59)$$

$$J(\underline{\underline{\sigma}} - \underline{\underline{X}}) = \left( \frac{3}{2} (\underline{\underline{s}} - \underline{\underline{X}}) : (\underline{\underline{s}} - \underline{\underline{X}}) \right)^{1/2} \quad (60)$$

$$\dot{\underline{\underline{X}}} = \frac{2}{3} C \dot{\underline{\underline{\varepsilon}}}^p - \gamma \underline{\underline{X}} \dot{p} \quad (61)$$

$$X = v \frac{C}{\gamma} + \left( X_0 - v \frac{C}{\gamma} \right) \cdot e^{(-v\gamma \cdot (\varepsilon_p - \varepsilon_{p0}))} \quad (62)$$

$$\dot{R} = b(Q - R)\dot{p} \quad R = Q(1 - e^{-bp}) \quad (63)$$

$X$  is the back stress tensor,  $\sigma_F$  the initial size of the yield surface and  $R$  its evolution (increase or decrease the parameter).  $J$  denotes the Von Mises distance in the deviatoric stress space with the deviatoric stress tensor  $s$ .  $C$  and  $\gamma$  are the kinematic hardening coefficients,  $\varepsilon_p$  the plastic strain and  $p$  is the accumulated equivalent strain.  $Q$  and  $b$  are the isotropic hardening coefficients.

In this investigation a linear combination of the two models is used (Eq.64 to Eq.66). Therefore, only the coefficient  $Q$  and  $C/\gamma$  are transformed with the isotropic coefficient  $h_{iso}=0.9163$ . The sum of the combined flow curves is equivalent to the original flow curve used for the isotropic and kinematic hardening (Fig. 70). For a linear combination, the exponent  $b$  and  $\gamma$  are the equivalent with 8.9.

$$k_{f-iso0} = k_{f-kin0} = k_{f-iso1} \cdot h_{iso} + k_{f-kin1} \cdot h_{iso} \quad (64)$$

$$Q_0 \cdot (1 - e^{-b \cdot p}) = \frac{C_0}{\gamma} \cdot (1 - e^{-\gamma \cdot \varepsilon_p}) = Q_1 \cdot (h_{iso}) \cdot (1 - e^{-b \cdot p}) + \frac{C_1}{\gamma} \cdot (1 - h_{iso}) \cdot (1 - e^{-\gamma \cdot \varepsilon_p}) \quad (65)$$

$$b = \gamma \quad (66)$$

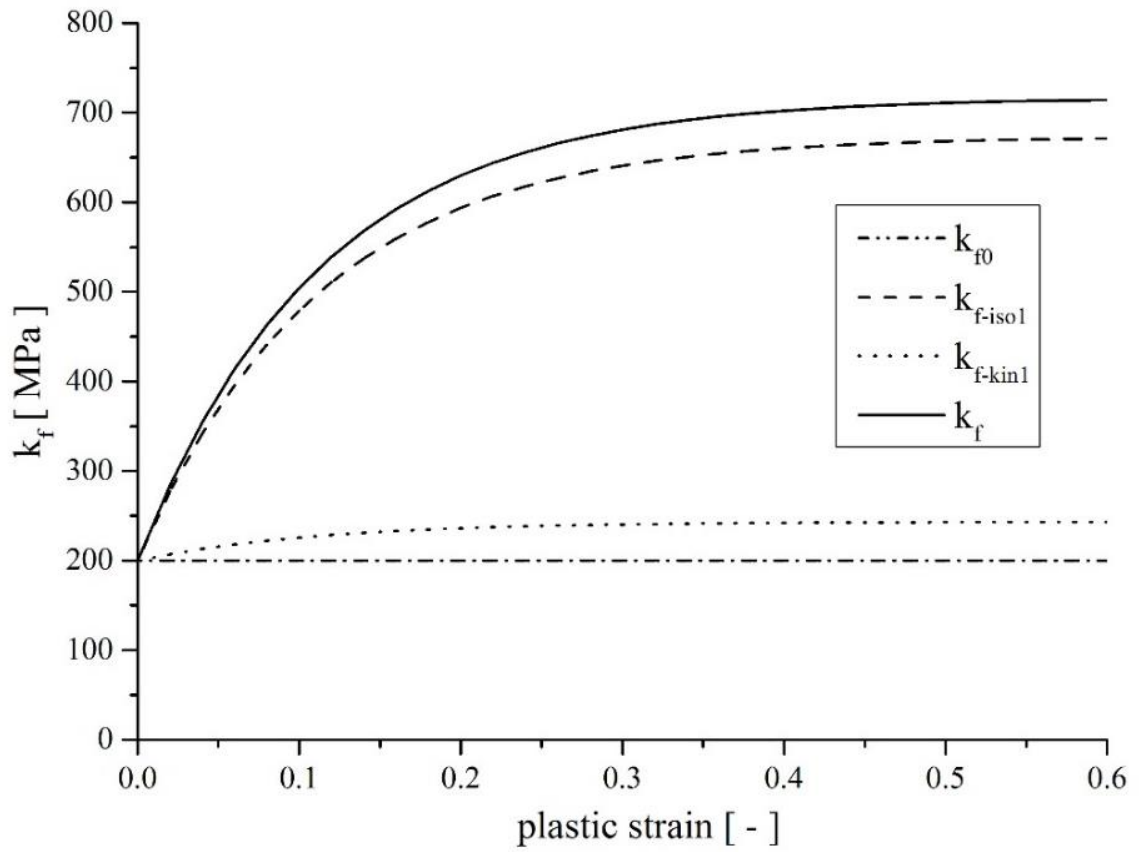


Fig. 70: Combined flow curve.

With the generated combination of the strain hardening parameters, the FEM simulation is processed again to establish the stress state of the experiment.

## 9.2 Result of the Hardening Models during Ball Spinning

All simulation results are taken from two incremental elements in the steady state region 8 mm from the front end at the outer and inner side of the tube. Fig. 71 shows the plastic strain in the radial, tangential and axial direction as well as the effective plastic strain (PEEQ) of the isotropic (a) and the kinematic (b) hardening at the inside of the tube. It can be seen, that the radial strain PE11 and the axial strain PE33 are reversing during the deformation.

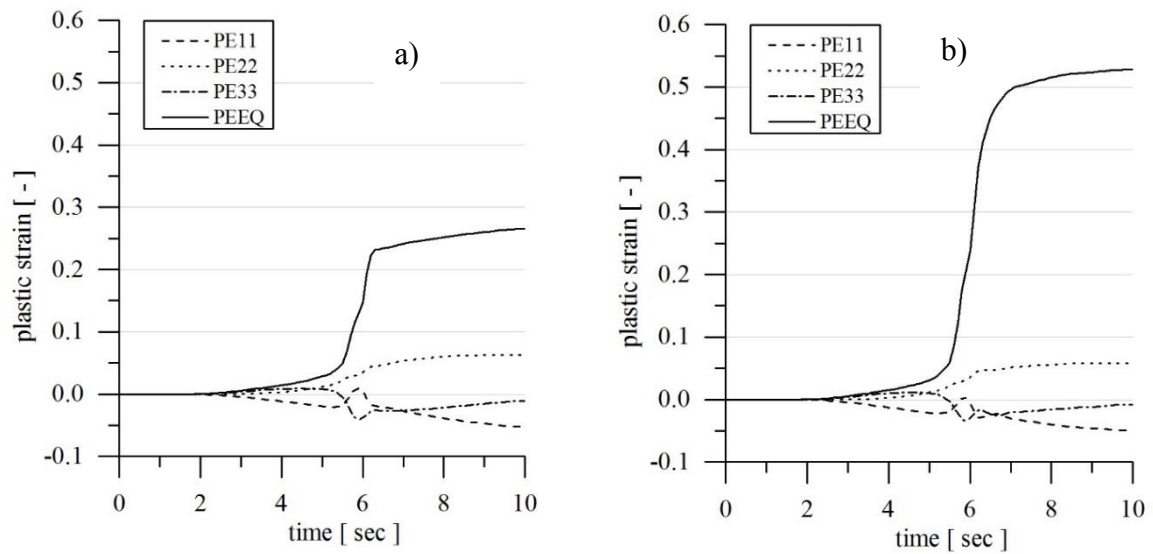


Fig. 71: Plastic strains in each direction of isotropic (a) and kinematic (b) hardening.

Fig. 72 displays the axial stresses of the isotropic and kinematic hardening model at the in- and outside of the tube. The internal stresses are about two thirds higher in the isotropic hardening model than in the kinematic hardening model

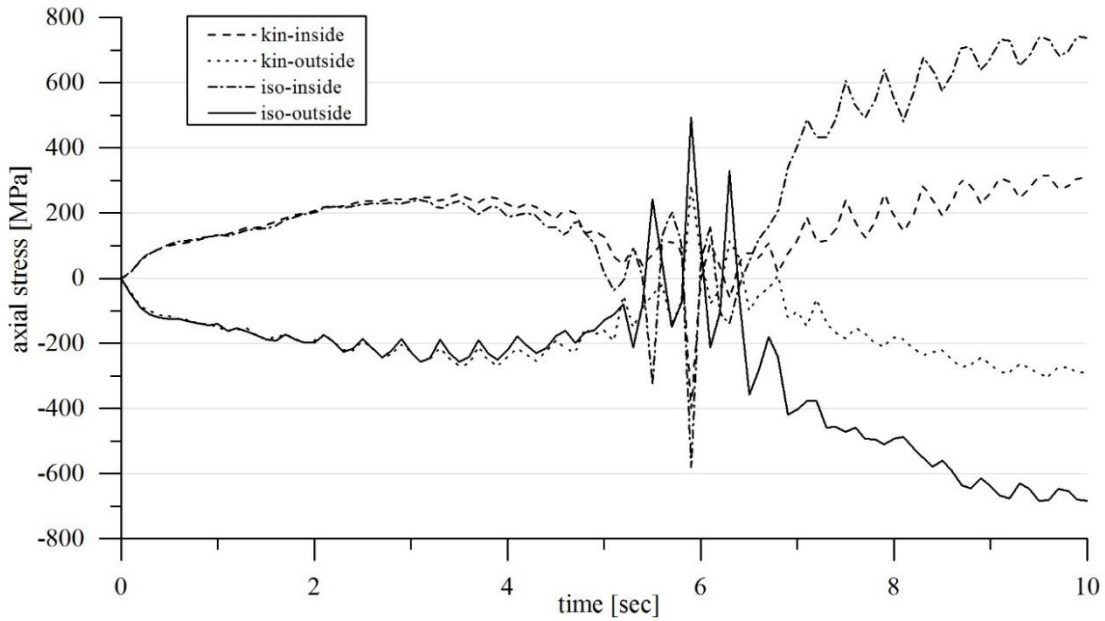


Fig. 72: Axial stresses of isotropic and kinematic hardening at the in- and outside of the tube.

The tangential stresses of the in- and outside of the tube and the different hardening models are pointed out in Fig. 73. Thereby the stresses of the kinematic model are about half of the ones of the isotropic model. However, the radial stresses show no significant differences for the two hardening models.

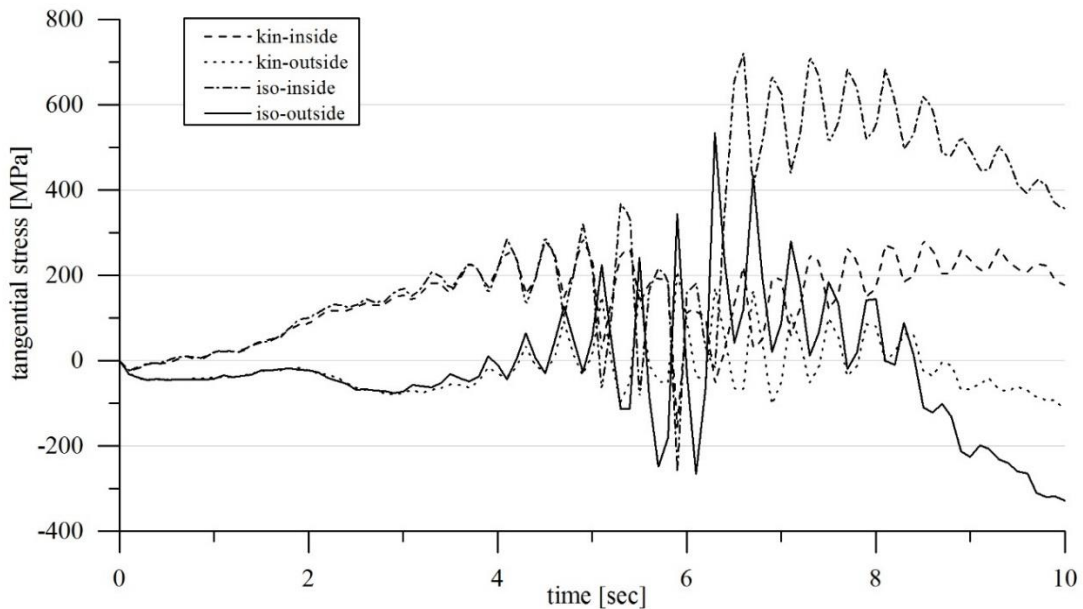


Fig. 73: Tangential stresses of isotropic and kinematic hardening at the in- and outside of the tube.

The shear strains in the tangential-axial plane of the in- and outside of the tube are shown in Fig. 74, and describes the twist of the tube after deformation. After passing the deformation zone, there is a gap between the in- and outside of the tube. The outside twists about a fourth more than the inside of the tube. The biggest distinction of the plastic strain between out- and inside is in the kinematic hardening model 0.03 and in the isotropic model with 0.025.

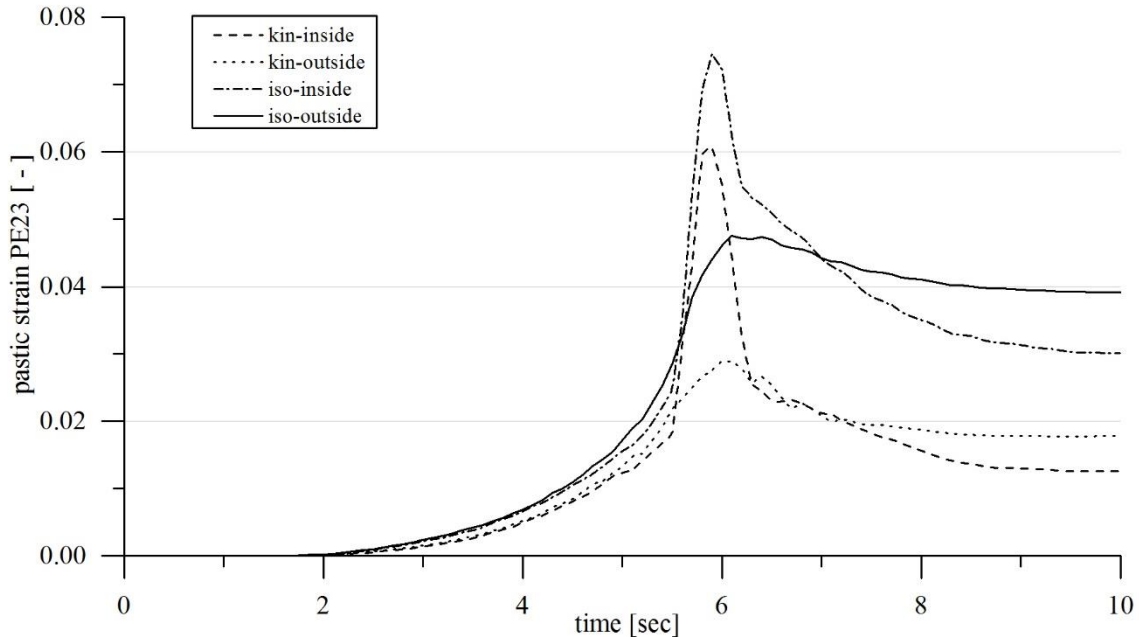


Fig. 74: Strains in the sectional plane 2-3 of the isotropic and kinematic model at the in- and outside of the tube.

Fig. 75 displays the shear strains in the radial-axial plane of the in- and outside of the tube. The positive direction of the axial coordinate is defined as leading into the tube. Therefore, in the kinematic hardening model the strains of the in- and outside are symmetric to zero after deformation. The negative shear strains are found in the outer part of the tube. Compared to the kinematic hardening model, the isotropic hardening model only has negative shear strains. The strains of the in- and outside are also reversed in the isotropic model. The inside of the tube has more strains which are negative than the outside of the tube. This effect becomes noticeable as a diameter difference of the two models after the axial cut.

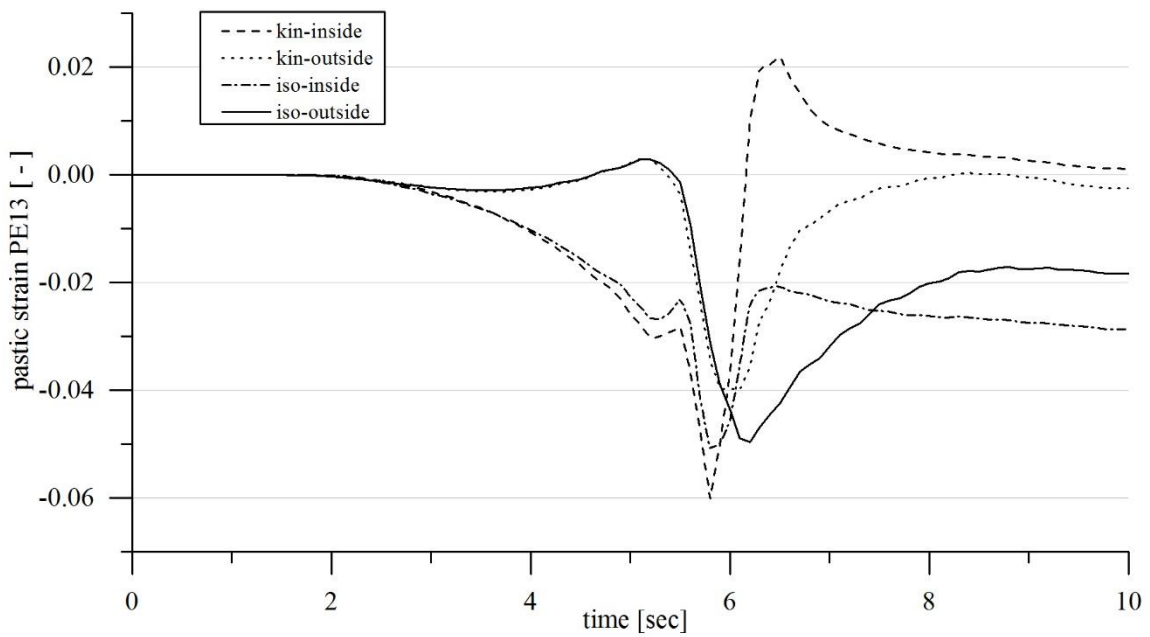


Fig. 75: Strains in the sectional plane 1-3 of the isotropic and kinematic model at the in- and outside of the tube.

Fig. 76 to Fig. 79 show the simulated stress and strain states of the kinematic, isotropic and combined hardening model. The essential differences between these two models result from the axial and tangential stresses. The physical experiment, which is represented by the combined hardening (solid line in Fig. 76) is between these two models, although closer to the isotropic model. The different stress states might also be the reason for the differences of diameter reduction after the axial cut, seen within the experiments.

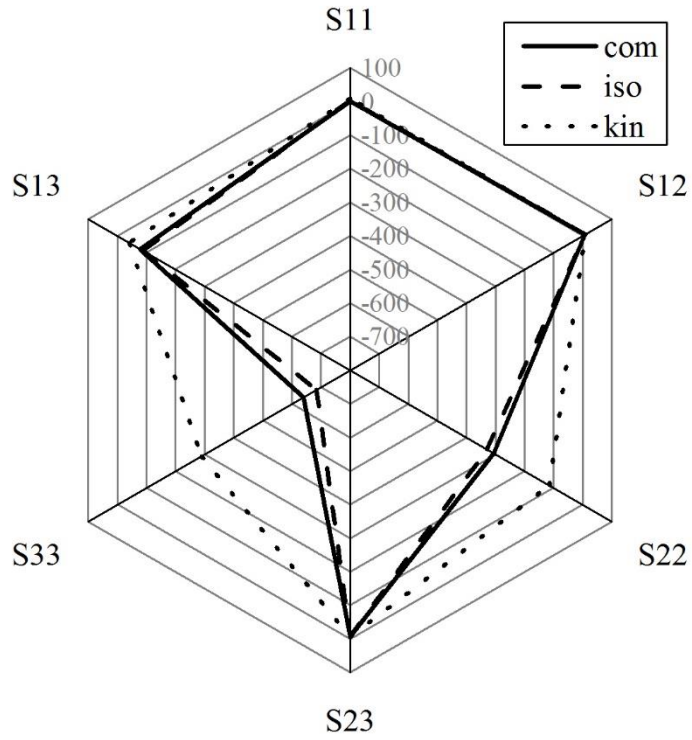


Fig. 76: Stress states of the hardening models at the outside of the tube.

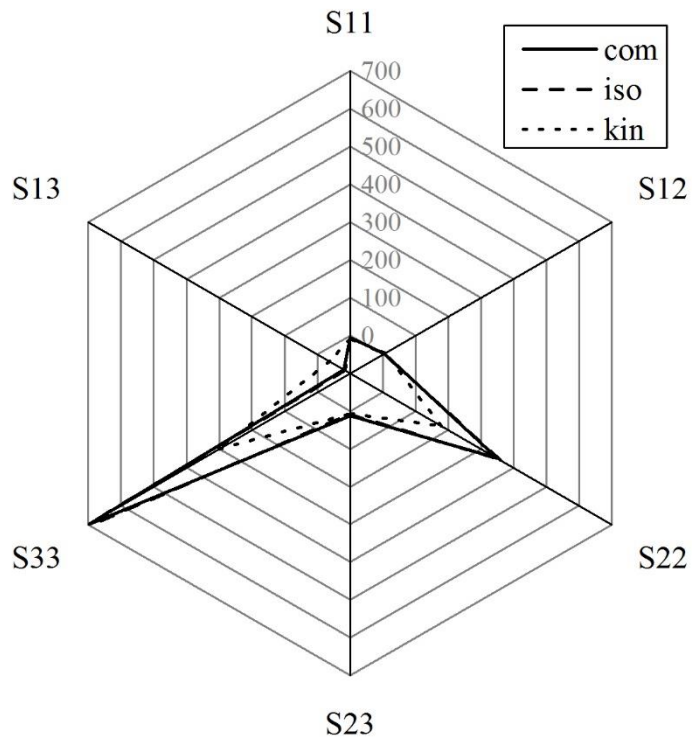


Fig. 77: Stress states of the hardening models at the inside of the tube.

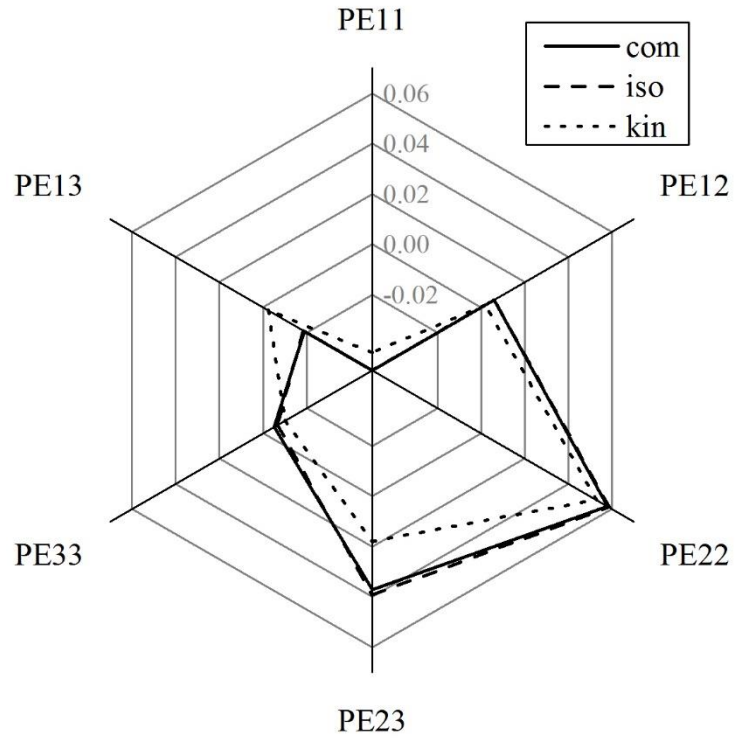


Fig. 78: Strain states of the hardening models at the outside of the tube.

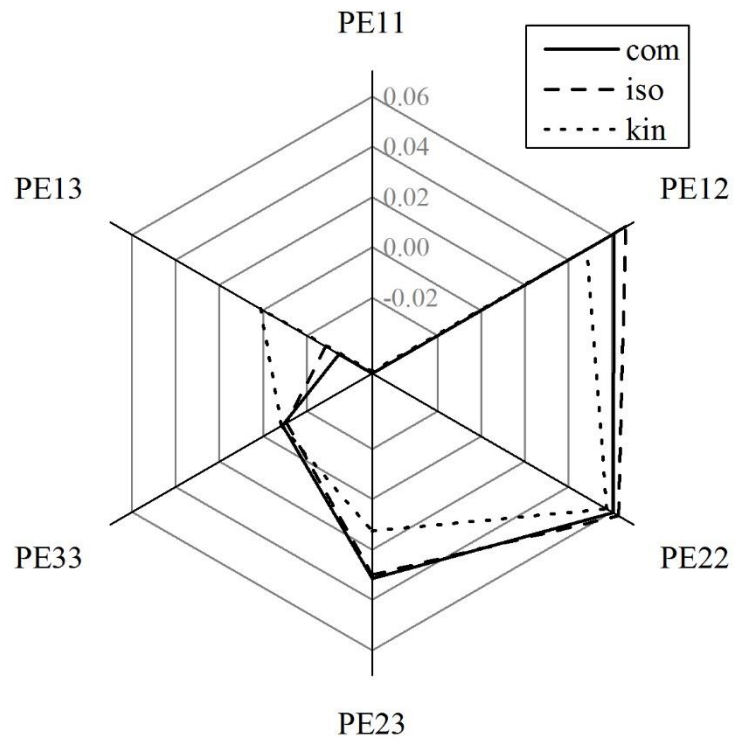


Fig. 79: Strain states of the hardening models at the inside of the tube.

The exact values of the diameter reduction of the axial cut are listed in Table 12.

Table 12: Diameter reduction of the isotropic, combined and kinematic hardening and of the experimental tube.

	ISO	KOM	REA	KIN
deformed diameter	36.919 mm	36.905 mm	36.780 mm	36.740 mm
cut diameter	36.683 mm	36.670 mm	36.548 mm	36.548 mm
diameter difference	0.236 mm	0.235 mm	0.232 mm	0.192 mm

## 10. Discussion

Ball spinning and flow forming are interesting processes with a complex deformation mechanism. Although there is no big market need for this process, there are some remarkable effects, which are prospected in this investigation.

At the beginning, the modified influence matrix displays the right way for an optimized construction of a ball spinning process (Fig. 20). The workpiece should be designed as small and as thin as possible with the lowest claimed yield stress. Big ball diameters are good for the reduction or expansion of the tube. For calibration and finishing, small diameters should be preferred. With respect to the process time, it is useful to find the right balance between the axial force and build-up in front of the forming zone. Fig. 22 shows, that incorrect process parameters have a strong negative influence on the material of the workpiece. The statements formulated from the contradiction-matrix for ball spinning could also be an initial point for new developments of the ball spinning technology.

There are some special demands for the simulation of flow forming or ball spinning processes, which are listened in the chapter “Finite Element Simulation of Flow Forming and Ball Spinning”. Nevertheless, the simulation needs to be a compromise between the effort of the knowledge profit, the resulted errors and the speed of the simulation.

The next related process of flow forming is radial forging and the differences are shown in the chapter “Radial Forging versus Flow Forming”. It is shown, that flow forming is useful for small tube thicknesses or for the deformation of the surface itself.

The chapter “Forming Forces of Ball Spinning” describes a method to calculate the forming forces analytically. The final geometry achieved in the FEM simulation is nearly identical to the experimental result (Fig. 42). Only at the front of the tube, the FEM simulation underruns the diameter compared to the experiment. A possible cause for this could be the isotropic strain-hardening model used in the simulation. With respect to the knowledge of the different stages during the expanding process (Fig. 43), it is possible to compare the steady state zones (IV) of the experiment, the simulation and the analytical calculation. Bearing in mind, that an ideal plastic hardening model is used for the analytical calculation, it can be stated that

the analytical solution and the solution of the FEM simulation describe the expanding process sufficiently. This is demonstrated in the comparison shown in Fig. 44.

One of the most interesting effects of ball spinning is the occurring surface hardening. This effect arises from the expanding process at the inner surface of the tube. This is demonstrated in Fig. 50 and in the measured difference of the grain size (Fig. 47). The highest stresses occurred at the inner surface in tangential and axial direction (Fig. 51). This is also the location, where first cracks and chipping occur. The simulation shows different forming zones for the shear stresses in Z-X direction (Fig. 52). The highest positive shear stresses are in front of the contact zone and the negative shear stresses are behind the contact zone. A different deformation mechanism appears in the X-Y section. The highest shear stresses are located between the deformation zones. Negative shear stresses are located at the outer diameter and positive shear stresses at the inner diameter.

The benefit of the chapter “Sensitivity Study on the Effects of Process Parameters on the Forming Force” is shown in Fig. 53. The analytical calculation facilitates the estimation of the effects of the parameter variations of the forming forces. The flow stress, the efficiency of plastic deformation and the radial reaming transform all forming forces except for the gap between the directions. The gap between the directions and the forces themselves is transformed by changing the ball diameter and the axial feed rate. This analytical sensitivity study could be a reference to avoid production problems. The drive torque is significantly influenced by the friction (Fig. 54) and the frictionless drive torque of the forming process is 3.85Nm (experiment ID4). The predominant part of the drive torque is the moment caused by the friction and is composed of the tube-ball contact friction (shear frictional stress) and the ball-leading ring contact friction (coulomb). However, the simulations display no significant change of the axial force by changing the friction coefficient.

The majority of manufacturing defects are cracks and chatter marks at the surface. These effects can be simulated using damage factors. In combination with a statistical design of simulation, the parameter variation of the damage behaviour is presented. One of the results of the statistical simulation design is Fig. 58, which displays the influence of both, the parameter tool diameter ratio  $D_1/d$  and the workpiece diameter ratio  $D_1/D_2$ , to the damage. With smaller tool diameter ratio  $D_1/d$ , the damage range diminishes. A higher diameter ratio  $D_1/D_2$  results in higher damage. Fig. 59 describes the influence of the workpiece diameter ratio  $D_1/D_2$  and the

feed rate  $v$  on the damage level. Thereby, the strong impact of the feed rate is mapped. If the material is steamrolled too often with small deformations, the Ayada-Damage value will increase. The influence of the tool diameter ratio  $D_1/d$  and the feed rate  $v$  on the damage is illustrated in Fig. 60. The best ball spinning performance with a constant diameter reduction will be achieved by using a large ball diameter and a high feed rate. Due to the 2D simulation with generalized plane strain elements, the axial bulge in Fig. 65 is not considered in this simulation method.

The deformation mechanism during ball spinning with the build-up during diameter reduction and reaming during diameter expansion leads to strain hardening behaviour. The proof of the reversed hardening is shown with a FEM simulation in Fig. 71. Therefore, the axial and tangential strain components change their directions at the time of the first contact with the ball. This effect is shown in the PEEQ curve. Due to the reversing strain hardening of the kinematic model, the effective plastic strain is about twice as high as for the isotropic model.

This study reveals new insight to the theme of ball spinning and might guide the way to understand the internal stresses after the deformation. The isotropic hardening model describes a higher strain hardening than the kinematic one. Hence, the current flow stress of the material is higher and the internal stresses are about two thirds higher than the kinematic hardening model as displayed in Fig. 72. Due to the thin tube, this effect occurs at the inner and outer side of the tube in the same way. The systematic of the strain hardening of these two models are also applicable for the tangential stresses (Fig. 73). Thereby, the stresses of the kinematic model are about the half as the ones of the isotropic model.

The shear strain in the tangential-axial plane displayed in Fig. 74 describes the twist of the tube after deformation. Therefore, the twist of the isotropic hardening model is about three times higher than in the kinematic model. After passing the deformation zone, there is a gap between the in- and outside of the tube. The outside twist is about 25 % higher than the inside of the tube. The biggest distinction of the plastic strain between out- and inside is in the kinematic hardening model 0.03 and in the isotropic model with 0.025.

Fig. 75 displays the shear strain in the sectional plane 1-3. The positive direction of the axial coordinate is defined as leading into the tube. Therefore, in the kinematic hardening model the strains of the in- and outside are symmetric to zero after deformation. The negative shear

strains are found in the outer part of the tube. Compared to the kinematic hardening model, the isotropic hardening model only obtains negative shear strains. The strains of the in- and outside are reversed in the isotropic model. The inside of the tube has more negative strains, than the outside of the tube. This effect results in different diameters of the two models after the axial cut.

One interesting point is the comparison between the stress states of the isotropic, kinematic and combined hardening model (Fig. 76 to Fig. 77). The essential differences between these two models result from the axial and tangential stresses. This is also the reason for the diverging diameter reduction after the axial cut. The differences in the strain state of the models (Fig. 78 to Fig. 79) are the shear strains, section 1-2, 2-3 and 3-1. The stress- and strain state of the combined hardening model represents the experiment.

Overall the linear combination of the two models does not entirely match with the listings in Table 12. The diameter reduction after the axial cut is not equivalent to the isotropic coefficient  $h_{iso}$ . This is attributed to the measurement inaccuracy and the linear parameter combination.

## 11. Conclusion and Outlook

Engineers are forced to come up with better predictions of forming processes. Deformation forces, damage and lifetime predictions, and the internal stress states are points of interest at an early stage of construction. Therefore, methods and calculations are required to accelerate the development period. Three new approaches for the investigation of the ball spinning technology are presented in this thesis:

- analytical prediction of the forming forces
- method to prospect the damage behavior with FEM
- method to combine and calibrate hardening models with FEM

The novelty of the analytical model to predict the forming force is its adaptability for the tube expansion process of ball spinning. The model has been validated experimentally and by finite element simulation. The numerical simulation and the analytical model agree quite well with the experimental results. It is possible to conclude that the model sufficiently predicts the deformation forces during the expansion process of ball spinning. In addition, the use of this model illustrates the influence on selected process parameters on the deformation forces. Overall, the model allows to predict the necessary forces for the process at the beginning of product development.

This investigation proposes a simple 2D FEM model to analyse damage effects during ball spinning. The FEM simulation in combination with a central statistical experiment design provides a useful tool to invest in deformation behaviour with a low number of simulations. The result is a regression polynomial with three variables. Thereby, the linear, quadratic, and interacting influence on each parameter is calculated. It has been shown, that the workpiece diameter ratio  $D_1/D_2$  and the feed rate  $v$  have an essential influence on the damage behaviour of ball spinning. A useful result of this investigation is that according to Ayada-Damage, increasing the feed rate can reduce the damage. The result of this model allows one to predict the necessary process parameters for a damage minimised ball spinning process.

The internal stress states influences the lifetime drastically. Hence, the forming simulation has to include more deformation mechanism like kinematic hardening. This investigation shows, that the two hardening models result in different internal stress states. Moreover, the final geometry after deformation is different. For the ball spinning expansion process the internal stresses with kinematic hardening models are about a third lower in axial direction and about a half lower in tangential direction. In addition, the twist after deformation is about a third lower than in the isotropic hardening model. To represent the real stress- and strain state, a combination of these two models is necessary. This investigation presents a method to combine and to calibrate the strain hardening parameter. The linear combination of the strain hardening parameters due to an initial stress relaxation is a practicable method to estimate the strain hardening method and therefore the internal stress state.

Maybe ball spinning displays a new upswing for products with longitudinal internal ribs, cheap manufacturing costs and low to middle lot sizes. It is important to combine the knowledge of workers at the machines with scientific investigations of metal forming and materials science. The next milestone of metal forming will be the measurement of the kinematic and isotropic hardening behaviour for high strains. Furthermore, FEM-Software has to include the influences on temperature, velocity and sequences to the different models.

## **Bibliography**

Ahmed, K.I.E., A new ball set for tube spinning of thin-walled tubular parts with longitudinal inner ribs, *Journal of Engineering Sciences, Assiut University*, Volume 39, No 1, 2011, pp.15-32.

Altschuller, G.S., *Erfinden – Wege zur Lösung technischer Probleme*, Publisher - Thiel, R., Patzwaldt, H., Publishing House - Technik, Berlin, 1984.

Ayada, M., Higashino, T., Mori, K., Central Bursting in Extrusion of Inhomogeneous Materials, *Advanced Technology of Plasticity 1*, 1987, pp. 553-558.

Birk, K., *Untersuchungen zur Anwendung des Abstreckdrückens bei der Fertigung rotationssymmetrischer Hohlkörper mit Innenverzahnung*, PhD-Thesis, TU Karl-Marx-Stadt, 1985.

Chaboche, J.L., Constitutive equations for cyclic plasticity and cyclic viscoplasticity, *International Journal of Plasticity*, Volume 5. 1989, pp.247-302.

Chaboche, J.L., A review of some plasticity and viscoplasticity constitutive theories, *International Journal of Plasticity*, Volume 24, 2008, pp. 1642-1693.

Eversheim, W., *Innovationsmanagement für technische Produkte*, Springer-Verlag Berlin Heidelberg, 2003.

Doegel, E., Behrens, B.-A., *Handbuch Umformtechnik, Grundlagen, Technologien, Maschinen*, 2. Edition, Springer-Verlag Berlin Heidelberg, 2010.

Friedmann, O., *Untersuchungen zum Abstreckdrücken kreiszylindrischer Hohlkörper*, PhD-Thesis, TU Karl-Marx-Stadt, 1984.

Groche, P., Fritsche, D., Application and modelling of flow forming manufacturing processes for internally geared wheels, *Int. Journal of Machine Tools and Manufacture*, Volume 46, 2006, p.1261–1265.

Heidel, K.-H., Kühmel, S., Verfahrensoptimierung des Abstreckdrückens mit Kugeln für tiefgezogene Näpfe, PhD-Thesis, TU Karl-Marx-Stadt, 1979.

Herold, G., Abdel-Kader, S., Einfluss der Prozessparameter beim Drückwalzen auf den Werkstofffluss und die Produktqualität, *Sächsische Fachtagung Umformtechnik*, 26th-27th November, 1998.

Hertz, H., Über die Berührung fester elastischer Körper, *Journal für die reine und angewante Mathematik*, Volume 92, 1881, p.156-171.

Hofen, W., Wenke, R., Untersuchung zur Weiterentwicklung des Fließdrückens, PhD-Thesis, Ingenieurhochschule Zwickau, 1986.

Hong, S.I., Rhee, S.H., Yun, S.J., A Study on the Neck-in Process by Flow-Forming, *Metals and Materials*, Vol.4, No.4, 1998, p.895-898.

Houillon, M., Massoni, E., Ramel, E., Logé R., 3D FEM Simulation of the Flow Forming Process Using Lagrangian and ALE Methods, *Numiform, Materials Processing and Design: Modeling, Simulation and Applications*, 2007.

Hua, F.A., Yang, Y.S., Zhang, M.H., Guo, M.H., Guo, D.Y., Tong, W.H., Hu, Z.Q., Three-dimensional finite element analysis of tube spinning, *Journal of Materials Processing Technology*, Volume 168, 2005, p.68–74.

Jiang, S., Ren, Z., Li, C., Role of ball size in backward ball spinning of thin-walled tubular part with longitudinal inner ribs, *Journal of Materials Processing Technology*, Volume 209, Issue 4, 2009, p.2167–2174.

Kleppmann, W., Taschenbuch Versuchsplanung, Hanser Verlag, München Wien, 5. Edition, 2008.

Klocke, F., König, W., Fertigungsverfahren Umformen, Springer-Verlag Berlin Heidelberg, 5. Edition, 2006.

Kuss, M., Buchmayr, B., Systematische Prozessbetrachtung von Flow Forming, Colloquium on Metal Forming, Planneralm, 2013.

Kuss, M., Buchmayr, B., Radialschmieden versus Zylinderdruckwalzen, Berg- und Hüttenmännische Monatshefte, Volume 159, No 5, 2014, p.208-213.

Kuss, M., Buchmayr, B., Analytical, numerical and experimental investigations of ball spinning expansion process, Journal of Materials Processing Technology, Volume 224, 2015, p.213-221.

Kuss, M., Buchmayr, B., Damage minimised ball spinning process design, Journal of Materials Processing Technology, Volume 234, 2016, p.10-17.

Li, M., Kang, D., Zhang, S., Xu, Y., Wang, Z., A Theoretical Analysis of Ball Spinning, Journal of Materials Science and Technology, Volume 18, No.3, 2002, p.275-278.

Lemaitre, J., Chaboche, J.L., Mechanics of solid materials, University of Cambridge, 2002.

Lindemann, U., Methodische Entwicklung technischer Produkte, Springer-Verlag Berlin Heidelberg, 2006.

von Mises, R., Mechanik der festen Körper im plastisch deformablen Zustand. Nachrichten der Gesellschaft der Wissenschaften in Göttingen, 1931, Mathematisch Physikalische Klasse, pp. 582-592.

Rotarescu, M., A theoretical analysis of tube spinning using balls, Journal of Materials Processing Technology 54, 1995, p.224–229.

Runge, M., Drücken und Drückwalzen: Umformtechnik, Werkstückgestaltung, Maschinen, Steuerungskonzepte, Verl. Moderne Industrie, Die Bibliothek der Technik, Issue 72, 1993.

Scheffler, E., Statistische Versuchsplanung und –auswertung, Deutscher Verlag für Grundstoffindustrie, Stuttgart, 3. Edition, 1997.

Siebel, E., Die Formgebung im bildsamen Zustande, Publisher House - Stahleisen m.b.H. Düsseldorf, 1932.

Sivanandini, M., Dhami, S.S., Pabla, B:S: Flow Forming of tubes a review, International Journal of Scientific & Engineering Research, Volume 3, Issue 5, May 2012.

Thamasett, E., Kräfte und Grenzformänderungen beim Abstreckdrücken zylindrischer, rotationssymmetrischer Hohlkörper aus Aluminium, PhD-Thesis, University of Stuttgart, 1961.

Ufer, R., Modellierung und Simulation von Drückwalzprozessen, PhD-Thesis, Technical University of Chemnitz, 2006.

Ufer, R., Awiszus, B., Neue Möglichkeiten der Simulation des Drückwalzens, wt Werkstattstechnik online 95 (10), 2005, p.759-764.

Wang, S., Zhao, B., FEM Analysis of the Different Spinning Speed of Inner Groove Copper Tube Formed, 2nd International Conference on Modelling, Identification and Control, Paris, 2015.

Wenke, R., Entwicklung einer Abstreckdrückvorrichtung für das Abstreckdrücken mit umlaufenden Stahlkugeln, Ing.-praktikumsarbeit (FMF 73 – 104.1), TH Karl-Marx-Stadt, Sektion FPM, 1973.

Wong, C.C., Dean, T.A., Lin, J., A review of spinning, shear forming and flow forming processes, International Journal of Machine Tools & Manufacture 43, 2003, p.1419-1435.



## List of Figures

Fig. 1: Set up for a metal spinning process (Runge, 1993). .....	7
Fig. 2: Classification of metal spinning processes. ....	8
Fig. 3: Spinning and shear spinning products (Runge, 1993). ....	9
Fig. 4: Principle of flow forming 1) forward flow forming, 2) backward flow forming. ....	9
Fig. 5: Flow forming process (left) and products of such a process (right) (Runge, 1993). ....	10
Fig. 6: Combination of expansion process and flow forming .....	10
Fig. 7: Combination of extrusion and flow forming (Herold and Abdel-Kader, 1998). ....	11
Fig. 8: Principle of friction spinning by Homberger (2009). ....	11
Fig. 9: Process description: (a) three roll principle, (b) multiple roll principle. ....	12
Fig. 10: Set up of a ball spinning reduction process (Kuss & Buchmayr, 2015). ....	13
Fig. 11: Ball spinning with variable diameter (Jiang et. al. 2009). ....	14
Fig. 12: Step tool for reduction of a round blank with ball spinning .....	15
Fig. 13: Set up of a ball spinning expansion process (Kuss & Buchmayr, 2015). ....	15
Fig. 14: Leading ring geometries. ....	17
Fig. 15: Lifecycle curve (Eversheim 2003). ....	19
Fig. 16: Count of publications of Flow Forming and Ball Spinning .....	19
Fig. 17: Influence matrix of ball spinning. ....	21
Fig. 18: Active and passive sum of the influence matrix for a ball spinning process. ....	23
Fig. 19: Active/passive sum and influence range of one parameter. ....	24
Fig. 20: Parameter influence on ball spinning. ....	25
Fig. 21: Vector diagram of the positive influence on ball spinning. ....	26
Fig. 22: Vector diagram of the negative influence on ball spinning. ....	27
Fig. 23: 2D FEM simulation of flow forming. ....	29
Fig. 24: 3D Simulation of ball spinning with symmetry areas (Wang and Zhao 2015). ....	30
Fig. 25: Kinematic structure of a ball spinning expansion process. ....	31
Fig. 26: Standard mesh and optimized mesh for a ball spinning or flow forming process. ....	31
Fig. 27: Contact area for hard (left) and softened (right) contact. ....	32
Fig. 28: Increments at the contact area and between the tools. ....	32
Fig. 29: Compromise of effort, quality and speed. ....	33
Fig. 30: Model set up of a radial forging process. ....	34
Fig. 31: Model set up of a flow forming process. ....	35
Fig. 32: Comparison of the equivalent stress between radial forging and flow forming .....	36

Fig. 33: Influence on the deformation gradient of the tube thickness during radial forging. ....	37
Fig. 34: Influence on the deformation gradient of the tube thickness during flow forming. ....	37
Fig. 35: Visualization of the parameters for the analytical calculation. ....	39
Fig. 36: Visualization of the contact surface and the gravity centre S. ....	41
Fig. 37: Visualization of the forces on the ball and the leading ring. ....	43
Fig. 38: Tubular workpiece and tool geometry. ....	45
Fig. 39: Experimental setup of the friction welding machine. ....	45
Fig. 40: Set up of the ball spinning FEM model. ....	47
Fig. 41: Formed workpiece and metallographic section. ....	48
Fig. 42: Comparison of the experimental result ID 4 with the FEM simulation. ....	48
Fig. 43: Stages of the axial forming force $F_z$ (experiment ID4). ....	49
Fig. 44: Axial force comparison of analytical calculation, experiment and simulation. ....	49
Fig. 45: Microsection of the basic structure and the welding seam. ....	50
Fig. 46: Micrograph of the basic structure and the welding seam before deformation. ....	51
Fig. 47: Microsection of the basic structure and the welding seam after deformation. ....	52
Fig. 48: Hardness profile of the basic structure. ....	52
Fig. 49: Hardness profile after deformation. ....	53
Fig. 50: Effective plastic strain of the FEM simulation in an axial section. ....	53
Fig. 51: Axial tube section showing the radial, tangential and axial stresses. ....	54
Fig. 52: Axial- and tangential tube section showing the shear stresses. ....	54
Fig. 53: Sensitivity study on the effects of process parameters on the forming forces. ....	55
Fig. 54: Sensitivity of the frictional coefficient on the drive torque. ....	56
Fig. 55: Set up of the ball spinning damage FEM model to predict damage. ....	58
Fig. 56: Schematic illustration of the contacts during ball spinning. ....	59
Fig. 57: Schematic illustration of the central composite experimental design. ....	61
Fig. 58: Regression of the damage in dependence on the tool diameter ratio $D_1/d$ . ....	67
Fig. 59: Regression of the damage in dependence on $D_1/D_2$ and the $v$ . ....	68
Fig. 60: Regression of the damage in dependence on $v$ and $D_1/d$ . ....	69
Fig. 61: Damage value of Ayada of two different experiments. ....	70
Fig. 62: Damage value according to Ayada plotted over the distance to the surface. ....	71
Fig. 63: Workpiece and tool geometry for a ball spinning reduction process. ....	71
Fig. 64: Experimental reduction setup of the friction welding machine. ....	72
Fig. 65: Sample $D_1 = 17.0$ mm & $D_1 = 16.9$ mm after ball spinning. ....	72
Fig. 66: Schematics of the isotropic hardening. ....	76

Fig. 67: Tabular flow curve of 1.4301 as used for the FEM simulation. .... 76

Fig. 68: Schematics of the linear kinematic hardening. .... 77

Fig. 69: Tangential stress of isotropic hardening of the tube and the physical workpiece..... 78

Fig. 70: Combined flow curve..... 81

Fig. 71: Plastic strains in each direction of isotropic (a) and kinematic (b) hardening ..... 82

Fig. 72: Axial stresses of isotropic and kinematic hardening of the tube..... 83

Fig. 73: Tangential stresses of isotropic and kinematic hardening of the tube. .... 83

Fig. 74: Strains in the sectional plane 2-3 of the isotropic and kinematic model..... 84

Fig. 75: Strains in the sectional plane 1-3 of the isotropic and kinematic model..... 85

Fig. 76: Stress states of the hardening models at the outside of the tube. .... 86

Fig. 77: Stress states of the hardening models at the inside of the tube. .... 86

Fig. 78: Strain states of the hardening models at the outside of the tube. .... 87

Fig. 79: Strain states of the hardening models at the inside of the tube. .... 87

**List of Tables**

Table 1: Process parameter for radial forging and flow forming. ....	35
Table 2: Nomenclature and parameters for the analytical calculation of the ball spinning. ....	39
Table 3: Design of experiments for measure the forming force. ....	46
Table 4: Fictitious values of the flow curve. ....	59
Table 5: Parameter combination for the central composite experimental design. ....	64
Table 6: Parameter of real experiments. ....	64
Table 7: Results of the central composite experimental design. ....	65
Table 8: Coefficients for the normalized values of the regression polynomial. ....	66
Table 9: Roughness value of the two experiments after ball spinning. ....	73
Table 10: Different plasticity criteria and flow rules (Lemaitre and Chaboche 2002). ....	74
Table 11: Diameter springsback after the axial cut. ....	79
Table 12: Diameter reduction of the isotropic, combined and kinematic hardening. ....	88

---

## Author's Publications

### 2011:

Kuss, M., FEM-Analyse des Axial-Radial-Umformens als Verfahrenserweiterung des Radialschmiedens, Diploma Thesis, Chair of Metal Forming, Montanuniversitaet Leoben, 2011.

### 2012:

Hofer, F., Kuss, M., Wallner, S., Buchmayr, B., Harrer, O.K., Lightweight design by radial forged gear box components, International VDI-Congress Drivetrain for Vehicles, Friedrichshafen / Germany 2012, pp.309-319.

Kuss, M., Wallner, S., Harrer, O.K., Buchmayr, B., Analyse des Axial-Radial-Umformens mittels Finite-Elemente-Methode, BHM Berg- und Hüttenmännische Monatshefte 2012, pp.181-186.

Kuss, M., Wallner, S., Buchmayr, B., FEM-Analyse des Axial-Radial-Umformens als Verfahrenserweiterung des Radialschmiedens, 13. Round Table Simulation Manufacturing, Bamberg / Germany 2012, pp.228-245.

Kuss, M., Wallner, S., Buchmayr, B., FEM-Analyse des Axial-Radial-Umformens als Verfahrenserweiterung des Radialschmiedens, 31. Colloquium on Metal Forming, Planneralm / Austria 2012, pp.29-33.

Hatzenbichler, T., Harrer, O.K., Wallner, S., Planitzer, F., Kuss, M., Pschera, R., Buchmayr, B., Deviation of the results obtained from different commercial finite element solvers due to friction, Tribology International 49, 2012, pp.75–79.

## 2013:

Kuss, M., Buchmayr, B., Systematische Prozessbetrachtung von Flow Forming, 31. Colloquium on Metal Forming, Plannersalm / Austria 2013, pp.131-136.

Kuss, M., Harrer, O.K., Buchmayr, B., Herausforderungen bei der Simulation von inkrementellen Umformverfahren zur Herstellung von Leichtbauprodukten, New Developments in Forging Technology, Stuttgart, Germany, 2013.

## 2014:

Kuss, M., Buchmayr, B., Radialschmieden versus Zylinderdrückwalzen, Berg- und hüttenmännische Monatshefte, Volume 159, Issue 5, 2014.

Fritz, R., Kuss, M., Buchmayr, B., Charakterisierung des Beulverhaltens von Gaspipelines ASMET Forum, Montanuniversitaet Leoben, 2014.

## 2015:

Kuss, M., Buchmayr, B., Analytical, numerical and experimental investigations of ball spinning expansion process, Journal of Materials Processing Technology, Volume 224, 2015, p.213-221.

Kuss, M., Buchmayr, B., Simulation inkrementeller Rohraufweitung, 16. Round Table Simulation Manufacturing, Bamberg / Germany 2015.

Buchmayr, B., Kuss, M., Flowforming research at Montanuniversitaet Leoben", Steel Tailored Tubes, 2015.

## 2016:

Kuss, M., Buchmayr, B., Damage minimised ball spinning process design, Journal of Materials Processing Technology, Volume 234, 2016, p.10-17.